Determination of an arrival time cut for the separation of electrons and muons in extensive air showers

Dissertation

zur Erlangung des akademischen Grades eines

Doktors der Naturwissenschaften

vorgelegt von

Diplom-Physiker Marc Brüggemann

geboren am 25. Juni 1977 in Hamm (Westfalen)

genehmigt vom Fachbereich Physik
der Universität Siegen

Siegen
Dezember 2006

Abstract

Extensive air showers measured by the KASCADE-Grande experiment at the Forschungszentrum Karlsruhe are studied with respect to the arrival times of electrons and muons at observation level. KASCADE-Grande is a ground based detector array to study extensive air showers generated by primary cosmic ray particles in the energy range from 10^{14} eV to 10^{18} eV. Approximately 290,000 air showers measured between January 2005 and Febuary 2006 are used to generate arrival time distributions of electrons and muons for 13 intervals of the distance R to the shower center. The particle arrival times are reconstructed by unfolding detector signal pulses sampled by a Flash-ADC based data acquisition system connected to the e/γ- and μ-detectors of eight detector stations of the KASCADE detector array. For distances $R > 200$ m particles of the muonic shower component arrive on average earlier at observation level than particles of the electromagnetic shower component. This difference in arrival time is used to determine a cut on the particle arrival time as a function of the distance from the shower center. This cut is intended to be used by experiments with time resolving detectors for the separation of electrons and muons according to their arrival times relative to the arrival time of the shower core. Particles with arrival times smaller than the cut are considered as muons. Due to the large spread of the arrival time distributions the number of muons reconstructed in this way will contain a contribution from the electromagnetic shower component. For each separation cut value the purity of the reconstructed muon sample is determined.

Zusammenfassung

In der vorliegenden Arbeit werden Elektronen und Myonen in ausgedehnten Luftschauern, die mit dem KASCADE-Grande-Experiment am Forschungszentrum Karlsruhe gemessen wurden, hinsichtlich ihrer Ankunftszeiten am Boden studiert. KASCADE-Grande ist ein Experiment zur Messung ausgedehnter Luftschauer, die von Teilchen der primären kosmischen Strahlung im Energiebereich von 10^{14} eV bis 10^{18} eV in der Erdatmosphäre erzeugt werden. Etwa 290.000 Luftschauer, die zwischen Januar 2005 und Februar 2006 gemessen wurden, werden verwendet, um für 13 Intervalle des Abstandes R zum Schauerzentrum Verteilungen der Teilchenankunftszeiten zu erzeugen. Die Teilchenankunftszeiten werden unter Verwendung eines Entfaltungsalgorithmus aus Detektorsignalen extrahiert, die mittels eines Flash-ADC basierten Datennahmesystems digitalisiert wurden, welches an die e/γ- und μ-Detektoren von acht Stationen des KASCADE-Detektorfeldes angeschlossen ist. Für Abstände $R > 200$ m erreichen die Myonen den Boden im Mittel früher als die Elektronen. Diese Differenz in der Teilchenankunftszeit wird verwendet, um einen Schnitt auf die Teilchenankunftszeit als Funktion des Abstandes zum Schauerzentrum zu bestimmen. Dieser Schnitt ist für Experimente mit zeitauflösenden Detektoren gedacht, um Elektronen und Myonen anhand ihrer Ankunftszeiten relativ zur Ankunftszeit des Schauerkerns zu trennen. Teilchen mit Ankunftszeiten kleiner als der Schnitt werden als Myonen betrachtet. Wegen der großen Streuung der Verteilungen der Teilchenankunftszeiten wird die Zahl der Myonen, die auf diese Weise bestimmt wird, einen Beitrag der elektromagnetischen Schauerkomponente enthalten. Für jeden Wert des Schnitts auf die Teilchenankunftszeit wird die Reinheit der rekonstruierten Myonauswahl bestimmt.

Contents

Introduction

High energy cosmic particles can be studied by analyzing the extensive air showers of secondary particles they generate in the atmosphere. These extensive air showers are measured by sampling the shower front of secondary particles with detector arrays at ground level. The sources of the initial highly energetic primary particles are still unknown. Their energy spectrum, averaged over all particle types, can be described by a power law over many orders of magnitude of primary energy. At an energy of about 3 PeV a structure in the all particle energy spectrum can be observed, which plays a key role for the understanding of the origins of cosmic ray particles. The sudden decrease in the flux of primary particles with higher energies is commonly referred to as the knee in the cosmic ray energy spectrum. Theoretical models of the origin of the knee predict a dependence of the knee position either on the charge Z or the mass A of the cosmic ray particles. In order to confirm or exclude different models, energy spectra of the individual elements in the cosmic radiation have to be studied. In order to reconstruct the energy and the identity of the primary particle it became common practice to unfold the correlated frequency distribution of the electron and muon numbers in air showers.

In general, the measurement of muons requires the operation of dedicated muon detectors. This increases the number of detectors of an air shower array. Furthermore, the muon detectors have to be shielded against the electromagnetic shower component in order to measure the number of muons with high purity. Therefore, the use of dedicated muon detectors is cost intensive for large detector arrays.

Modern air shower detector arrays are equipped with fast time resolving electronics to sample the time development of the detector responses. The different development of the electromagnetic and the muonic component of extensive air showers causes a difference in the arrival times of electrons and muons at the observation level. Therefore, an alternative to dedicated muon detectors is to use the arrival time difference of electrons and muons in the shower front and to separate the particle types by an adequate

cut on the particle arrival time. In this thesis, the arrival time difference of electrons and muons of extensive air showers measured by the KASCADE-Grande experiment is studied in order to determine an appropriate time cut. This is achieved by analyzing particle arrival time distributions reconstructed from unfolded detector signals sampled by a Flash-ADC based data acquisition system installed in eight detector stations of the KASCADE detector array. The time cut is intended to be used in experiments without dedicated muon detectors but with time resolving data acquisition electronics. The muon number is then estimated by counting the particles at a distance R from the shower core with an arrival time smaller than the corresponding time cut. The contribution from the electromagnetic shower component has to be subtracted by applying an appropriate correction factor.

Chapter **2**

Cosmic rays and extensive air showers

The term "cosmic rays" refers to highly energetic charged particles constantly impinging onto the earth's atmosphere from outer space. These particles are also commonly referred to as primary particles or simply primaries. Cosmic radiation was discovered in 1912 by measuring their discharging effect in electroscopes during balloon flights [Hes12]. They are composed of distinct types of charged particles like protons, fully ionized atomic nuclei and electrons. Their energies cover 11 orders of magnitude from 10^9 eV up to 10^{20} eV.

Although cosmic rays were discovered almost a century ago, they are still subject to intensive studies today. Essential questions could not be answered so far, like the type and location of their sources, the underlying acceleration mechanisms or their exact chemical composition at energies above 100 TeV. Satellites and balloons carrying particle detectors are used to study cosmic radiation of an energy below 100 TeV. At higher energies ground based arrays of particle detectors like KASCADE-Grande are used to study the primary cosmic radiation indirectly by investigating the properties of extensive air showers, which are initiated by the interaction of the primary with air nuclei.

In the following, a brief summary of observed characteristics of cosmic rays and a brief overview of theoretical models with respect to the origin of the cosmic radiation are given.

2.1 Energy spectrum

The energy spectrum of cosmic radiation with extrasolar origin extends over more than 10 orders of magnitude, reaching from a few GeV to over 10^{20} eV. It is depicted in figure 2.1.
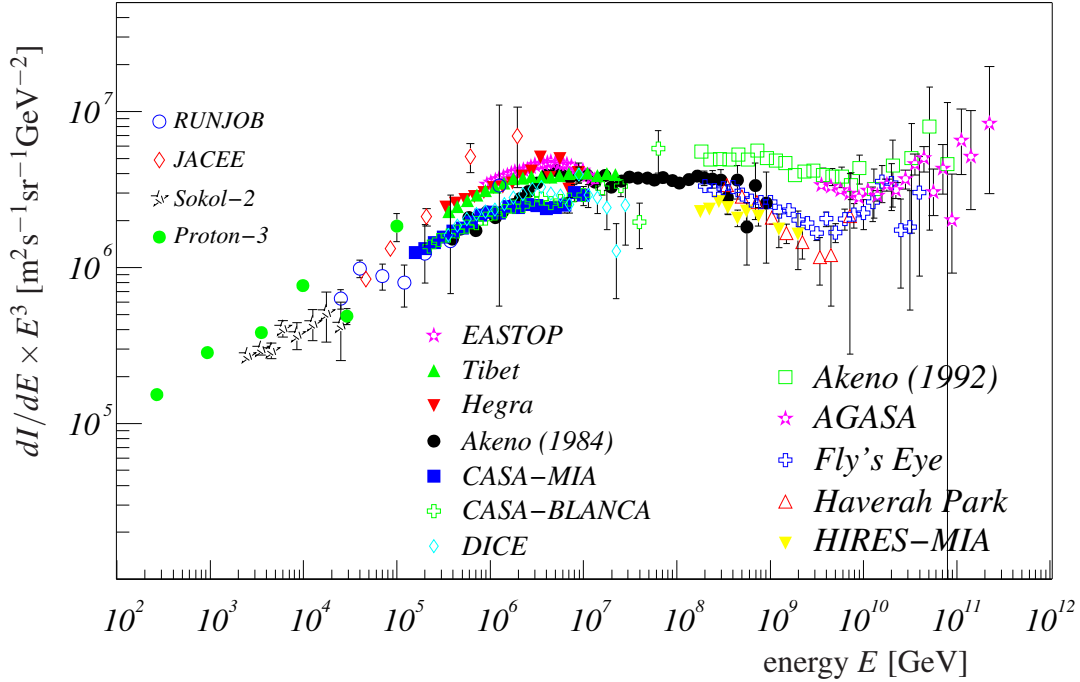
Figure 2.1: The energy spectrum of the cosmic radiation. Compilation by [Ulr04]. See [Ulr04] for the list of references for the experimental data.

Its shape is described by a simple power law

$$\frac{dN}{dE} \propto E^{-\gamma}. \tag{2.1}$$

Due to the steep decrease of the energy spectrum, the values have been multiplied by E^3 in order to be able to recognize structures in the flux spectrum. Up to energies of the primary particles of 10^{14} eV the spectral index of the flux spectrum is $\gamma \approx 2.7$.

At higher energies, above 10^{14} eV, the flux of primary particles becomes so low that the detectors on balloons or satellites with a sensitive detection area in the order of $1\,\text{m}^2$ are being hit by less than one particle per year only. At these energies, arrays of ground based particle detectors are necessary. Experiments of this type measure the shower of secondary particles resulting from an inelastic scattering between the incident cosmic ray particle and an air nucleus. The atmosphere above the detector arrays serves as the detection medium thus increasing the detection area considerably compared to balloon or satellite based experiments. These experiments are also called air shower arrays. They have a typical size in the order of a $1\,\text{km}^2$ and cover the energy spectrum including

the first irregularity at about 3×10^{15} eV. This irregularity is commonly referred to as the knee. At the knee the spectral index increases from $\gamma_{E < E_{knee}} \approx 2.7$ to $\gamma_{E > E_{knee}} \approx 3.1$. The origin of the knee is still unknown, although it has been studied since its discovery in 1958 [Kul59]. The data of the experiments Yakutsk [Knu06], HiRes-MIA [AZ01] and Fly's Eye stereo [Bir94] suggest the presence of a second knee at $E \approx 4 \times 10^{17}$ eV. The data describe a change of the spectral index from $\gamma \approx 3$ to $\gamma \approx 3.3$ at the second knee. The KASCADE experiment has been enlarged by the Grande array to especially study the cosmic radiation in this energy region in more detail.

In order to study the cosmic radiation in the highest regime of the primary particle energy, larger air shower arrays with a size of at least $1000\,\text{km}^2$ are used as well as telescopes which detect the fluorescence light generated by the secondary particles of the air showers. The Pierre Auger experiment [Abr04], for example, combines both experimental techniques to study primary particles with energies up to 10^{20} eV. These experiments cover a further irregularity in the energy spectrum at approximately 5×10^{18} eV, the so called ankle. The spectral index of the spectrum decreases at the ankle from $\gamma_{E < E_{ankle}} \approx 3.1$ to $\gamma_{E > E_{ankle}} \approx 2.75$. The ankle may be caused by the transition from a galactic to an extragalactic origin of the cosmic ray particles (e.g. [Ste99]).

The region of primary energy above 5×10^{19} eV is especially interesting due to calculations by Greisen, Zatsepin and Kuzmin [Gre66, Zat66]. They predict a cutoff, referred to as GZK-cutoff, of the energy spectrum at 5×10^{19} eV due to the energy loss of primary particles caused by interactions with the photons of the cosmic microwave background radiation. Above energies of 5×10^{19} eV the center-of-mass energy exceeds the energy threshold for photo-pion production and pair production. Ultra-high energy particles with an assumed extragalactic origin ($\gtrsim 50\,\text{Mpc}$) lose their energy in these processes until their energy has dropped below the energy threshold. The data from different experiments beyond 5×10^{19} eV are contradictory. The data from HiRes [Abb04], Fly's Eye [Bir94] and Yakutsk [Efi91] are consistent with the expected GZK-cutoff at 5×10^{19} eV. However, the data of AGASA [Tak98, Hay00] show an excess of events above 10^{20} eV indicating a continuing energy spectrum [Bah03].

2.2 Composition of cosmic rays

The chemical composition of cosmic rays is only known for energies below 10^{14} eV. Due to the low flux above this energy a direct measurement of the primary particles above 10^{14} eV is impossible. The composition of the cosmic radiation has been studied with highest precision by satellite and balloon experiments up to energies of $1\text{-}2\,\text{GeV/nucleon}$ [Sim83]. About 98 % of the cosmic radiation are hadrons. The rest is composed of electrons and γ radiation. The hadronic component is composed of 87 % protons and 12 % helium nuclei. The rest corresponds to fully ionized nuclei of heavy elements. Figure 2.2 shows a comparison of the relative elemental abundance in our solar system and in the cosmic radiation. The abundances are normalized to the abundance of silicon. The good agreement of the abundances for most elements suggests that the elements at the
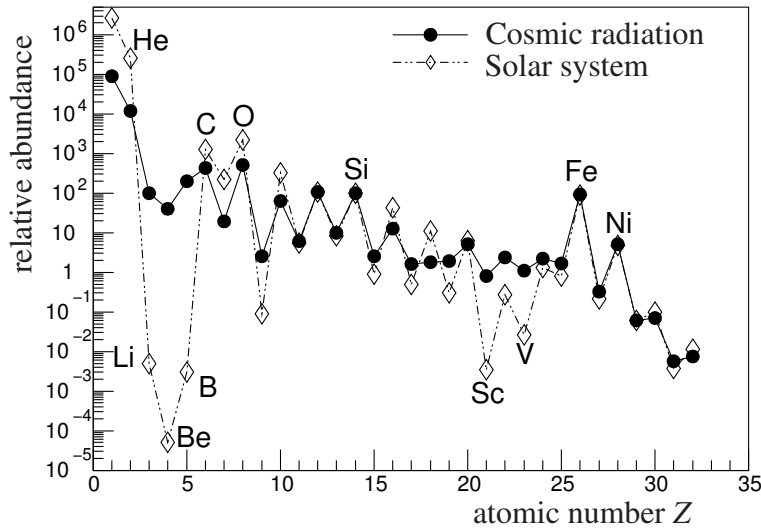
Figure 2.2: Comparison of the relative abundances of the chemical elements in our solar system and in the cosmic radiation [Wef91].

source are also products of the nucleosynthesis and that the abundances at the source are thus equal to the abundances in our solar system. However, a deviation of the abundance is seen for some elements. The lower abundance of hydrogen and helium in the cosmic radiation with respect to the abundance in our solar system probably originate from their relatively high ionization energies. Since the most popular acceleration processes (see next section) are only efficient for charged particles, it is assumed that only the ionized fraction of hydrogen and helium atoms is accelerated. Furthermore, an excess of the light elements Li, Be and B and the elements below iron ($Z < 26$) Sc, Ti, V and Mn is observed in the cosmic radiation. Only a small amount of these particles is produced by nucleosynthesis. They are produced by spallation in collisions of nuclei of the CNO and iron group with particles of the interstellar matter.

2.3   Acceleration and propagation

Contemporary theories for the acceleration of cosmic radiation creating a power law energy spectrum belong to one of the two categories, stochastic acceleration or direct acceleration. In stochastic processes many single interaction processes with little gain in particle energy per interaction sum up to accelerate charged particles to the high energies which are observed. In the direct acceleration models the cosmic particles are accelerated in a few, or even a single, very efficient step(s).

The underlying process of the stochastic acceleration is called 1st order Fermi acceleration [Fer49]. Shock fronts, which propagate into the interstellar medium, are the most popular candidates to form the necessary conditions. A shock front generates two regions of different magnetic field characteristics due to the compression of the medium behind the shock. By diffusive collision-less scattering at magnetic irregularities behind and in front of the shock front, charged particles cross the shock front many times. In

each crossing they gain an amount of energy proportional to the velocity of the shock front. Therefore, the maximum attainable energy of the particles depends on the velocity of the shock front and the number of reflections. The latter is limited by the lifetime of the shock front. See [Dru83] for a review of the theory of diffusive shock acceleration.

The most promising candidates for shock fronts are supernova blast waves propagating into the interstellar medium. For a recent review see [Hil05]. The model of acceleration by supernova shock waves is able to explain the observed characteristics of the cosmic radiation as for example their intensity and their chemical composition. It provides a power-law energy spectrum $E^{-\gamma}$ at the source with a spectral index $\gamma \approx 2$. The observed average frequency of three galactic supernovae per century results in a power of about 3×10^{35} J/s. Compared to the power of 5×10^{33} J/s mandatory to generate the observed energy density of the cosmic radiation of 1 eV/m^2, the energy emitted by a supernova has to be transformed into the acceleration of cosmic radiation with a reasonable efficiency of a few percent. Recent measurements support the model of cosmic ray acceleration by supernova remnants [Eno02, Aha04]. Other environments for the occurrence of shock fronts are the termination shock of a stellar wind [Ces83] or the termination shock of a galactic wind [Jok87]. In a binary system with a pulsar, a shock front is generated due to the interaction between the pulsar wind and the atmosphere of the companion star [Har90]. More detailed calculations have shown that all these galactic candidate sites for acceleration of cosmic rays are able to reach a maximum energy in the order of maximal 10^{16} eV.

The non-stochastic direct acceleration models require the presence of strong magnetic and electric fields. Potential environments with such conditions are found at the polar caps of rapidly spinning pulsars [Che86] or within relativistic jets from Active Galactic Nuclei (AGN) [Rac93]. Another model assumes that the highly relativistic matter emitted by supernovae as jets accelerates the cosmic ray particles [Dar06]. Furthermore, so-called top-down scenarios have been developed to explain the origin of cosmic radiation with still undiscovered phenomena like the decay of so far unknown ultra-heavy particles. In [Sig03] a review of top-down scenarios is given. The top-down models and models describing extra-galactic origins of the cosmic ray particles, e.g. from AGNs, predict primary energies above 10^{16} eV.

The lifetimes of cosmic ray particles are longer than the time they need to cross the thickness of the galactic plane (≈ 0.2 kpc) straightly. This and the measured isotropy of the cosmic radiation suggests a diffusive propagation of the charged particles from the sources to the earth. On their way they are deflected by galactic magnetic fields and their original direction is lost when they arrive at the earth. The particle energy changes during propagation due to collisions, decay and ionization processes. Furthermore, particles escape with an energy dependent probability from the galaxy. All this affects the energy spectrum of cosmic rays and causes that the spectral index at the source of $\gamma \approx 2$ increases to $\gamma \approx 2.7$ observed at earth. The composition of the cosmic ray particles changes due to decay and spallation.

2.4   Origin of the knee

The reason for the knee in the energy spectrum is still unknown. Various models exist which roughly belong to three different categories. The first category states that the knee is an effect of the related acceleration mechanism. The second category explains the knee with properties of the cosmic ray propagation. The last category employs new physics. A brief overview of the models is given in the following.

Models which predict the knee as a feature of the underlying acceleration mechanisms are strongly connected to the models of diffusive shock acceleration. These models predict an energy limit for accelerated cosmic rays depending on the properties of the shock front and the surrounding medium [Ber99, Sta93, Kob02]. The models explain the knee in the primary energy spectrum at a few PeV as the maximum attainable energy for cosmic ray particles with a galactic origin. The acceleration rate of cosmic ray particles increases with decreasing time between two consecutive crossings of the shock front. This time is proportional to the Larmor radius $\propto 1/Z$ of the particles. Therefore, in all models, the maximum achievable energy depends on the charge Z of the accelerated cosmic ray particle. Hence, the position of the knee in the energy spectra of the individual primary elements varies with the charge Z of the incident particles.

Other models explain the knee as an effect of the propagation of the cosmic ray particles. An increasing leakage from the galaxy is assumed which is caused by a change in the confinement efficiency of cosmic ray particles by galactic magnetic fields. This change is a result of the presence of an irregular magnetic field superimposing the regular galactic magnetic field [Ptu93, Ogi03, Rou04]. The result of this additional random component is a drift of the cosmic ray particles. This drift increases rapidly with the energy of the cosmic ray particles and leads to a leakage of the particles from the galaxy for energies above $\approx 3\,\mathrm{PeV}$, which causes the knee. The drift depends on the energy per unit charge E/Z. Therefore, the position of the knee in the energy spectra of the individual primary elements is proportional to Z, too. Other effects during the propagation which may cause the knee are energy losses of the cosmic ray particles due to the onset of photo-disintegration by soft photons around the sources [Tka01, Can02]. The cross-sections for such interactions depend on the energy per nucleon E/A. Contrary to the aforementioned models, this yields a dependence on the atomic mass A of the position of the knee in the energy spectra of the individual primary elements.

The following models employ new particle physics processes or not yet confirmed assumptions about the properties of the particles involved.

A theory which provides also a second knee is proposed by [Wig00]. The threshold energy for the proton destruction process $p + \bar{v}_e \rightarrow n + e^+$ made possible by massive neutrinos corresponds to the knee energy of $3\,\mathrm{PeV}$ if the neutrino mass is assumed to be $m_v = 0.4\,\mathrm{eV}$. The second knee corresponds to the threshold energy for the same reaction for helium nuclei and is expected at $\approx 3 \times 10^{17}\,\mathrm{eV}$.

A completely different approach involves new particle physics in the atmosphere. In

these models a fraction of the energy of the primary hadronic interaction dissipates into unobserved channels of the initiated air shower. These channels are represented by the production of so far undetected heavy particles [Kaz01]. Alternatively, low scale gravitation is suggested as new physics in the particle interactions [Kaz03]. Since the new particles are not measured by conventional detectors, the primary energy is underestimated, which causes the knee in the reconstructed energy spectrum.

The last mentioned models depend all on the corresponding interaction cross-sections, which in turn depend on the energy per nucleon E/A. Therefore, they all predict a knee position for the energy spectra of the individual primary elements proportional to the atomic mass A.

2.5 Extensive air showers

Cosmic rays with an energy exceeding 10^{14} eV are being studied by measuring showers of secondary particles. These showers are initiated by the interaction of the primary cosmic particles with nuclei in the upper atmosphere. The existence of these extensive air showers (EAS) has been discovered in 1939, when coincident signals from spatially separated detectors for cosmic radiation were measured [Aug39].

An extensive air shower starts with the first hadronic interaction of the primary particle with an air nucleus. The probability for an interaction depends on the inelastic cross-section for the primary-air nucleus reaction. This cross-section determines the mean free path length of the primary in the atmosphere. The cross-section depends on the energy of the primary and the probability of an interaction depends on the density of the atmosphere. The height above ground of the first interaction at fixed primary energy therefore fluctuates according to the underlying interaction probability distributions.

The development of an extensive air shower consists of a superposition of cascades of particle production by interaction processes and particle decays. An air shower is composed of many types of different secondary particles which can be divided into three major components – the hadronic, the electromagnetic and the muonic component.

The hadronic component
While the hadronic component constitutes only about 1 % of the total number of particles in the shower, it has by far the largest impact on the shower development as it serves as the origin of the other shower components.

The first secondary hadrons are produced in the strong interaction of the primary with an air nucleus. Those secondary hadrons, which live long enough to undergo a subsequent interaction before decaying, will produce further generations of secondaries when they interact with air nuclei. As this interaction process occurs repeatedly as the shower propagates towards the observation level, a hadronic cascade evolves in which the number of hadrons increases with atmospheric depth, eventually reaches a maximum and then

decreases exponentially. Because the atmosphere corresponds to about 11 hadronic interaction lengths, only air showers generated by primaries of sufficiently high energies reach the observation level at approximately sea level.

The majority of hadronic particles are neutral and charged pions, followed by kaons, baryons like protons and neutrons and nucleonic fragments. Secondary hadrons are produced with a mean transverse momentum of about 400 MeV/c, which is small compared to the overall momentum. Thus, a shower core of highly energetic hadrons with a radius of less than 20 m is formed, which propagates along the line of flight of the incident primary – the shower axis. Only low energy hadrons ($E < 10$ GeV), especially neutrons, show a broad lateral distribution of up to 1 km as their relative transverse momenta compared to their longitudinal momenta are not negligible anymore.

The hadronic component feeds the electromagnetic component predominantly through the decay of neutral pions into two photons. The muonic component is generated by the decays of charged mesons.

The electromagnetic component
As discussed above, the electromagnetic component is initiated by the hadronic component. Neutral pions decay into two photons, starting an electromagnetic cascade in which photons produce electrons and positrons via pair production

$$\gamma + \text{nucleus} \longrightarrow \text{nucleus} + e^+ + e^-,$$
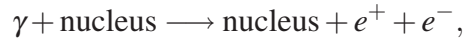
and electrons and positrons produce in turn photons via bremsstrahlung

$$e^\pm + \text{nucleus} \longrightarrow \text{nucleus} + e^\pm + \gamma.$$
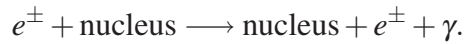
Successively, these two processes alternate and an electromagnetic subcascade develops. Since neutral pions are continuously produced along the shower axis, the longitudinal development of the number of electromagnetic particles is determined by the superposition of the electromagnetic subcascades, which each follow from pion decays. The number of electromagnetic particles multiplies so rapidly that they become the most numerous particles in the shower. The longitudinal development of the electromagnetic component in an air shower initiated by a photon of energy E_0 is described by

$$N_e(E_0, t) = \frac{0.31}{\beta_0^{1/2}} \exp\left(t(1 - \frac{3}{2}\ln s)\right)$$

with t being the atmospheric depth measured in radiation lengths X_0 ($X_0 = 37.15$ g cm^{-2} for air [Lin85]), $s \simeq 3t/(t + 2\beta_0)$ and $\beta_0 = \ln(E_0/E_{\text{crit}})$ [Gre56]. The parameter s is referred to as the age parameter. Its value is $s = 0$ at the beginning of the air shower and becomes $s = 1$ at the shower maximum. For $s > 1$ the number of shower particles declines. The energy E_{crit} is the critical energy at which the energy loss rate via ionization is equal to the energy loss rate via bremsstrahlung and corresponds to $E_{\text{crit}} = 84.2$ MeV in air.

The particle number of the electromagnetic component reaches a pronounced maximum as shown on the left hand side of figure 2.3. The atmospheric depth t_{max}, at
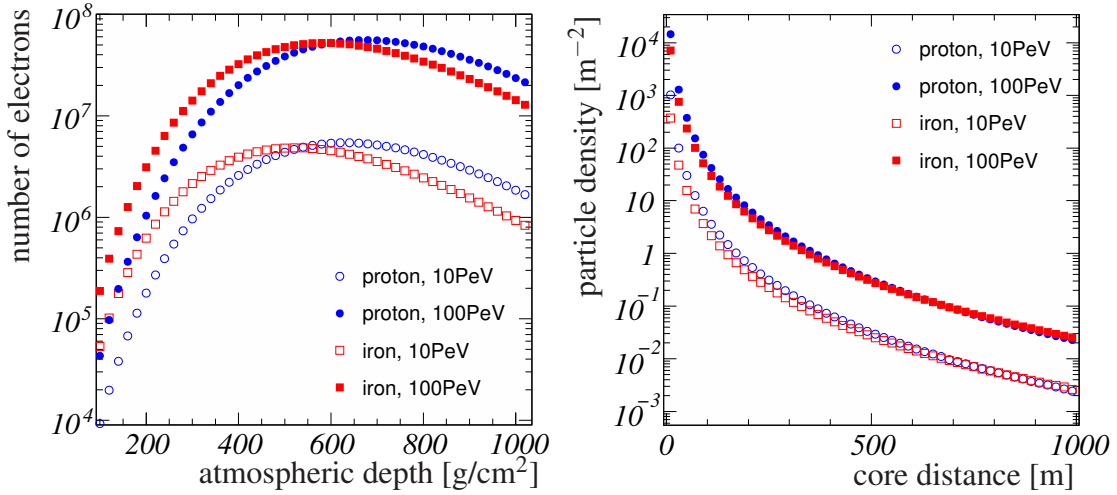
Figure 2.3: *Left:* Average longitudinal distribution of electrons. *Right:* Average lateral distribution of electrons. The distributions have been generated by averaging 50 simulated air showers for each primary particle and each primary energy. The air showers have been simulated with the air shower simulation program CORSIKA [Hec98].

which this maximum occurs, increases logarithmically with the primary energy $t_{max} \propto \ln(E_{prim}/E_{crit})$. The total atmospheric depth corresponds on average to 27 radiation lengths. For a vertical shower initiated by a primary of 10^{15} eV the maximum occurs at a depth of $t_{max} \approx 16$ radiation lengths, which translates into a height of about 5 km above ground. A primary of 10^{20} eV produces an air shower having its maximum at sea level. The number of particles at the shower maximum depends linearly on the primary energy $N_e^{max} \propto E_{prim}$. After the maximum the number of particles declines rapidly as the energy of more and more particles reaches the critical energy E_{crit}.

During the longitudinal development of the air shower, the electromagnetic component spreads laterally due to Coulomb scattering. The determining factor for the lateral spread is the Molière radius r_M, which is $r_M = 79$ m at sea level. The lateral extent of the electromagnetic component is described by the NKG-function (J. Nishimura, K. Kamata and K. Greisen) [Gre56, Kam58]

$$\rho_e(r) = \frac{\Gamma(4.5 - s)}{\Gamma(s)\Gamma(4.5 - s)} \times \frac{N_e}{2\pi r^2} \times \left(\frac{r}{r_M}\right)^{s-2} \left(1 + \frac{r}{r_M}\right)^{s-4.5} \qquad (2.2)$$

with the electron density ρ_e at distance r from the shower axis and N_e the total number of electrons at observation level. The NKG-function was determined for purely electromagnetic showers, but it describes air showers initiated by hadrons as well with different parameters. For the reconstruction of KASCADE-Grande data, a slightly modified NKG-function is used, which will be presented in chapter 5. The right hand part of figure 2.3 shows the lateral density distribution of electrons averaged over 50 simulated air showers for two primaries and two primary energies.

The muonic component

The muonic component is generated by the decays of mesons of the hadronic component. The muon gain from the decays of charged pions dominates, but also charged and neutral kaons decay into muons, either directly or via a prior decay into pions:

$$
\begin{aligned}
\pi^{\pm} &\longrightarrow \mu^{\pm} + \nu_{\mu}(\bar{\nu}_{\mu}) \quad (\approx 99.99\,\%), \\
K^{\pm} &\longrightarrow \mu^{\pm} + \nu_{\mu}(\bar{\nu}_{\mu}) \quad (\approx 63.5\,\%), \\
&\longrightarrow \pi^{0} + \mu^{\pm} + \nu_{\mu}(\bar{\nu}_{\mu}) \quad (\approx 3.2\,\%), \\
K_{L}^{0} &\longrightarrow \pi^{\mp} + \mu^{\pm} + \nu_{\mu}(\bar{\nu}_{\mu}) \quad (\approx 3.2\,\%).
\end{aligned}
$$
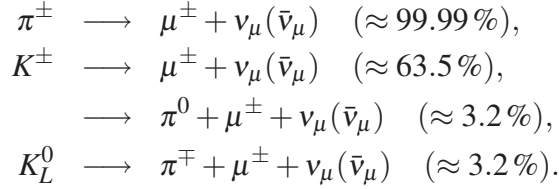
Whether a meson either decays or interacts depends on the relative magnitudes of its mean decay length and its mean free path length with respect to hadronic interactions. Both depend on the density of the atmosphere. In the early phase of the shower development, the atmosphere is still of low density, causing the mean free path length to be considerably larger than the mean decay length, hence making a decay more probable than an interaction. Especially, high energy muons ($E > 100\,\mathrm{GeV}$) originate from this early stage of the shower development.

Low energy muons also feed the soft electromagnetic component via their decays into an electron and a neutrino

$$
\mu^{\pm} \longrightarrow e^{\pm} + \bar{\nu}_{\mu}(\nu_{\mu}) + \nu_{e}(\bar{\nu}_{e}). \tag{2.3}
$$
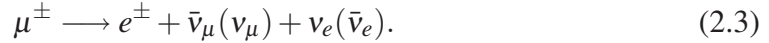
The longitudinal development of the muonic component shows a less pronounced maximum as seen in the left part of figure 2.4. There is no steep increase in the muon num-
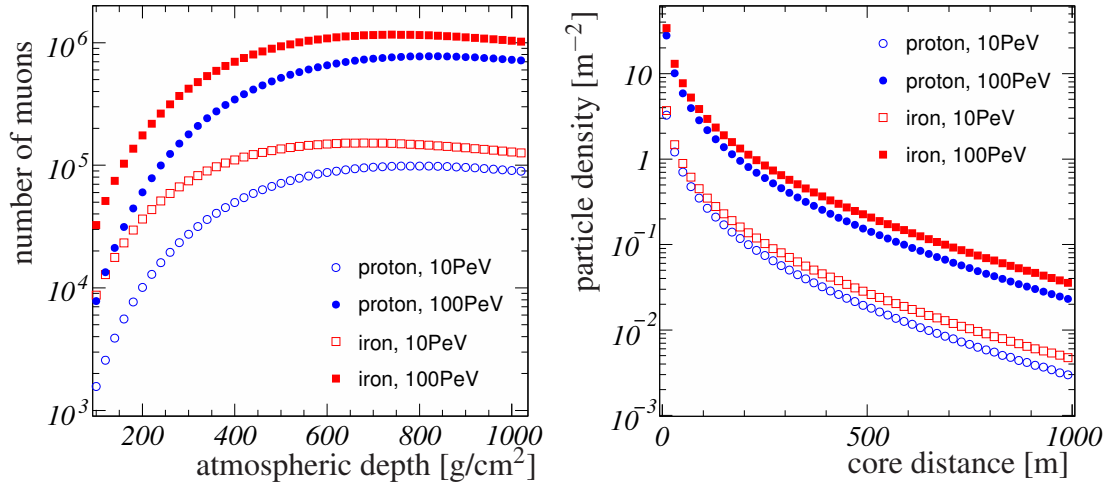
Figure 2.4: *Left:* Average longitudinal distribution of muons. *Right:* Average lateral distribution of muons. The distributions have been generated by averaging 50 simulated air showers for each primary particle and each primary energy. The air showers have been simulated with CORSIKA [Hec98].

ber since muons do not multiply. After the maximum, the number of muons decreases slowly and rather resembles a plateau since the muons do not vanish in interactions but

only lose their energy slowly by ionization. The decrease of the number of high energy muons via decay is suppressed since with the muon energy also the related relativistic time dilatation increases. The lifetime of high energy muons is thus prolonged and their decay in the atmosphere becomes unlikely.

The lateral spread of the muon component is mainly caused by the transverse momenta of the parent mesons. To a lesser extend also multiple scattering contributes, but it is suppressed by a factor of $(m_e/m_\mu)^2$ compared to electrons. This suppression and because muons are not affected by the strong interaction keeps them traveling almost undisturbed along straight lines through the atmosphere. High energy muons inherit their transverse momenta from their parent mesons, which defines eventually the lateral distributions of muons. The lateral spread increases for muons of lower energies. The function used to describe the lateral density distribution of muons is similar to the one proposed in [Lag01]. It will be presented in chapter 5. The right hand part of figure 2.4 shows the lateral density distribution of muons averaged over 50 simulated air showers for two primaries and two primary energies.

Arrival times of the electromagnetic and muonic shower component
An extensive air shower is regarded as a disk of secondary particles of increasing lateral and longitudinal extension as it propagates through the atmosphere. However, the disk is not flat but has a specific curvature. In a vertical air shower, secondary particles close to the shower axis hit the observation level first. Particles at a certain distance from the shower axis arrive with a time delay due to the curvature of the shower disk.

Shower particles close to the shower core have to travel the shortest path from the point of their generation to the observation level. With increasing core distance of the secondary particles, the path length increases, which causes particles to arrive later than particles closer to the shower center. The difference in the path lengths causes the curvature of the shower front. The path length difference also contributes to the longitudinal spread, i.e. the thickness of the shower front. For a fixed distance to the shower core, particles which are produced deeper in the atmosphere have longer path lengths with respect to the point of the first interaction than particles generated higher in the atmosphere reaching the observation level directly. Furthermore, the velocities of the secondaries produced at different heights are not constant but vary, which translates directly into a difference in the arrival times at the observation level.

The differences in the shower development of the electromagnetic shower component and the muonic shower component suggests an arrival time difference between electrons and muons at the observation level. According to the model of the shower development, muons are on average produced higher in the atmosphere and move under the production angle with respect to the shower axis rectilinearly towards the observation point. The electromagnetic particles are on average produced deeper in the atmosphere and close to the shower axis. They reach the observation point by multiple scattering creating longer path lengths and thus longer times of flight. Furthermore, electromagnetic particles which are produced at the early phase of the shower development are absorbed in the atmosphere before they reach the observation level. Therefore, the bulk of elec-
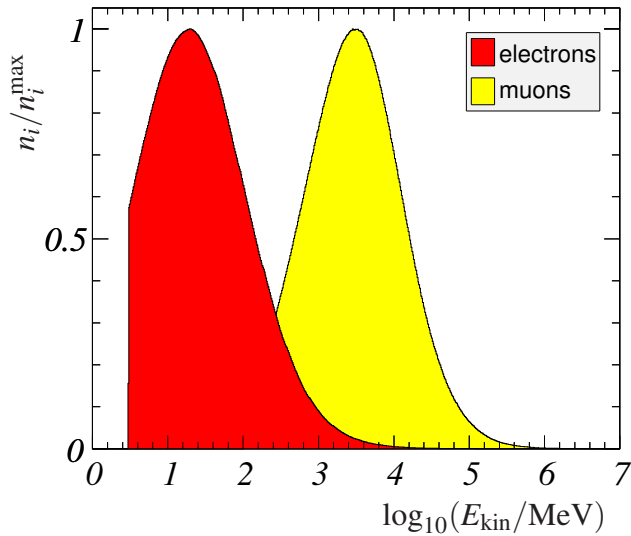
Figure 2.5: Distributions of the kinetic energy of electrons and muons for simulated air showers. Fifty proton showers and fifty iron showers have been simulated with CORSIKA [Hec98] for each of the two primary energies 10^{16} eV and 10^{17} eV. The edge of the distribution for electrons is caused by the cutoff energy chosen in the CORSIKA program. Particles below this energy are not further tracked. For comparison, the distributions have been scaled by 1/maximum.

tromagnetic particles, which are detected at ground level, are produced deeper in the atmosphere or at a later stage of the shower development. At this point, the energy available for the production of secondaries has already decreased. Hence, the average kinetic energy of the electromagnetic particles is smaller than the kinetic energy of the muons. In figure 2.5 the distributions of the kinetic energy for electrons and muons are shown for simulated proton and iron air showers with primary energies of 10^{16} eV and 10^{17} eV. The resulting effect of the different development of the electromagnetic and the muonic shower component is that muons arrive earlier at the observation level than particles of the electromagnetic shower component. The difference in the arrival time increases with the radial distance from the shower core. The effect of the shower development on the shape of the shower disk and on the arrival times of electrons and muons is depicted in figure 2.6.
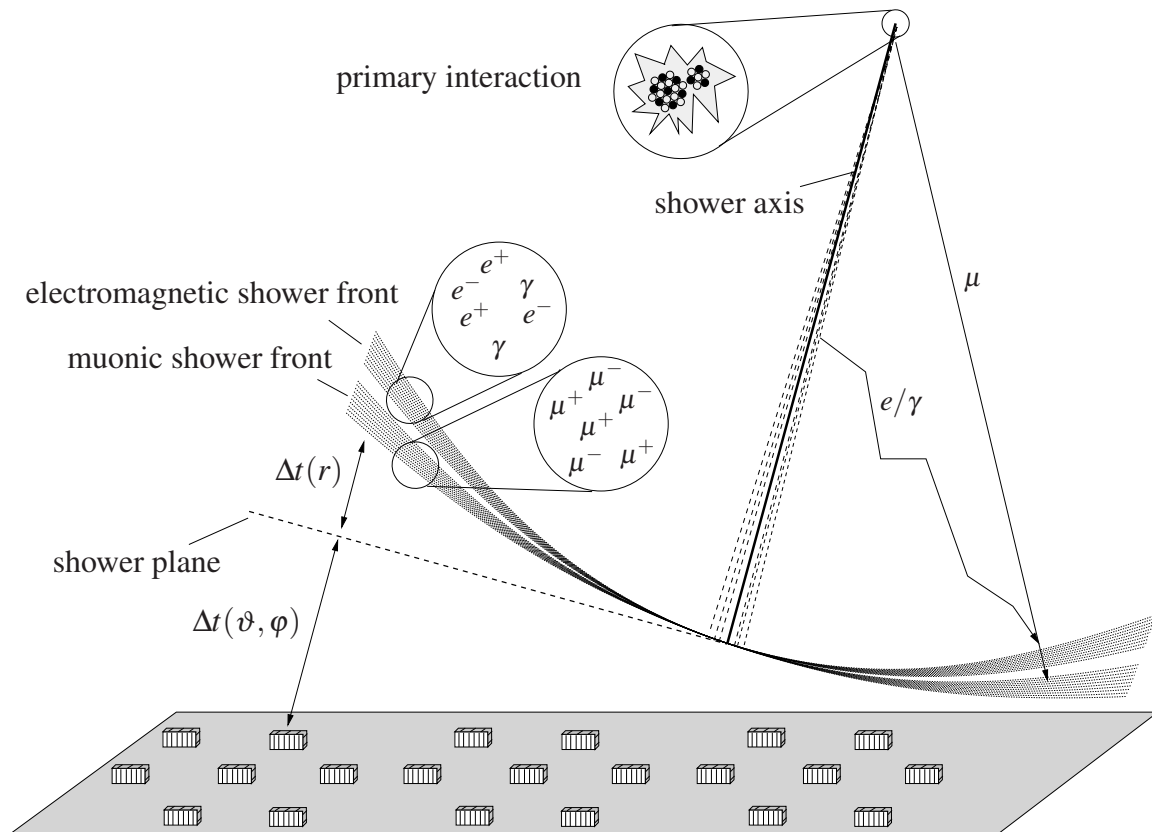
Figure 2.6: Scheme of the shower development in the atmosphere. Electrons have to cross a longer path length with respect to the point of the first interaction than muons to reach the same core distance. This leads to a time delay of the electrons. The difference in path length and thus also the time delay of electrons increases with the distance from the shower core.

The KASCADE-Grande experiment

The KASCADE-Grande experiment, depicted in figure 3.1, is a multi-detector setup dedicated to measure the electromagnetic, muonic and hadronic components of extensive air showers. It is located at the Forschungszentrum Karlsruhe, Germany (at 110 m above sea level, 49° N, 8° E). The main aim of KASCADE-Grande is the analysis of the chemical composition of primary cosmic radiation in the energy range of 10^{14} eV to 10^{18} eV. The experiment consists of the KASCADE experiment, the Grande array and the Piccolo trigger array. The KASCADE (KArlsruhe Shower Core and Array DEtector) experiment itself is a combination of three subdetectors [Ant03b]. It was designed to investigate primary cosmic radiation in the energy range of 10^{14} eV to 10^{17} eV which includes the knee in the cosmic ray energy spectrum. The KASCADE experiment is taking data since 1996. In the analysis of the chemical composition of primary cosmic radiation with data from KASCADE a knee structure in the energy spectra of the light mass groups has been found [Ant05]. An extrapolation of the knee positions from light primaries to heavy primaries suggests a knee structure at about 10^{17} eV, the upper energy limit of KASCADE, where the statistics of measured air showers is low. In order to increase the statistics in the energy region of 10^{17} eV the detection area was enlarged by an array of 37 detector stations, the Grande array. The Grande detector stations are scintillation detector stations re-used from the EAS-TOP experiment [Agl89, Agl93], which finished its operation in 2000. The third part of KASCADE-Grande, the Piccolo array, provides a fast trigger signal to the muon tracking detector and the central detector of KASCADE to assure a measurement in coincidence with the Grande array. In the next paragraphs the subdetectors of KASCADE-Grande are described in more detail.
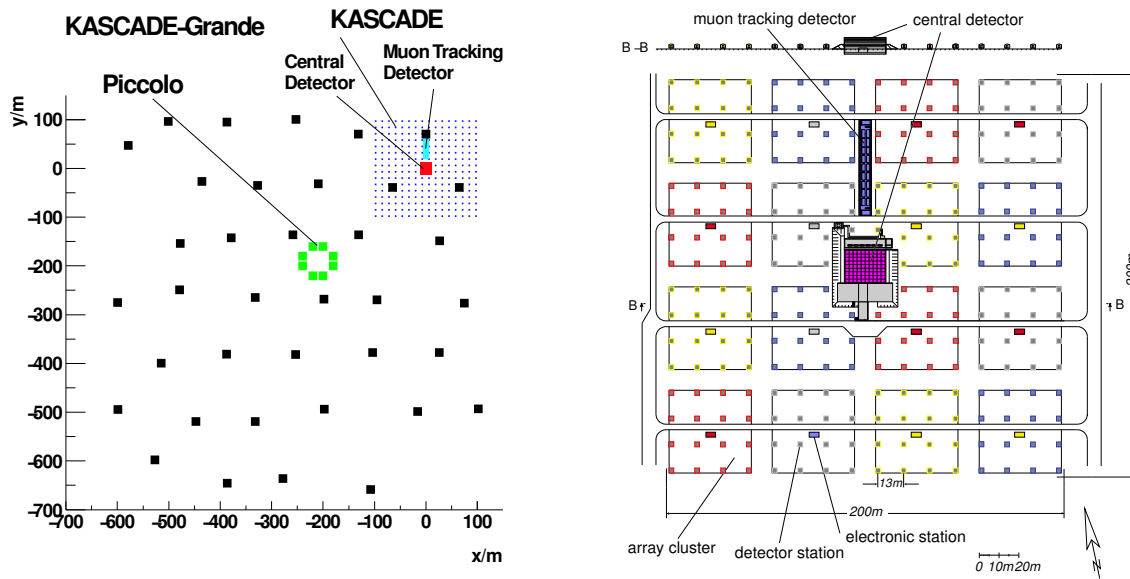
Figure 3.1: *Left:* Schematic top view of the KASCADE-Grande experiment [Hau03]. *Right:* The KASCADE experiment and its subdetectors [Ant03b]. The figure also shows the separation of the KASCADE array into sixteen clusters of 16 or 15 stations. The lower left cluster is cluster 1. In this cluster the FADC system is installed (see chapter 4), which provides the data analyzed in this thesis.

3.1 The KASCADE experiment

Three major components form the KASCADE experiment. These are the KASCADE scintillator array, the central detector and the muon tracking detector. Each of these subdetectors is specialized in measuring a certain component of extensive air showers and has dedicated tasks to fulfill regarding the reconstruction of air shower observables. The array mainly measures the electromagnetic and muonic components of an air shower. The main part of the central detector, the hadron calorimeter, focuses on the measurement of the hadronic component of air showers. The muon tracking detector is a shielded underground detector and thus measures muon tracks only. Since the analysis presented in this thesis is based on a FADC (Flash Analog to Digital Converter) system which is integrated in the KASCADE array, the central detector as well as the muon tracking detector are only briefly described before the KASCADE array is described in more detail.

3.1.1 The central detector

The central detector as a whole is displayed in figure 3.2. It covers an area of about $320\,\mathrm{m}^2$ to assure a detection rate of about 100 particles per year at $10^{16}\,\mathrm{eV}$ and consists of a combination of subdetectors. It is mainly formed by a sampling hadron calorimeter composed of warm-liquid ionization chambers placed between eight layers of iron
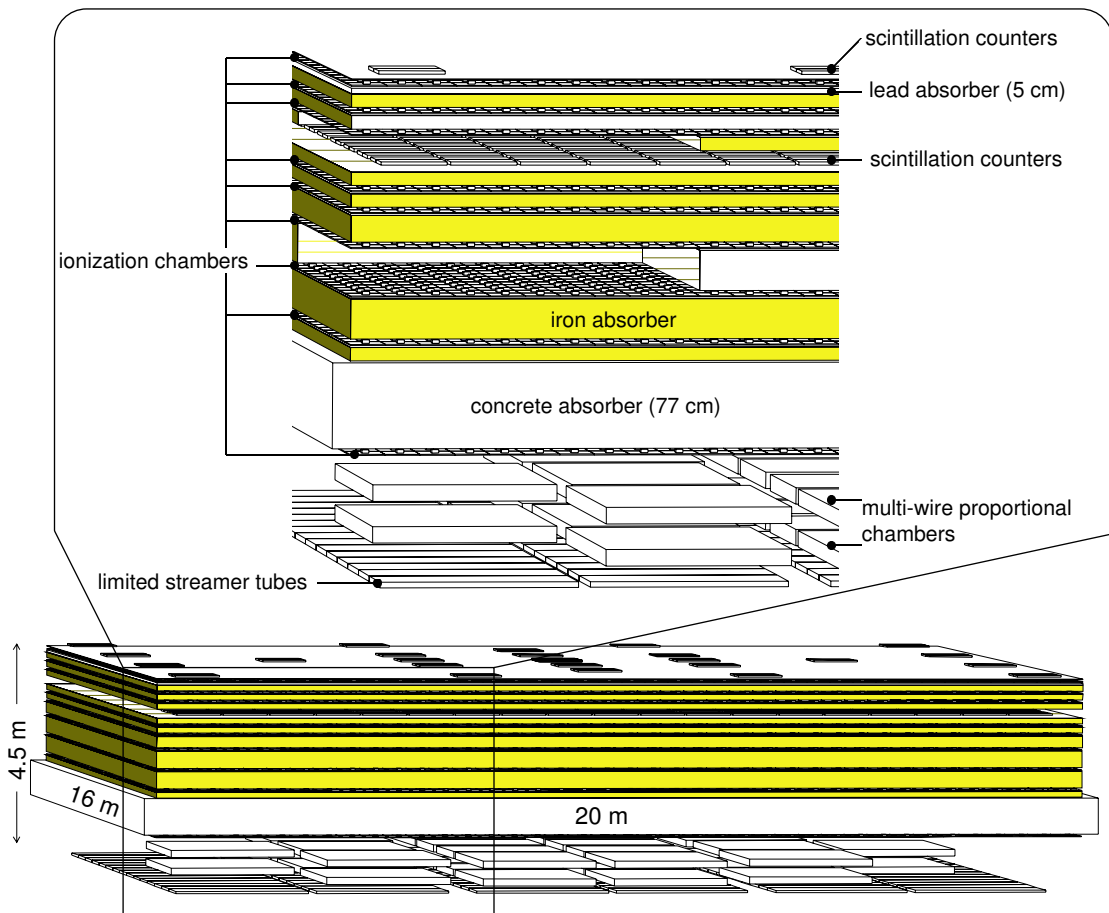
Figure 3.2: Scheme of the central detector with its subdetectors [Ant03b].

absorber. The most upper cluster of scintillators, the top cluster, is placed on top of the first layer of ionization chambers, which is mounted onto the first absorber layer made of lead. Beneath the third absorber layer a layer of plastic scintillators forms the trigger plane. Finally, a combination of multi-wire proportional chambers and a layer of limited streamer tubes located in the basement of the central detector form the muon chamber system. The central detector provides good resolution of the shower core position. By combining the information from all subdetectors of the central detector a detailed study of the characteristics of EAS cores is performed.

Hadron calorimeter: The hadron calorimeter consists of about 11000 liquid ionization chambers filled with purified tetramethylsilane (TMS) or tetramethylpentane (TMP). These liquids provide a high dynamic range and long-term stability as well as a high signal yield. The calorimeter's thickness corresponds to 11.5 nuclear interaction lengths in vertical direction in order to provide a sufficiently high energy resolution and a reasonable shower containment for hadrons up to 25 TeV. To enable the measurement of the lateral dependence of the hadron density in the shower core and to determine the energy of individual hadrons, the hadron calorimeter is designed with an appropriately fine segmentation [Eng99].

Top cluster and top layer: The top cluster is formed by 25 scintillation counters, made of two 3 cm thick scintillator [1] slabs. The light is coupled out by a central wavelength shifter bar and measured by a single photomultiplier[2]. Its purpose is to fill the gap of the four missing array stations in the center of the KASCADE array and to trigger the measurement of small extensive air showers [Hae96].

Below the top cluster and still above the first layer of absorber a layer of liquid ionization chambers with full surface coverage – the top layer – is installed. Since these chambers have twice the active thickness of liquid (TMP) compared to the calorimeter chambers, the top layer provides a good separation of minimum ionizing particles from noise. The purpose of the top layer is the precise determination of the shower core position especially for small air showers [Ris00, Ric03].

Trigger plane: The trigger plane is located below the third absorber and serves as a fast trigger source for all subdetectors of the central detector. It is made out of 456 scintillation detectors of the same type as those forming the top cluster. It covers 64 % of the calorimeter area. The total amount of absorber material above the trigger plane corresponds to 30 radiation lengths. This translates into a kinetic energy threshold of 490 MeV for vertical muons and represents an efficient shielding against the electromagnetic component. Two different trigger conditions are implemented. High energy hadron events are triggered by the detection of an energy deposit exceeding 50 muon equivalents in a single scintillator. Air shower events are triggered by a coincidence of eight or more scintillation detectors seeing at least one muon equivalent. The trigger plane is used to measure muon densities in the center of the KASCADE experiment and to reconstruct arrival time distributions of muons above 2 GeV [Bre98].

Muon chamber systems: Below the iron sampling calorimeter two layers of 16 multi-wire proportional chambers (MWPCs) are mounted [Boz01], each covering an area of $129 \, \mathrm{m}^2$. An argon-methane mixture is being used as counting gas. All material above the chambers – especially the layers of absorber material of the hadron calorimeter – are only passed by muons with an energy above an energy threshold of 2.4 GeV for vertical muons. The muon chamber system is thus used to measure the track parameters of high-energy muons in air showers. The two layers of MWPCs are vertically separated by a 38 cm wide gap which results in an angular accuracy of $\sigma_\vartheta = 1.5°$. The spatial resolution of $\sigma = 1.1$ cm for muon tracks is determined by the spacing of anode wires and the read-out strips.

Below the MWPCs a third layer of limited streamer tubes (LSTs) [Ant03a] belongs to the muon chamber system. The layer consists of six rows of 15 modules each. Its purpose is to reduce ambiguities in the muon track reconstruction for particle densities above $2 \, \mathrm{m}^{-2}$, especially close to the shower axis. The LSTs are of the same type as those used in the muon tracking detector, which is described in the next section. The only difference is the use of pure CO_2 as counting gas.

---

[1]NE 114
[2]EMI 9902

3.1.2   The muon tracking detector

The muon tracking detector is located north of the central detector. It has a length of 48 m, a width of 5.4 m and a height of 2.4 m. The shielding covering the detector consists of concrete, iron and soil and corresponds to 18 radiation lengths, i.e. an energy threshold of 800 MeV for vertical muons. A sketch of the detector is shown in figure 3.3. Sixteen towers made of 3 horizontally and 82 cm vertically mounted modules of
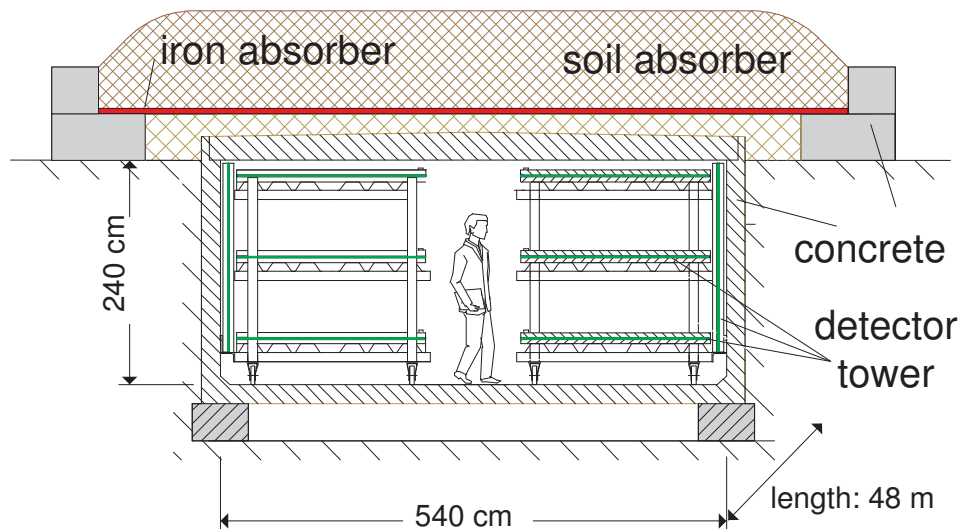
Figure 3.3: Schematic profile view of the muon tracking detector [Ant03b].

limited streamer tubes are arranged in two rows. The tubes are operated with a mixture of argon, isobutane and CO_2 as counting gas. The module design is explained in detail in [Dol02]. Each tower provides hit information of passing muons, which is used to reconstruct the corresponding tracks. Additional modules, which are mounted vertically next to the towers, provide the necessary hit information for the reconstruction of inclined tracks. The measured muon tracks are extrapolated in upward direction and are used to determine the muon production height by means of triangulation. The production height is in turn an observable which is sensitive to the mass of the primary cosmic particles. The setup reaches highest efficiency for vertical muons and, in this case, provides an effective detection area of 128 m^2 and a geometrical angular resolution of $0.35°$.

3.1.3   The KASCADE array

A 200×200 m^2 sized array of 252 detector stations with a grid size of 13 m forms the KASCADE array. It is subdivided into 16 clusters, as shown in the right part of figure 3.1. Each of the outer 12 clusters comprises 16 detector stations. The inner four clusters consist of 15 stations only, because the central detector occupies the area of the four missing stations. Apart from this difference, inner and outer clusters differ by the detector setup inside the detector stations.

Air showers, which have their core located inside the central detector, are of special interest, because they can be measured with the maximum number of observables provided by KASCADE. However, a disadvantage of these showers is, that it is not feasible to shield the μ-detectors close to the shower core against electromagnetic punch-through. The μ-detector data would be biased by the electromagnetic punch-through component which would prevent a proper determination of the μ-density. For this reason, the detector stations of the inner four clusters are not equipped with muon detectors. Instead, the muon tracking detector and the muon chamber system provide the muon information, since they are efficiently shielded against the electromagnetic shower component. The stations of the inner clusters house four stainless steel cones filled with liquid scintillator for the detection of the e/γ-component of air showers. This e/γ-detector is described in more detail below.

The stations of the 12 outer clusters use only two cones for the determination of the electromagnetic air shower component. Contrary to the stations in the inner clusters, below the e/γ-detectors two layers of iron and lead absorbers, 4 cm and 10 cm thick, are mounted. The absorber material corresponds to approximately 20 radiation lengths. It shields four plastic scintillator modules, which are used to measure the muon density in the detected extensive air showers.

A schematic view of an array detector station combining the features of both detector types is shown in figure 3.4.

The e/γ detector: The e/γ-detector in one detector station consists of four (inner clusters) or two (outer clusters) steel cones. A sketch of a sample cone describing its setup is shown in the upper right part of figure 3.4. The steel cones have a base diameter of 1 m. They cover an aluminum tank filled with (5 cm) liquid scintillator which is a mixture of paraffin and pseudocumene (PDP). The inner wall of the steel cone is covered with a light reflecting paint. Scintillation light emitted by the scintillator is reflected by the inner walls and guided upwards where it is gathered by a plexiglas light collector. A 3" diameter photomultiplier tube[3] (PMT) is attached to the light collector at the tip of the steel cone to convert the light into a current signal, further referred to as PMT signal. The PMT signal is decoupled twice, at the anode and, for lower amplification, at the last but two dynode. The anode signals of all four (or two) e/γ-detector cones are sent to the cluster's data acquisition electronics separately. The dynode current signals however are passively added and the sum is transmitted to the cluster DAQ electronics.

The volume above the liquid scintillator is filled with argon to prevent oxidation. To avoid a variation of the argon pressure inside the hermetically sealed cone due to temperature changes, a gas balancing bag capable of containing a maximal volume of 60 l of argon is attached to the cones. The steel cones are covered with lead foil of 3 mm thickness. Its purpose is to enhance the conversion probability for high energy photons in order to increase their detection probability. This improves the angular resolution by 60 % [May90, Wet95]. The time resolution of the e/γ-detector was determined to $\sigma = 0.77$ ns [Völ92].

---

[3]EMI 9822 or Valvo XP3462
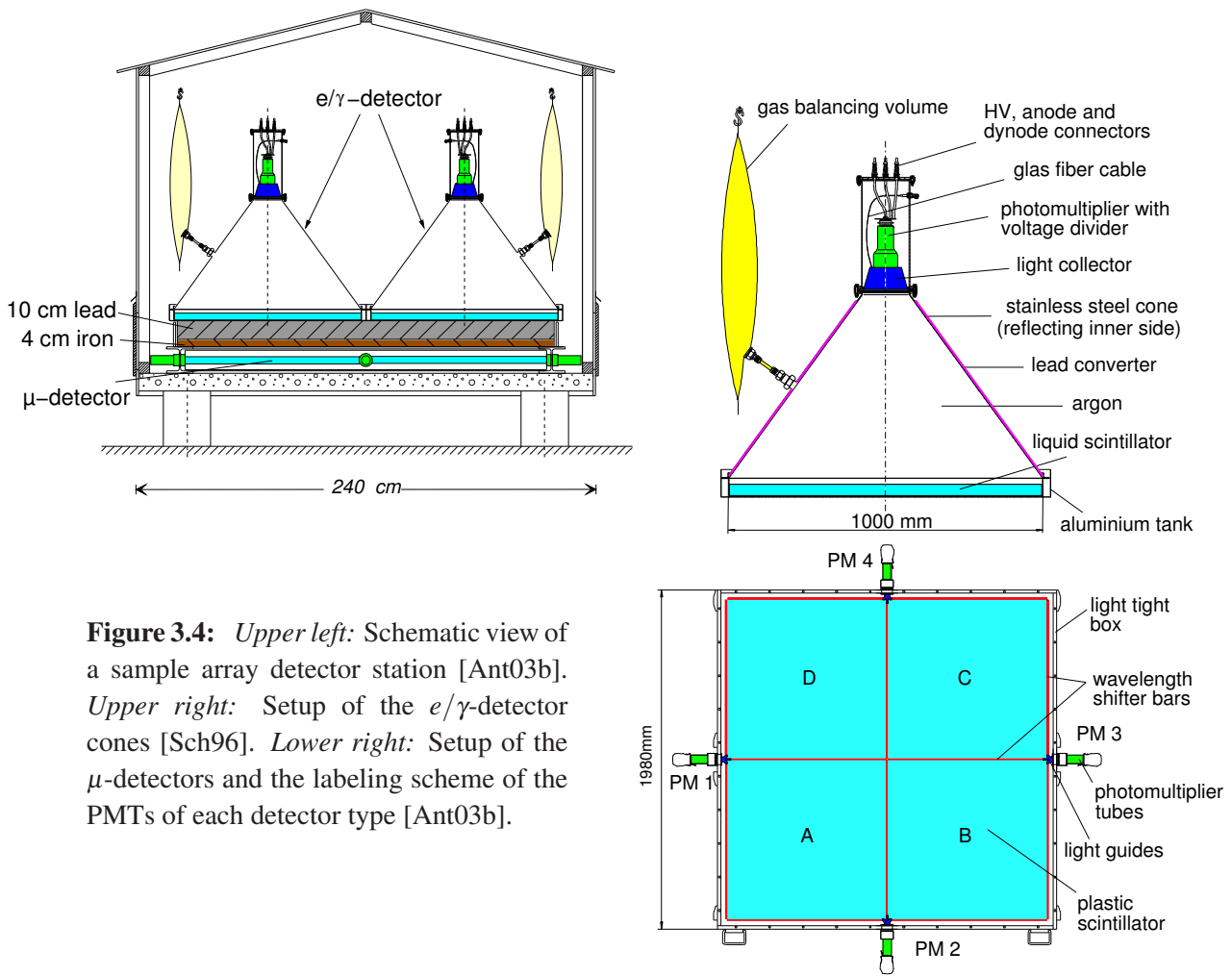
Figure 3.4: *Upper left:* Schematic view of a sample array detector station [Ant03b]. *Upper right:* Setup of the e/γ-detector cones [Sch96]. *Lower right:* Setup of the μ-detectors and the labeling scheme of the PMTs of each detector type [Ant03b].

With the help of optical fibers brought into each cone the relative time delays between the detectors belonging to one cluster is determined by triggering all detectors simultaneously with laser pulses from a calibration system.

The μ detector: In the lower right part of figure 3.4 a top view of the muon detector is given. Each muon detector of the KASCADE detector stations in the outer clusters is made from four quadratic segments of plastic scintillator[4] with a side length of 90 cm and of 3 cm thickness. They are covered by an absorber of 4 cm iron and 10 cm lead. Each side of the segments is being read-out by a wave length shifter bar. The light from three wave length shifter bars continues through a light guide which is connected to a PMT[5]. Hence, one PMT gathers the scintillation light of two segments. The time resolution of the μ-detector was determined to $\sigma = 2.9$ ns [Kri92].

The sketch of the muon detector also shows the labeling scheme for the PMTs of the μ-detector and e/γ-detector, respectively. The PMTs of the μ-detector are labeled counterclockwise from '1' to '4' starting with the PMT on the left hand side. The following

---

[4]Bicron BD-416
[5]EMI 9902 or Valvo XP2081

definitions are used to specify the individual μ-detector segments. The plastic scintillator segment between PMT 1 and 2 will be named '1|2'. Correspondingly, the others are named counterclockwise '2|3', '3|4' and '4|1'. The letters ('A'-'D') in the μ-detector segments refer to the e/γ-detector cones mounted above the corresponding segments. Therefore, the PMTs of the e/γ-detector are labeled with letters from 'A' to 'D' starting with the detector cone mounted above the lower left μ-detector segment '1|2'. Since the anode signals from all PMTs are transmitted to the data acquisition electronics separately, it is possible to generate for each detector station a hit pattern on an event-by-event basis for both detector types. This hit pattern is a bit string, which indicates which detector cone or segment measured a passage of at least one shower particle. If a bit in this hit pattern is set to '1', the corresponding detector part was active. Otherwise the bit is set to '0'. The least significant bit represents the μ-detector PMT '1' or the e/γ-detector PMT 'A', respectively. Accordingly, the most significant bit represents μ-PMT '4' or e/γ-PMT 'D'.

The KASCADE FADC system is installed in the outer array cluster 1 where the e/γ-detector of each station consists of the two e/γ-detector cones 'A' and 'C' only. For stations in the outer clusters, only the hit patterns listed in table 3.1 are possible. The

no. of active cones/segments	e/γ-detector hit pattern		active cones	μ-detector hit pattern		active segments	
1	0001	(1)	A	0011	(3)	1|2	
	0100	(4)	C	0110	(6)	2|3	
				1100	(12)	3|4	
				1001	(9)	4|1	
2	0101	(5)	A,C	0111	(7)	1|2,	2|3
				1110	(14)	2|3,	3|4
				1101	(13)	3|4,	4|1
				1011	(11)	4|1,	1|2
> 2				1111	(15)		

Table 3.1: Possible detector hit patterns for outer array clusters (e.g. cluster 1). The numbers in brackets correspond to the integer number represented by the hit pattern bit string.

hit patterns were used in two steps of the analysis. Firstly, for the determination of the average pulse shape of a single particle passing the detector (see chapter 7). Secondly, it is used to calculate an average detector calibration in order to adjust the average single particle detector response dynamically to the actual detector performance (see also chapter 7).

Cluster electronics: To each cluster of the KASCADE array belongs an air conditioned station housing the data acquisition (DAQ) electronics for the detector signals. This station will in the following be referred to as the electronics station. As figure 3.1 shows, the electronics stations are located at the cluster centers.

The DAQ electronics in these stations comprises KASCADE Front-End-Electronics (KAFE) modules, a clock module and a trigger unit. The KAFE modules are linked to the detectors and are responsible for receiving and processing the incoming anode and dynode signals. The clock module receives the 1 Hz and 5 MHz clock signals from the central clock distributor and forwards them to the KAFE modules and the trigger unit. Each of these modules run counters for both clock signals. The 1 Hz clock counter – further referred to as Global Time (GT) – represents the number of seconds since 1970/01/01. The 5 MHz clock counter, in the following referred to as Time Label (TL), counts the number of 5 MHz cycles since the last 1 Hz clock cycle, thus dividing the seconds into 200 ns intervals. The trigger unit generates trigger signals if a trigger condition in the local cluster is fulfilled. It sends the trigger signal to the central trigger distributor, which forwards it via dedicated trigger lines to each subdetector of the experiment. If the trigger unit detects a valid trigger condition or receives an external trigger signal from the central trigger distributor, it stores the current values of the 1 Hz and 5 MHz clock counters. These counter values are used as time stamp for the measured event data.

Each electronics station receives and processes the PMT signals from the detectors of the 16 (outer clusters) or 15 (inner clusters) detector stations. A fully equipped detector station would transmit 9 signals into the electronics station:

- four anode signals of the e/γ-PMTs,

- one dynode sum signal of the e/γ-PMTs,

- four anode signals of the μ-PMTs.

The signals are received by the KASCADE Front-End-Electronics (KAFE) modules. One KAFE module serves two detector stations. Each anode signal is connected to the input of a discriminator. If a signal transcends a detector specific threshold, a logic signal is produced by the discriminator. The discriminator signals are combined via a logical OR for the e/γ- and μ-detectors of a station, respectively. In the case of an event, the overall logic signal triggers a TDC, which measures the time from the threshold transition to the next following 5 MHz clock signal. This time measurement plays a crucial role in the scope of this analysis. It allows to determine the arrival time of the detector signals at the DAQ electronics with a precision of less than a nanosecond. It is vital to synchronize the KASCADE array with the Grande array, as described in chapter 6. The discriminator thresholds are adjustable and are different for the e/γ-detector and the μ-detector. They have to be set low enough to be sensitive for the detection of a single minimum ionizing particle (MIP). The threshold for the e/γ-detectors is adjusted to 2/5 of the average energy deposition of a single MIP (≈ 4.5 MeV). The threshold for the μ-detectors corresponds to 1/3 of the average energy deposition of a single MIP (≈ 2.6 MeV) [Sch96]. These values are later used to determine the exact time of the threshold transition in the pulse shapes recorded by the FADC modules (chapter 8).

The second task of the KAFE modules is to measure the total energy deposit in the e/γ- or μ-detector of the connected stations. Therefore, the KAFE modules sum up the anode

signals of the e/γ- or μ-PMTs, respectively. The charge of each sum signal is integrated over 200 ns and digitized by an ADC (Analog to Digital Converter). The result is converted into the total energy deposit in the corresponding detector by using an energy calibration. In addition, the anode sum signal of each detector type is made available at the front panel of the KAFE module. In this way, other components can process the anode signals as well. In cluster 1 the KASCADE FADC system is connected to these outputs, as described in chapter 4. A detailed description of the hardware and the data acquisition of the KASCADE array is given in [Sch96].

3.2   The Grande array

The second major part of the KASCADE-Grande experiment is the Grande array. It consists of 37 scintillator stations, distributed over an area of $700 \times 700 \, \text{m}^2$ at the Forschungszentrum Karlsruhe. The Grande array is intended to increase the sensitive detection area. It allows to measure showers initiated by primary cosmic particles with an energy of up to 10^{18} eV. Besides, the larger coverage increases the statistics of air showers at the upper energy limit of KASCADE at about 10^{17} eV.

A sketch of the scintillator setup inside each of the Grande detector stations is shown in figure 3.5. It is a combination of sixteen $80 \times 80 \times 4 \, \text{cm}^3$ plastic scintillator[6] modules arranged in a 4×4 matrix. The total surface covered amounts to $10 \, \text{m}^2$. The modules
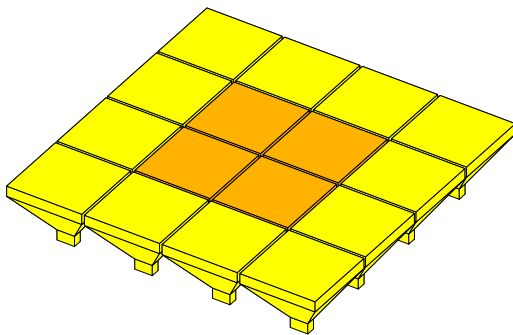
Figure 3.5: The scintillator detector of a Grande detector station [Ove04]. All 16 detector modules are equipped with high gain photomultiplier tubes. The inner four modules are in addition connected to low gain photomultipliers to measure high particle densities.

are located in a pyramidal metal case to protect the modules from external light. In order to detect the scintillation light, a photomultiplier[7] is mounted at the tip of each of the 16 pyramids. It is operated in high gain mode at a voltage of (1800-2050) V. An analog signal mixer is used to generate the overall high gain signal. To avoid saturation of the detector in case of high particle densities, the inner four pyramids are in addition equipped with a second photomultiplier of the same type, which is operated in low gain mode at a lower voltage of (1200-1600) V. They provide signals which are smaller by a factor of 10 than the corresponding high gain signals. These four low gain photomultiplier signals are as well added by an analog signal mixer to provide an overall low gain signal. One output of the high gain mixer module is connected to a discriminator which

---

[6]type NE102A
[7]type XP3462

generates a logic signal if the high gain signal exceeds a threshold, which is low enough to be sensitive for a typical signal of a single MIP passing the detector. The signal from these discriminator will in the following be referred to as logic run signal. It is sent to the central DAQ station of the Grande array for further processing by the coincidence logic. The overall high and low gain signals are both integrated over $8\,\mu$s by a shaping amplifier resulting in pulses which are proportional to the accumulated charges and thus to the deposited energy. The shaper module transmits these signals via 700 m coaxial cable to the DAQ station. A peak sensing ADC in the DAQ station digitizes the pulse heights which are proportional to the energy deposit in the scintillators.

Figure 3.6 shows the location of the Grande detector stations at the site of the Forschungszen-
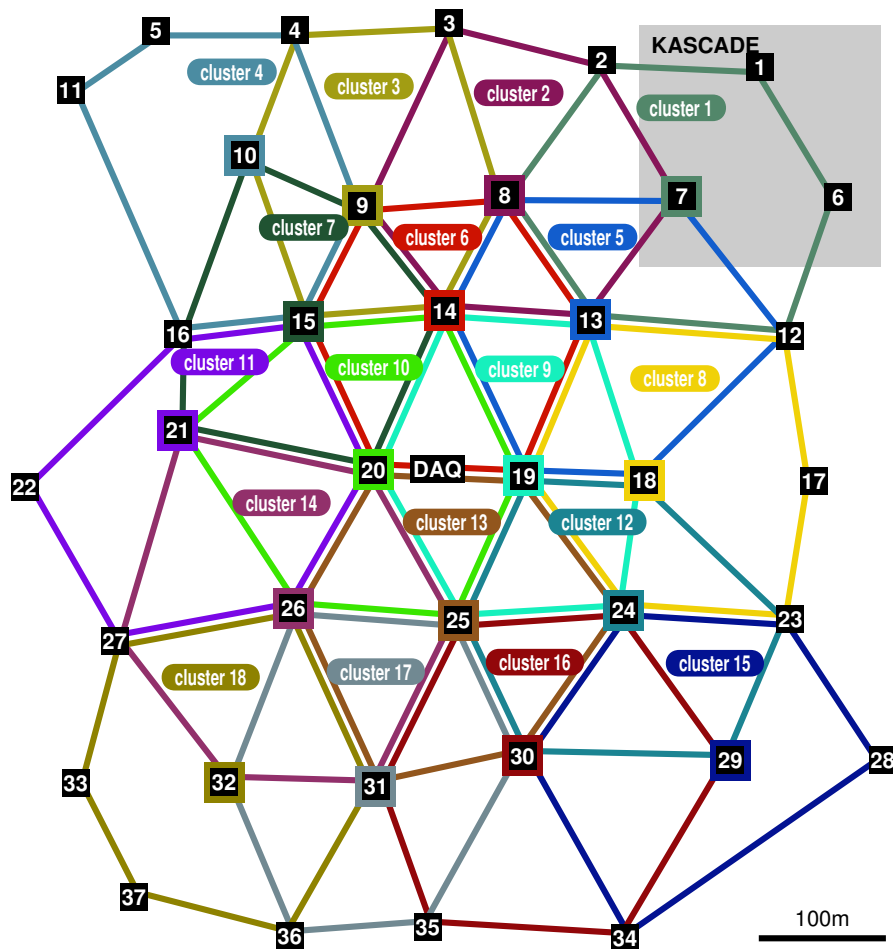
Figure 3.6: The locations of the Grande detector stations and the arrangement of trigger clusters [Ove04].

trum Karlsruhe. The DAQ station of the Grande array is located at the center of the Grande array with a distance to the central detector building of KASCADE of approximately 500 m. The data acquisition system of the Grande array is described in detail in [Ove04]. The trigger logic implemented in hardware divides the array into 18 overlapping trigger hexagons, also referred to as clusters. Each cluster contains seven stations, except cluster 15 which contains only 6 stations. Two trigger conditions are

implemented. First, the four-out-of-seven (4/7) trigger requires at least one cluster in coincidence with the logic run signals from the corresponding central station and three surrounding stations. The second trigger condition is called seven-out-of-seven (7/7) coincidence. It demands that at least one cluster measures coincident logic run signals from all of its stations. If one of the two trigger conditions is fulfilled, the real time clock module stores the current values of the 1 Hz and 5 MHz clock counters, which represent the event time of the Grande data.

Grande station 7 is of special interest for the time synchronization (see chapter 6) between the KASCADE experiment and the Grande array. It is the only Grande detector station which is located within the KASCADE array without being at the boundary of the Grande array.

3.3   The Piccolo array

The Piccolo array is an array of 8 scintillator stations distributed over an area of $360 \, \text{m}^2$ forming an octagon with 20 m distance between the stations. It was built to provide a fast trigger signal to assure a simultaneous measurement of air showers with the Grande array and the muon tracking and central detector of KASCADE. Each detector station contains 12 plastic scintillators providing a total sensitive area of $10 \, \text{m}^2$. Two scintillators together form one module. Therefore, the Piccolo array consists of 48 modules. A Piccolo trigger signal is produced and sent to KASCADE and Grande if a coincidence of at least four out of the 48 modules or two out of the eight Piccolo stations is detected.

The KASCADE Flash-ADC system

In order to analyze arrival time distributions of particles, the experiment has to offer the possibility to measure the arrival times of particles with high precision. The electronics of the e/γ- and μ-detectors of the KASCADE array is not able to provide the arrival time of each individual shower particle hitting the detector. The only time information measured using a TDC is the time of the discriminator threshold transition. To first approximation, this corresponds to the first particle within the particular segment of the shower disk that hits the detector. The time information of the following particles hitting the detector are lost since the electronics integrates the PMT signal to measure the energy deposit of the particles in the detector (see section 3.1.3).

As an alternative possibility to measure the arrival times of single particles in the shower disk an additional dedicated finely segmented detector equipped with fast electronics for time measurements as described in [Agn95] could be used. Another possibility is to record the full time development of the photomultiplier signals from which the arrival times can be extracted. This can be achieved by using a FADC based data acquisition system, which continuously samples the PMT pulses. This possibility is used by KASCADE. A Flash-ADC system is installed in 8 stations of cluster 1 of the KASCADE array. The analysis of particle arrival times described in this thesis is based on data from this KASCADE Flash-ADC system. In this chapter the hardware of the FADC system, the data acquisition and the processing of the measured pulses by the reconstruction software are described.

4.1   The electronics of the KASCADE FADC system

The KASCADE FADC system comprises in total 16 FADC modules. Each module contains four 250 MHz FADCs of 8 bit resolution operated in interleaved mode using a displacement of one nanosecond. Hence, each module reaches an effective sampling rate of 1 GHz. The four FADCs belong to four signal processing channels each comprising a buffer of 2048 words (1 word = 1 Byte). Therefore, the total buffer depth of one module amounts to 8 KByte. The modules are able to process signals in the negative voltage range from 0 V to -2 V.

The modules can be operated in two different data acquisition modes. The first mode is called autostop-on mode, in which the signal sampling by the FADC module is initiated by a start signal and is stopped automatically after 8 μs when the buffer is filled completely. Therefore, in order to measure event signals, the start signal has to be provided before the event actually happens. Air showers occur randomly, so the time between events is not fixed, i.e. this mode cannot be used to measure detector signals in air showers. The second mode is called autostop-off. In this mode, the modules acquire data continuously until they are stopped by a stop signal. In case the buffer size is exceeded before the stop signal occurs, writing starts again at the beginning of the buffer. This causes buffered data older than 8 μs to be overwritten, which corresponds to the operation of a ring buffer. The 8 KB depth of the buffer translates into a 8 μs long snapshot of the detector signal before the stop signal. This mode is used for the data taking with the KASCADE FADC modules. Therefore, the system relies on a properly adjusted delay of the stop signal which prevents buffered samples belonging to the event signal from being overwritten. The FADC system cannot generate a stop signal itself since no online processing of the measured signals is implemented which could trigger on interesting data. Hence, the FADC system relies on an external stop signal, which is provided by the trigger signal generated by the array electronics. The trigger signal is directly coupled to the occurrence of an air shower event and can be sufficiently delayed to record the detector signals in full length.

During summer, the temperature in the array detector stations can exceed the recommended temperature range of the electronics of the FADC system. Therefore, the modules have to be operated in an air conditioned environment, which is only available in the electronics stations of the array clusters. The VME standard of the FADC modules requires the use of a VME crate. For economical reasons, it was decided to install the FADC system only in one cluster of the KASCADE array so that only one VME crate is needed. Further, it was required to sample the signals of both detector types, the e/γ-detector and the μ-detector, respectively, which offers the important advantage to measure the structure of the muon disk independently from the electromagnetic shower disk. This restricted the installation of the FADC system to outer clusters only, and cluster 1 was finally chosen for the installation. The 16 FADC modules available are not sufficient to equip both detector types for all 16 stations of cluster 1. Therefore, it was decided to connect the FADC system to both detectors in 8 stations. The 8 detector stations were selected by the requirement that the coverage of the KASCADE FADC

system should not favor a certain arrival direction of air showers. The distribution of stations equipped with FADC modules within cluster 1 is shown in figure 4.1.

■ Array stations equipped with FADC modules
■ Array stations without FADC modules
■ Electronics station

Figure 4.1: Distribution of KASCADE array stations equipped with FADC modules in cluster 1. The numbering scheme of the stations within the cluster is also shown.

A schematic view of the electronics of the FADC system is shown in figure 4.2. The input signals to be digitized correspond to the analogue sum of the anode signals of the e/γ- or μ-detectors, respectively, which are provided at the front panels of the KAFE modules (see 3.1.3 on page 26). The signals are multiplexed to the FADC modules by linear-fan-in/fan-out modules, which at the same time also invert the signals. This is necessary because the FADC modules can only process signals of negative voltage. Before the signals reach the FADC modules, they are amplified by an amplifier module. The 16 amplified analogue PMT signals are then digitized continuously by the 16 modules. The linear-fan-in/fan-out modules and the amplifiers are modules in NIM standard.

The external trigger signal which is used as the stop signal for the FADC system as well as the clock signals are taken from the array modules in the electronics station. The trigger signal is provided as a TTL signal and has to be converted into a NIM signal for further usage. It reaches the FADC modules via a logical AND gate and can be blocked by an active veto signal at the second input of the AND gate. To pass the AND gate, the trigger signal has to be inverted at the input as it is provided active-low. This means that the signal represents a logic 1 if it is inactive and a logic 0 if it is active. The external trigger signal can originate from one of the array clusters, the trigger plane in the central detector, the Piccolo array or the Grande array. All trigger signals are first sent to the central trigger distributor and are then redistributed to all clusters. This leads to a total delay of $3\,\mu$s for trigger signals which are generated by one of the array clusters. After the AND gate, a NIM module delays the trigger signal by an additional $1\,\mu$s before the signal stops the digitization by the FADC modules. This delay is necessary as trigger signals generated by cluster 1 enter the electronics of the FADC system directly. Without this extra delay, these local trigger signals would cut off the digitization of the pulse

Figure 4.2: Schematic of the electronics of the KASCADE FADC system [Hor01].

shapes immediately at the point of the discriminator threshold transition and only the very beginning of the detector pulse would be sampled. The delay ensures that at least $1\,\mu$s of the detector pulse shape is sampled after a threshold transition occurred.

After the delay module, the trigger signal is multiplexed to the VME clock module and to the FADC modules. The first signal branch initiates in the VME clock module the storage of the current values of the 1 Hz and 5 MHz clock counters. The second branch stops the digitization of all FADC modules. When being stopped the FADC modules generate an EOC (End Of Conversion) signal. The EOC signal of the last module is used as the veto signal which blocks further trigger signals at the AND gate. The EOC signal of the penultimate module serves as veto signal for the VME clock module. This additional veto prevents that shortly following trigger signals, which were not blocked by the veto signal at the AND gate, trigger the clock module again.

Besides the FADC modules and the VME clock module, the VME crate also houses a PCI-VME interface serving as connection to a PC which runs a dedicated data acquisition software, whose main features are summarized below. For the communication with the data acquisition software the VME clock module generates a VME interrupt as soon as it receives a trigger signal. This VME interrupt initiates the readout of the VME clock module and the buffers of all FADC modules.

4.2 The KASCADE FADC data acquisition

The data acquisition software of the KASCADE FADC system is responsible for the readout of the buffers of the FADC modules. At readout it performs a suppression of samples which do not belong to a detector signal and creates a data packet according to the specifications of the event builder. A detailed description of the DAQ software is given in [Hor01].

Every time the VME clock module generates a VME interrupt, the DAQ software reads the content of the FADC buffers to the PC memory and restarts the FADC modules immediately afterwards. The FADC data in the PC memory is then processed in order to perform a zero suppression to reduce the amount of data to be transferred and stored permanently. This is achieved by looking for particle signals in the buffered FADC data. The beginning of a signal is defined as two adjacent samples above a threshold signal height

$$ch_{\text{threshold}} = \mu + n \times \sigma$$

in units of FADC channels. The threshold is determined at each run start from the data of the first 20 events. Herein μ denotes the mean value of all samples of the first 20 events, and σ the corresponding standard deviation. The value n is adjustable and was set to $n = 3$ for all runs analyzed. When a signal is found by the DAQ software it is stored together with an adjustable number of samples before and after. The number of samples before the signal and the number of samples after the signal to be stored were both set to 100. If no signal is found by the online software, the corresponding module does not appear in the data at all. The peak finding algorithm discards the first $2\,\mu$s of the buffered FADC data. When the FADC system was installed and commissioned, no subdetector was present which could generate a trigger signal which arrived so late that event signals occupied the first 2 KB of the FADC buffers.

## 4.3 Offline signal processing

The raw signals from the KASCADE FADC system are further processed by the offline reconstruction software KRETA. Several contributions from the FADC electronics, described below, have to be reduced before the signals are usable for analysis. Sample raw signals of both detector types are depicted in figure 4.3. The raw signals show a regular noise structure, which is caused by the different characteristics of the four interleaved FADCs per module. Intercalibration values for each FADC, which could be used to eliminate these differences, are not available. To smoothen the resulting deformation, the signal is processed with a median filter. The filter has a width of 3 samples. It replaces each measured sample i by the median of the 7 samples within the range of ± 3 samples around sample i. A special treatment of random noise, which contributes to the signal deformation as well, is unnecessary, since it is smoothened by the filter as well.

The pedestals of the PMT signals are adjusted in order to assure a full containment of the
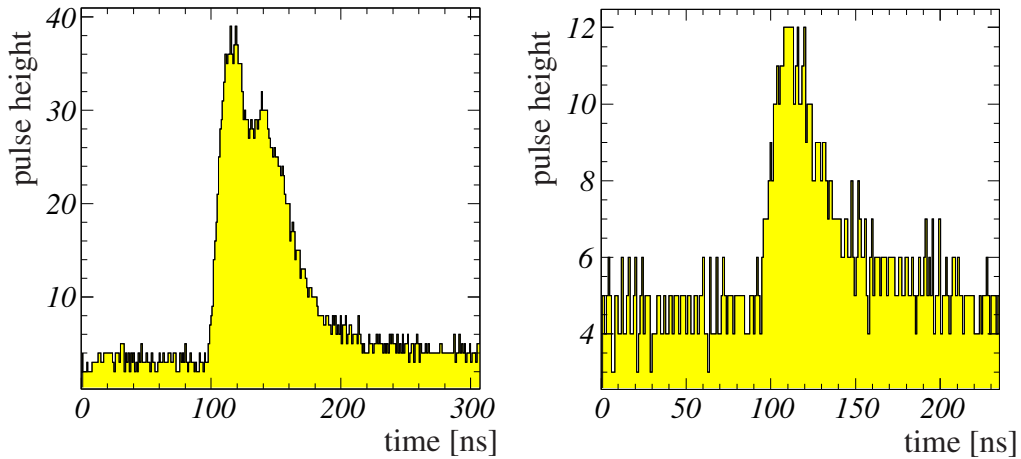
Figure 4.3: Examples of raw FADC signals (Run5130, event 89372). *Left:* Raw e/γ-detector signal measured by the FADC system. *Right:* Raw μ-detector signal measured by the FADC system.

signal within the measureable voltage range of the FADC system. The pedestal settings are different for each module and have to be subtracted on a signal-by-signal basis to be able to analyze the signals from different modules in an identical way. Hence, the reconstruction software performs a pedestal estimation for each signal using its first 80 samples. The mean value of these 80 samples is taken as pedestal and subtracted from all signal samples. Figure 4.4 shows as an example the signals depicted in figure 4.3 after
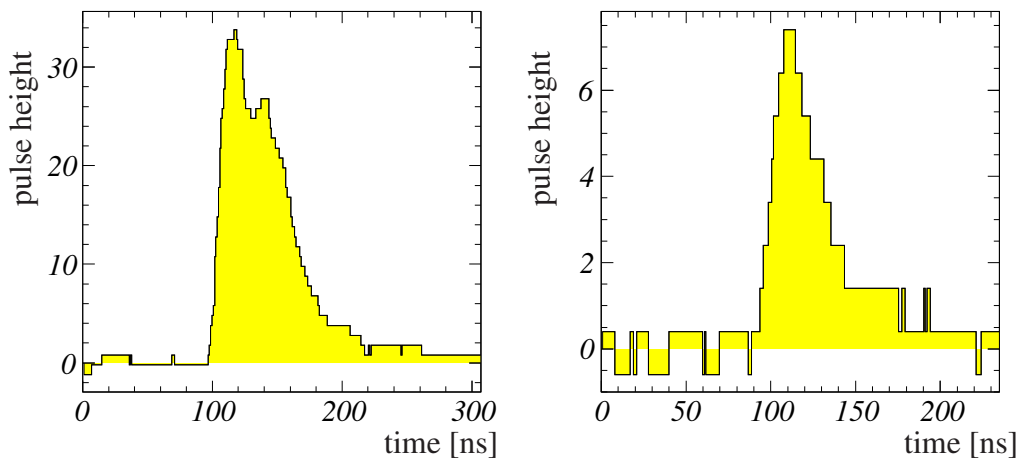
Figure 4.4: Examples of filtered FADC signals with subtracted pedestal (Run5130, event 89372). *Left:* Processed detector signal of the e/γ-detector. *Right:* Processed detector signal of the μ-detector.

the application of the filter and the pedestal correction. For the analysis presented in this thesis only the signals resulting from the signal processing described in this section are used.

Reconstruction and simulation of extensive air showers

For the reconstruction of air showers measured by KASCADE-Grande the reconstruction program KRETA (KASCADE REconstruction for exTensive Air showers) is used. The reconstruction steps are described in the first part of this chapter.

The second part of this chapter represents a brief description of the simulation procedure used for the KASCADE-Grande experiment.

5.1   Reconstruction of air showers

The first task of the reconstruction program KRETA is the transformation of the measured raw data provided by the detector electronics in terms of ADC and TDC values into energy deposits and time information. This transformation uses calibration spectra which have been gathered either in parallel to the measurement of air showers or separately by dedicated calibration measurements. The resulting values for the energy deposits and times are then used to reconstruct the air shower using a three-step iterative procedure. In the following these steps are referred to as levels. Showers, which did not trigger the Grande array, are considered KASCADE events and are reconstructed accordingly [Web99, Ant01, Mai03]. The reconstruction algorithms, which are used for events measured with the Grande array, are described here separately for each level.

Level 1

Level 1 uses robust methods to provide starting values for the shower observables, which
are successively improved in the higher levels. These shower observables include the
coordinates of the shower core, the arrival direction of the shower, the arrival time of
the shower core, and the number of electrons and muons.

The position of the shower core is determined by a center of gravity method, which
weights the detector coordinates with the corresponding measured energy deposits. The
shower arrival direction is estimated by one of two selectable methods. In the first
method, a plane is adjusted iteratively to the shower front arrival times measured by
the three Grande detector stations with the highest energy deposits. The second method
solves a linear system of equations. This system of linear equations arises from the
requirement that the sum of time differences between an average shower front, which
was determined from simulations, and the times measured by all detector stations is
minimal. The latter method relies on the coordinates of the shower core, since the time
profile of the average shower front depends on the distance from the shower core due to
the curvature of the shower front. If the estimation of the core position has failed, the
coordinates of the Grande detector station, which measured the highest energy deposit,
are taken instead.

For all further calculations, especially in level 2 and 3, a transformation into shower disk
coordinates (SDC) is performed. The new coordinate system is given by the shower axis,
which represents the new z^{SDC}-axis and the plane perpendicular to the shower axis, the
shower plane, which contains the new x^{SDC}- and y^{SDC}-axes. The transformation has two
effects. The first effect is, that in the new coordinate system the distances of the detector
stations to the shower core are shortened due to the projection of their coordinates onto
the shower plane. The second effect is that detector stations, although they are placed
at the same height in normal coordinates, receive a different z^{SDC}-coordinate in the
shower disk coordinate system due to their different radial distance from the shower
core in the $x - y$-plane. The transformation into shower disk coordinates and its effects
are illustrated in figure 5.1.
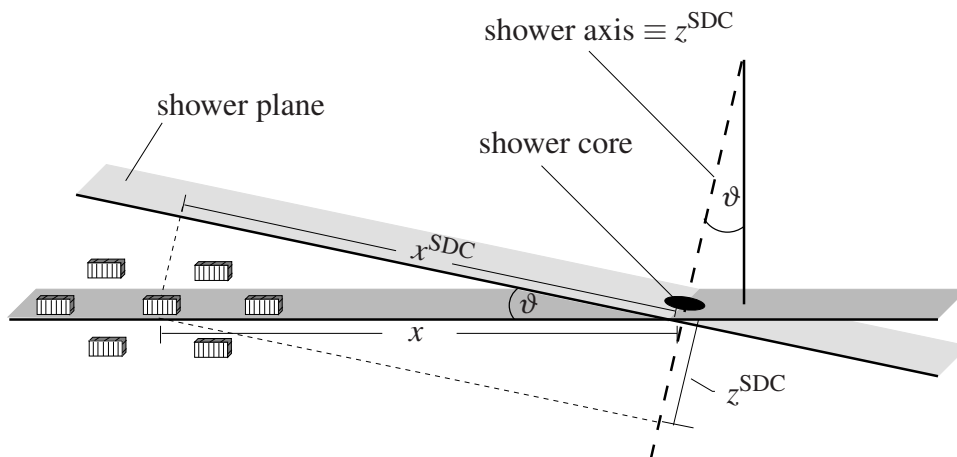
Figure 5.1:   Definition of the shower plane and the transformation into the shower disk coordi-
nate system.

In order to estimate the number of particles N_x of a specific particle type x contained in a measured air shower, also referred to as shower size, the corresponding lateral density distribution function

$$\rho_x(r) = N_x \times f_x(r)$$

is used. The value $\rho_x(r)$ represents the density of particles of type x at a distance r (in SDC) from the shower core. The function $f_x(r)$ is the lateral density distribution function for particles of type x in SDC normalized to 1. The formula is discretized to allow an estimation N_x^{est} of N_x using the data of the detector stations measured at discrete distances from the shower core. Translating the density $\rho_x(r)$ into the number of particles n_i^x of type x measured by a detector station i at distance r_i and summing over all M detector stations, the particle number N_x can be estimated with the detector data via the formula for

$$\sum_{i=1}^{M} n_i^x = \sum_{i=1}^{M} N_x^{\text{est}} \times f_x(r_i) \times A_i \times \cos \vartheta = N_x^{\text{est}} \times \sum_{i=1}^{M} f_x(r_i) \times A_i \times \cos \vartheta.$$

The parameter A_i represents the detector area seen by the shower particles. It is decreased by a factor $\cos \vartheta$ for inclined showers with ϑ being the zenith angle. Thus the number of particles of type x is estimated to

$$N_x^{\text{est}} = \frac{\sum_{i=1}^{M} n_i^x}{\sum_{i=1}^{M} f_x(r_i) \times A_i \times \cos \vartheta}. \tag{5.1}$$

For the estimation of the number of charged particles N_{ch} in level 1, the function

$$f_{\text{ch}}(r) = \frac{1}{2\pi \times C \times r_0^2} \times 10^{(p_1 x + p_2 x^2 + p_3 x^3)} \tag{5.2}$$

with fixed parameters $C = 4.8267$, $r_0 = 90\,\text{m}$, $p_1 = -2.462$, $p_2 = -0.4157$ and $p_3 = 0.09863$ is used. The parameters were determined by fitting the charged particle density distribution obtained from averaging 20 simulated proton and iron air showers with a fixed primary energy of $E_{\text{prim}} = 10^{17}\,\text{eV}$ and a zenith angle of $\vartheta = 22°$ [Gla05a]. According to equation 5.1, the numbers of charged particles n_i^{ch} actually measured by the Grande detector stations are used in the calculation of $N_{\text{ch}}^{\text{est}}$.

A first estimate of the muon number N_μ^{est} is obtained by using the number of muons n_i^μ measured by the muon detectors in the KASCADE array stations. The function

$$f_\mu(r) = \frac{0.28}{r_0^2} \left(\frac{r}{r_0}\right)^{p_1} \times \left(1 + \frac{r}{r_0}\right)^{p_2} \times \left(1 + \left(\frac{r}{10 \times r_0}\right)^2\right)^{p_3}$$

is used to describe the lateral density distribution function of muons. The scaling parameter r_0 amounts to $r_0 = 320\,\text{m}$ and the other parameters are $p_1 = -0.69$, $p_2 = -2.39$ and $p_3 = -1.0$. They were obtained by averaging the fit results of the lateral density distribution function to simulated $10^{16}\,\text{eV}$ and $10^{17}\,\text{eV}$ proton and iron air showers. A detailed description of the reconstruction of the muon number is given in [Bur06].

The first estimate of the number of electrons N_e^{est} is calculated using the number of electrons n_i^e measured by the e/γ-detectors in the KASCADE array stations. The function 5.2 is used to describe the lateral density distribution function of electrons.

Level 2

For the estimation of the electron number N_e in level 2, a slightly modified NKG-function (see also chapter 2)

$$f_e(r) = \frac{\Gamma(\beta - s)}{2\pi r_0^2 \Gamma(s - \alpha + 2)\Gamma(\alpha + \beta - 2s - 2)} \times \left(\frac{r}{r_0}\right)^{s-\alpha} \left(1 + \frac{r}{r_0}\right)^{s-\beta} \quad \text{[Ape06]}$$

serves as lateral density distribution function of the electrons. The parameters are $\alpha = 1.5$, $\beta = 3.6$ and $r_0 = 40$ m. They were determined using air showers simulated with CORSIKA [Gla05b]. The parameter s represents the shower age and is determined by the reconstruction. For the determination of N_e^{est}, the number of electrons n_i^e measured by the Grande detector stations has to be known. Since the Grande stations measure only charged particles, n_i^e is calculated by subtracting the estimated number of muons in Grande station i from the number of measured charged particles. The number of muons in the Grande stations is estimated by using the lateral density distribution function of muons from level 1 and the result for N_μ^{est} from level 1.

In order to improve the values for the shower arrival direction and core position, a parameterization of an average shower front, extracted from averaged simulated air showers, is fitted to the arrival times of the shower front measured by each Grande detector station. The parameterization of the average shower front is given by

$$\bar{t}(r) = 2.43 \, \text{ns} \times \left(1 + \frac{r}{30 \, \text{m}}\right)^{1.55} \qquad \text{and} \qquad \sigma_t(r) = 1.43 \, \text{ns} \times \left(\frac{r}{30 \, \text{m}}\right)^{1.39}$$

with $\bar{t}(r)$ being the average arrival time of particles at distance r from the shower core and $\sigma_t(r)$ the corresponding time spread. The arrival time of the shower front at distance r is determined by the time of arrival of the first out of N particles given by $\bar{t}_{1.\text{ of } N}(r) = \bar{t}(r)/\sqrt{N}$ [Gla05b].

The parameterizations of the average shower front and the lateral density distribution of electrons are linked by the core distance r. Therefore, they are fitted simultaneously to the data in a combined negative-log-likelihood minimization [Gla05b]. The minimization algorithm varies seven free parameters in order to fit the measured data. These are the core position coordinates, the shower direction, the electron number, the shower age s and, most important for this analysis, the arrival time of the center of the average shower front to fit the measured detector times as sketched in figure 5.2 This arrival time represents the arrival time of the shower core as well as the arrival time of the shower plane. It will be referred to as $t_{\text{core}}^{\text{Grande}}$ in the following. The times of the Grande detector stations correspond to TDC values multiplied with the TDC resolution in nanoseconds. Since the parameterized average shower front is fitted to these times, the shower core arrival time $t_{\text{core}}^{\text{Grande}}$ is given in the same units. Therefore, it represents the TDC value provided by a virtual Grande detector station located exactly at the position of the shower core.
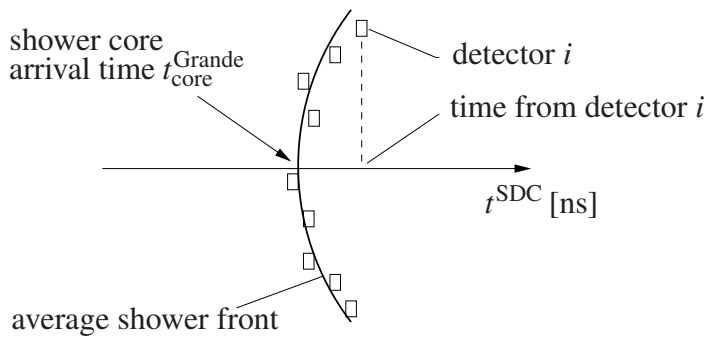
Figure 5.2: Scheme of the reconstruction of the shower core arrival time by fitting an average shower front to the measured detector times. The time axis is given in shower disk coordinates (SDC).

With the improved values for the position of the shower core and the shower direction, an improved number of muons is calculated analog to the procedure explained in level 1.

Level 3
The reconstruction procedure at level 3 repeats the algorithms at level 2 with improved starting values for the shower core position, the shower arrival direction and the muon number. The results of level 3 for the shower core position and the shower arrival direction are then used to calculate a further improved and final muon number. The results of reconstruction level 3 are the final observables from the reconstruction. They are used for all analyses of the KASCADE-Grande data.

5.2 Simulation of extensive air showers for KASCADE-Grande

In later chapters, simulated data are used to study the reconstruction accuracy of the shower core arrival time and to motivate cut criteria, which are used to exclude certain air showers from the analysis. The simulation of extensive air showers for the KASCADE-Grande experiment is performed with the simulation code CORSIKA (COsmic Ray Simulation for KASCADE) [Hec98]. It is a comprehensive Monte Carlo program which was originally developed for the KASCADE experiment. It describes the development of extensive air showers in the atmosphere by simulating the interactions and decays of nuclei, hadrons, muons, electrons and photons. All decay channels with a branching ratio above 1 % are taken into account. The program allows to choose the type of primary particle which initiates the air shower, its energy and its arrival direction. The hadronic interactions are described by different hadronic interaction models. The choice of the interaction models used to describe the hadronic interaction depends on the energy $E_{\mathrm{lab}}^n = E_{\mathrm{lab}}/$Nucleon. The transition from one model to the other is controlled by an adjustable threshold for this energy. Electromagnetic processes are described by the program EGS4 (Electron Gamma Sower code version 4) [Nel85].

Unless otherwise noted, the simulations used in the following consist of three sets of air showers simulated with CORSIKA 6.152 in the energy range from 10^{14} eV to 10^{18} eV according to a power law energy spectrum with a spectral index of $\gamma = 2.0$. The zenith

angles of the simulated air showers are in the range $0°$ to $42°$. For all three sets the inter-action model QGSJET I [Kal93] was used to describe high energy hadronic interactions. The model Fluka 2002.4 was used [Fas03, Fer05] to describe the hadronic interactions at low energies. The energy threshold for the transition from Fluka to QGSJET was set to $200\,\mathrm{GeV}$. Each of the data sets contains approximately 64,000 simulated air showers for each of the five simulated primary particle types: hydrogen, helium, carbon, silicon and iron.

Each simulated air shower is passed through the detector simulation CRES (Cosmic Ray Event Simulation). Its task is to provide simulated detector responses in a format identical to the detector data obtained in the real experiment. This allows for an identical processing of simulated air showers by the reconstruction program KRETA as it is used for measured air showers. The simulation of high energy extensive air showers is very time consuming and only a limited number of events can be simulated in a reasonable time. Therefore, in order to increase the statistics, each simulated air shower is passed several times through the detector simulation. For each individual pass, the shower core position of the simulated air shower is chosen uniformly random in an area of $760 \times 800\,\mathrm{m}^2$ to assure a different response of the detectors. The showers of one of the three simulated data sets passed the detector simulation 5 times. The showers of the other two simulated data sets were processed 10 times by the detector simulation.

Synchronization of the KASCADE and the Grande array

The analysis presented in this thesis aims at analyzing particle arrival time distributions especially for greater distances from the shower axis. The KASCADE FADC system, which is used to generate these arrival time distributions, is installed in cluster 1 of the KASCADE array. Showers with a significantly far core position can only be provided by the Grande array. Therefore, the showers measured by the Grande array are of special interest. These showers require a coincident measurement of the KASCADE and the Grande array. Both detector arrays can be thought of as two separate experiments running in parallel. A joint analysis of arrival times, using the data of both arrays, requires their time synchronization. In this chapter the determination of the time offset is described in detail.

6.1   Origin of the time mismatch

The time mismatch between the KASCADE array and the Grande array is caused by the different experimental setup. As will be explained below, the main contributions are the time delay introduced by the signal running times between both arrays and the different cable lengths from the detectors to the data acquisition electronics. Hardware effects like different response times of the different detector and acquisition electronics contribute to the time mismatch as well, but the contributions from the cable lengths dominate by far.

In figure 6.1 the time measurement of a shower event in shower disk coordinates, separated into the two arrays – left hand side KASCADE array, right hand side Grande

array –, is sketched to illustrate the sources of the time offset. The abscissa represents the distance from the shower center and the ordinate describes the time increasing downwards. Tick marks on the outer left and outer right margins represent clock cycles of the 5 MHz clock provided by the central clock distributor in the central detector building of KASCADE. Each clock signal increments the 5 MHz clock counter in the real time clock module, which is a part of the data acquisition (DAQ) electronics of Grande [Ove04]. The counter values for the 5 MHz clock are in the following referred to as Time Label (TL). They serve as time stamps for the overall KASCADE array and Grande array data, respectively. The true arrival time of the air shower is depicted by the shower plane indicated by the dashed horizontal line ①. It is defined as the plane perpendicular to the shower axis through the shower core. Therefore, the arrival times of the shower plane and the shower core are equal. The shower core is depicted in figure 6.1 as a virtual station at $R = 0$.

The Grande array (right hand side) measures the shower front approximately Δt_{Grande} later (dashed line ②). This delay is caused by the 700 m long cables connecting the Grande stations with the Grande data acquisition station. With an estimated signal velocity of 4 ns/m [Sch05] the delay amounts to $\Delta t_{\text{Grande}} \approx 2.8\,\mu$s or about 14 clock cycles. This delay is reduced by the displacement between the clock counter values of the KASCADE experiment and the Grande array. During the run start procedure a reset signal sets all clock counters back to zero. It is provided by the DAQ hardware housed in the central building of KASCADE and arrives with a delay Δt_{Clock} at the Grande DAQ electronics. The clock counter values of Grande are therefore smaller, since counting from zero starts Δt_{Clock} later. The estimated distance of the Grande DAQ station from the central detector building of KASCADE is 500 m. Therefore, a time displacement $\Delta t_{\text{Clock}} \approx 2.5\,\mu$s or about 12 clock cycles is expected, if a signal transfer speed of 5 ns/m is assumed. The combination of both delays results in an effective delay $\Delta t_{\text{Grande}}^{\text{eff}}$ of about 2 clock cycles between the true shower arrival time (①) and the one measured by the Grande array (dashed line ③).

In case of the KASCADE array (left hand side), a shower which hits the observation level at time ① will be registered with a delay Δt_{Array} by the discriminators in terms of threshold transitions (dashed line ④). This delay corresponds to the time the signals need to cross the distance from the detectors to the cluster electronics. For a cable length of approximately 40 m and a signal velocity of 5 ns/m [Sch05] this delay amounts to $\Delta t_{\text{Array}} \approx 200$ ns. For the reconstruction of air shower observables, the arrival time differences of the shower front between the KASCADE stations have to be known with high precision. Hence, a TDC measures for each detector i the time $\Delta_{\text{Discrim.}}^{i}$ between the discriminator signal and the following 5 MHz clock signal ($\text{TL}_{\text{reference}}$) with a precision of 0.7 ns (see also section 3.1.3). The times of the discriminator signals are however not referred to $\text{TL}_{\text{reference}}$ but to $\text{TL}_{\text{KASCADE}}$. The latter is determined by the arrival time of a trigger signal provided by the central trigger distributor and becomes the time stamp of the KASCADE array data. The stored time information t_{detector}^{i} from a single KASCADE station i is thus the sum of the TDC measurement $\Delta_{\text{Discrim.}}^{i}$ and the time difference $(\text{TL}_{\text{KASCADE}} - \text{TL}_{\text{reference}}) = n \times 200$ ns. It describes the arrival time of the detector signal from detector i in the cluster electronics relative to $\text{TL}_{\text{KASCADE}}$, marking
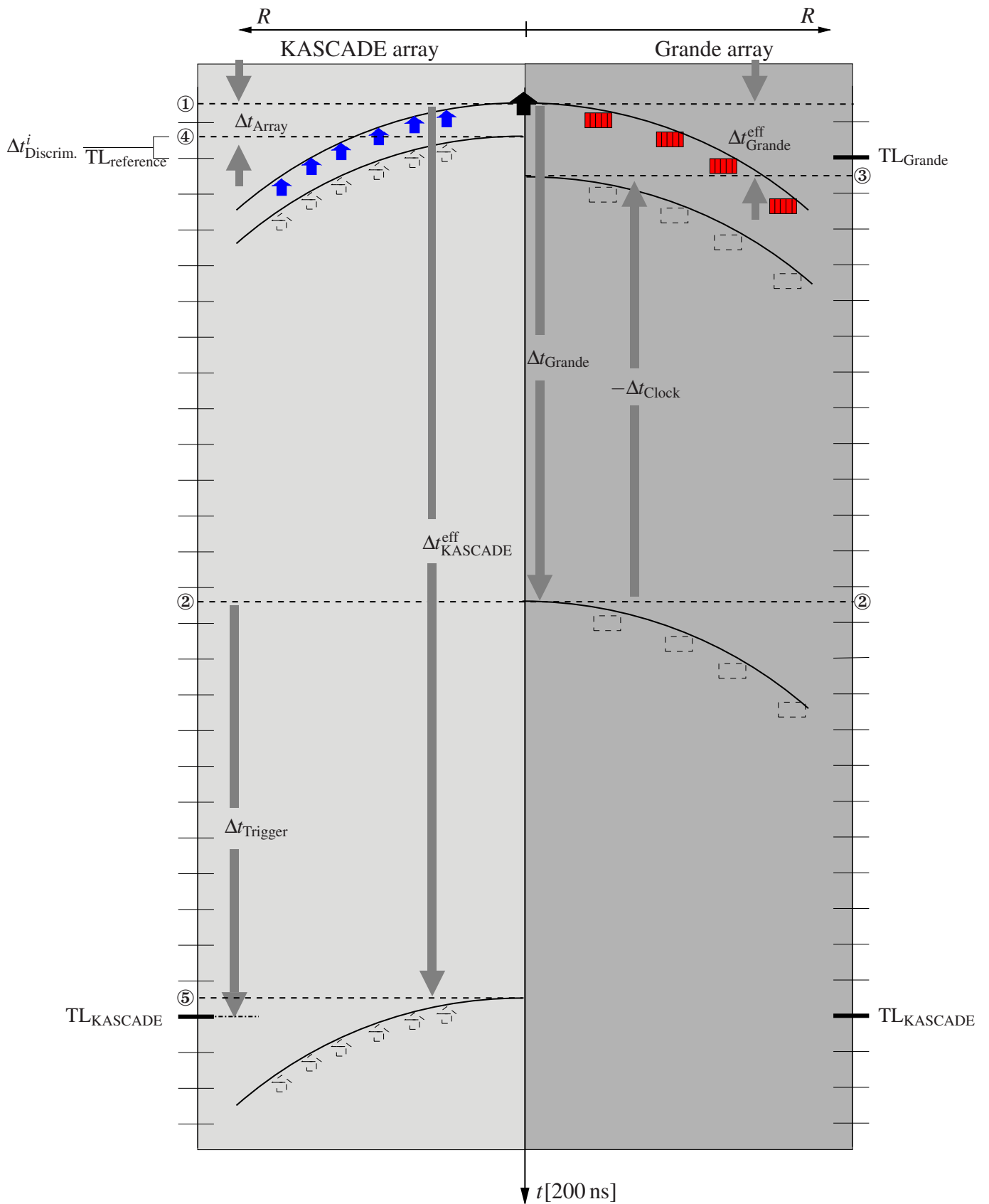
Figure 6.1: Contributions to the time offset between the KASCADE and the Grande array. See text for details.

the arrival time of the common trigger signal in KASCADE. As shown in the picture, a trigger signal, which is produced by Grande at ②, needs an additional running time $\Delta t_{\text{Trigger}}$ to arrive in the KASCADE DAQ hardware. In total this leads to an effective time delay $\Delta t_{\text{KASCADE}}^{\text{eff}}$ for the shower plane measured by the KASCADE array (dashed line ⑤).

The time offset between the KASCADE experiment and the Grande array is therefore given by the difference between the effective arrival times of the shower planes measured by the KASCADE array $\Delta t_{\text{KASCADE}}^{\text{eff}}$ (dashed line ⑤) and the Grande array $\Delta t_{\text{Grande}}^{\text{eff}}$ (dashed line ③).

6.2 Determination of the time offset

As explained above, the shower plane or shower core arrival time measured by the Grande array has to be subtracted from the arrival time measured by the KASCADE array to find the synchronization offset for both arrays.

For exactly vertical showers with a completely flat shower disk hitting all stations simultaneously, the measured times of all stations could be used to calculate the arrival time of the shower plane. Real showers neither have a flat shower disk nor are exactly vertical. In figure 6.1 an exaggerated curvature of the shower front illustrates the effect on the measured detector times. Detectors far from the shower center measure later arrival times, which do not represent the arrival time of the shower core. Therefore only stations close to the shower core, where the curvature of the shower front is still negligible, are able to provide time measurements corresponding to the arrival time of the core.

The detector time of a specific KASCADE detector station k which is located exactly at the position of the shower core is given by $t_{\text{detector}}^k = (\Delta t_{\text{KASCADE}}^{\text{eff}} + \Delta t_{\text{Discrim.}} - \Delta t_{\text{Array}})$. With this time, the true arrival time t_0^{KASCADE} of the shower plane (①) can be calculated to

$$t_0^{\text{KASCADE}} = \text{TL}_{\text{KASCADE}} - t_{\text{Detector}}^k - \Delta t_{\text{Array}}.$$

To calculate the corresponding value t_0^{Grande} from Grande data, a time measurement from a Grande station close to the shower center is needed as well. If Grande station l would be the station closest to the core, the true arrival time t_0^{Grande} of the shower plane is

$$t_0^{\text{Grande}} = \text{TL}_{\text{Grande}} + \Delta t_{\text{TL}}^l + \Delta t_{\text{Clock}} - \Delta t_{\text{Grande}}.$$

The parameter Δt_{TL}^l represents the time difference between the time stamp $\text{TL}_{\text{Grande}}$ of the Grande data and the arrival time of the discriminator signal from Grande station l in the Grande electronics (③).

To calculate both parameters on a shower-to-shower basis, detector stations of both arrays have to be located close to the shower core. Therefore, only Grande station 7

remains to provide the data from Grande needed to determine the offset. This is due to the following two reasons. Firstly, it is located within the KASCADE array and thus being surrounded by four KASCADE detector stations close by. Secondly, from all three Grande stations within the KASCADE array it is the only one which is located sufficiently far away from the boundaries of the Grande array, where the reconstruction of the shower core becomes erroneous [Gla05a, Bur06].

The data sample, that was used to determine the offset, consisted of all showers that triggered a 7/7 coincidence in the Grande array with the maximum energy deposit in Grande station 7. All runs between Run 5240 and Run 5464 with both arrays taking data in coincidence were included. To increase the statistics of showers used for the offset determination, also inclined showers were included. Showers with zenith angles $\vartheta > 60°$ were discarded to avoid misreconstructed showers [Gla05a]. Grande station 7 is located within cluster 5 of the KASCADE array. Its neighboring KASCADE stations are stations 5, 6, 7 and 8 with a distance of 7.7 m (stations 5,6) and 11 m (stations 7,8). In case of inclined showers this distance results in an arrival time difference of $\Delta t = d/c \times \sin\vartheta$ caused by the path length difference $d \times \sin\vartheta$ for the shower plane between two stations. Herein d is the distance between two stations, c the speed of light and ϑ the zenith angle of the air shower. In order to avoid this contribution, a mean arrival time was calculated from all time measurements of the four neighboring KASCADE detectors on a shower-by-shower basis. This mean detector time was then used to estimate the true arrival time of the shower plane t_0^{KASCADE} to be compared to the corresponding t_0^{Grande} calculated from the time measured by Grande station 7. Nevertheless, effects from contributions from path length differences in inclined showers cannot be fully prevented, since not always all four KASCADE stations are hit and provide time information. Hence, instead of always calculating the same offset values for all showers, a distribution of offset values is expected, centered at the true offset value. The spread is caused by the path length differences in inclined showers. The time offset has therefore to be extracted from the resulting distribution. Furthermore, to cut away small air showers, for which the curvature of the shower front cannot be neglected even close to the shower center, a minimum of 20 triggered Grande stations was required.

To summarize, the offset is determined by

$$
\begin{aligned}
\Delta t_{\text{KG}} &= t_0^{\text{KASCADE}} - t_0^{\text{Grande}} & (6.1) \\
&= \left(\text{TL}_{\text{KASCADE}} - <t_{\text{Detector}}> - \Delta t_{\text{Array}} \right) & (6.2) \\
&\quad - \left(\text{TL}_{\text{Grande}} + \Delta t_{\text{TL}}^7 + \Delta t_{\text{Clock}} - \Delta t_{\text{Grande}} \right)
\end{aligned}
$$

with $<t_{\text{Detector}}>$ being the average detector time from all triggered KASCADE stations next to Grande station 7. The parameter Δt_{TL}^7 is the time difference in nanoseconds between the arrival time of the 5 MHz clock signal corresponding to the TL of the Grande data ($\text{TL}_{\text{Grande}}$) and the arrival time of the discriminator signal (③) from the Grande station closest to the shower core, i.e. Grande station 7 for the selected showers. The parameters $\text{TL}_{\text{KASCADE}}, <t_{\text{Detector}}>, \text{TL}_{\text{Grande}}$ and Δt_{TL}^7 represent measured parameters. To verify the picture of the origin of the offset described in section 6.1, the values $\Delta t_{\text{Array}} \approx 40\,\text{m} \times 5\,\text{ns/m}$ and $\Delta t_{\text{Grande}} \approx 700\,\text{m} \times 4\,\text{ns/m}$ have been taken into account

as constant values. They were calculated from the estimated cable lengths and signal velocities. The only parameter that remains unknown is Δt_{Clock}. This means that the determination of the time offset between the KASCADE and the Grande array according to equation 6.1 is reduced to the determination of the transfer time Δt_{Clock} of the reset signal from the KASCADE hardware to the Grande hardware.

As equation 6.1 indicates, the determination of the time differences Δt_{TL}^i between the 5 MHz clock and the arrival times of the Grande discriminator signals is vital for the synchronization. While the time of the discriminator signals have been measured by a TDC since the beginning of the data taking with the Grande array, the time of the 5 MHz clock cycle belonging to the TL marking the Grande data (TL$_{\text{Grande}}$) was never needed for the reconstruction of the air shower observables and thus was missing. The measurement of the arrival time of the 5 MHz clock signal in the DAQ electronics of Grande had to be introduced into the hardware setup especially for this analysis. This is described in the next section.

6.3 Measurement of the Grande Time Label

For the reconstruction of the shower arrival direction and the position of the shower core two measurements are necessary. These are the relative arrival times of the shower front in the detector stations as well as the particle densities, i.e. the energy deposits in the detectors. Since only time differences between the detector times have to be known, TDC measurements of the arrival times of the logic run signals from the Grande discriminators were sufficient for the shower reconstruction in the past. The delay of these detector times with respect to the 5 MHz clock signal was never measured. Therefore, the global time information of single detector events was not available. This time difference is however mandatory for the analysis of particle arrival times relative to the shower plane using the time measurements of both arrays. Hence, in order to connect the time information from the Grande stations to the time reference system of the rest of the experiment, also the 5 MHz clock signal was measured by the TDC. Using this additional information, the time difference Δt_{TL}^i of each detector signal to the 5 MHz clock is known to a precision of less than 1 ns, and thus also the global time of the single station events as needed for the determination of the offset given by equation 6.1.

The hardware measuring the timing information of the Grande array is sketched in figure 6.2. The logic run signals from the discriminators of each Grande detector station are connected to the TDC. This multi-hit TDC stores the arrival times of one or more logic run signals in a 10 μs wide time window per input channel. It has a time resolution of 800 ps. The logic run signals are in addition processed by the coincidence logic, which checks the incoming signals for valid trigger conditions. If a coincidence is found, an EVENT signal is produced, which is sent to the real time clock module and to the KASCADE central detector building to trigger the other subdetectors of KASCADE-Grande. The real time clock module stores the values of the 1 Hz and 5 MHz clock counters, which will become the time stamp of the overall Grande event data. The
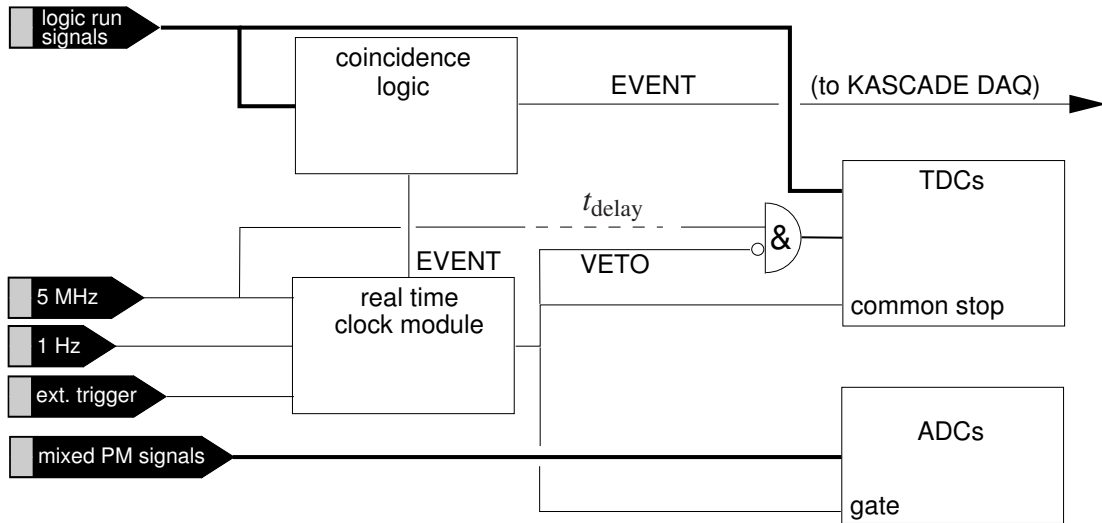
Figure 6.2: Simplified scheme of the Grande data acquisition hardware with the additional TDC measurement of the Time Label (TL$_{\text{Grande}}$). The dashed line indicates the 15 ns delay cable, which was introduced to study the reason for the occurence of the second offset distribution (see text).

5 MHz clock counter value assigned to the overall Grande data is referred to as TL$_{\text{Grande}}$.

In order to obtain a TDC measurement of the specific 5 MHz clock cycle corresponding to TL$_{\text{Grande}}$, an additional TDC channel was reserved for the 5 MHz clock signal. Due to its 10 μs wide time window, the TDC can store the time of up to 20 cycles of the 5 MHz clock. Hence, one task of the Grande DAQ software is to find the specific TDC measurement belonging to the clock signal which corresponds to the time label TL$_{\text{Grande}}$ assigned to the Grande event data. To ease the determination, a veto signal has been introduced to prevent that, in case of a Grande event, further 5 MHz clock cycles are measured by the TDC. The EVENT signal itself is used as VETO signal. It is fed to the inverted input of an AND gate to which also the 5 MHz clock line is connected to. This logic AND prevents the 5 MHz clock signals from entering the TDC in case of an active EVENT signal. The last entry found in the corresponding TDC channel $t_{\text{TDC}}^{\text{TL}}$ corresponds to the 5 MHz clock cycle belonging to TL$_{\text{Grande}}$. This measurement has been introduced with Run 5240 being started on 2005-01-31.

The resulting distributions of the offsets between the Grande array and the electromagnetic or muon detector of the KASCADE array, i.e. for the only unknown parameter Δt_{Clock} in equation 6.1, are shown in figure 6.3. Contrary to the expectation, two offset distributions instead of a single distribution per detector type are observed. The separation of the distributions amounts to exactly 200 ns, which suggests that this splitting is related to the 5 MHz clock. It was assumed that, in some occasions, the EVENT signal produced by the coincidence logic serving also as VETO signal for the TDC measurement of TL$_{\text{Grande}}$ ($t_{\text{TDC}}^{\text{TL}}$), arrives too early. This would cause the preceding 5 MHz clock cycle of TL$_{\text{Grande}}$ entering the TDC as last signal. In this case the DAQ software identi-
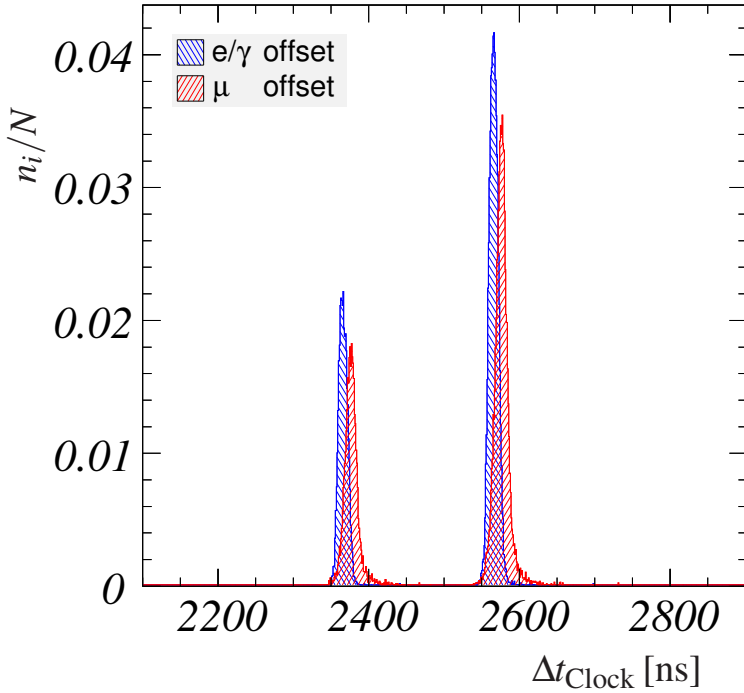
Figure 6.3: Distributions of the time offsets between the Grande and the electromagnetic and muon detector of the KASCADE array. Due to the experimental setup of the TDC measurement of TL_{Gramde} the calculation of the offset results in two distributions (see text). For comparison the bin contents n_i of the distributions were normalized by the total number of entries N.

fies the wrong last TDC entry as belonging to TL_{Grande} provided by the real time clock module for the Grande data. The missing 5 MHz clock cycle creates the distributions on the left hand side, because 200 ns are lacking in the offset calculation (eqn. 6.1).

To verify the above assumption, the hardware for the TDC measurement of the TL was modified by introducing an additional delay of $t_{delay} = 15$ ns (indicated by the dashed line in fig. 6.2) into the 5 MHz clock signal line to the TDC input. This increases the time window for the VETO signal to arrive too early at the TDC input. With this modification data was taken (Run 5509) to check the effect on the offset distributions. In picture 6.4 the offset distributions are shown with and without the additional delay. As expected from the above discussion, the extra delay of the 5 MHz clock shifts the offset distributions by 15 ns to the right. Furthermore, since the probability for a VETO signal arriving too early is increased, it is expected, that the population of the left hand side distribution grows at the costs of the right hand side distribution. These effects are observed in figure 6.4. The distributions were normalized to the number of entries to make them comparable. Additionally, to prove the effect quantitatively, the integrals of the left respectively right distributions with and without delay were calculated and compared to each other. In case of the offset distribution for the electron detector, the relative population of the left distribution increases from 35 % to 42 % whereas it is reduced by exactly the difference of 7 % from 65 % to 58 % in the right distribution. The same holds for the muon detector offset distributions.

There was no way to avoid the splitting of the offset values by additional changes to the hardware, because most of the data analyzed in this thesis was already taken. Hence, for each KASCADE array detector type, both offset values given by the two offset distributions have to be used in the data analysis.
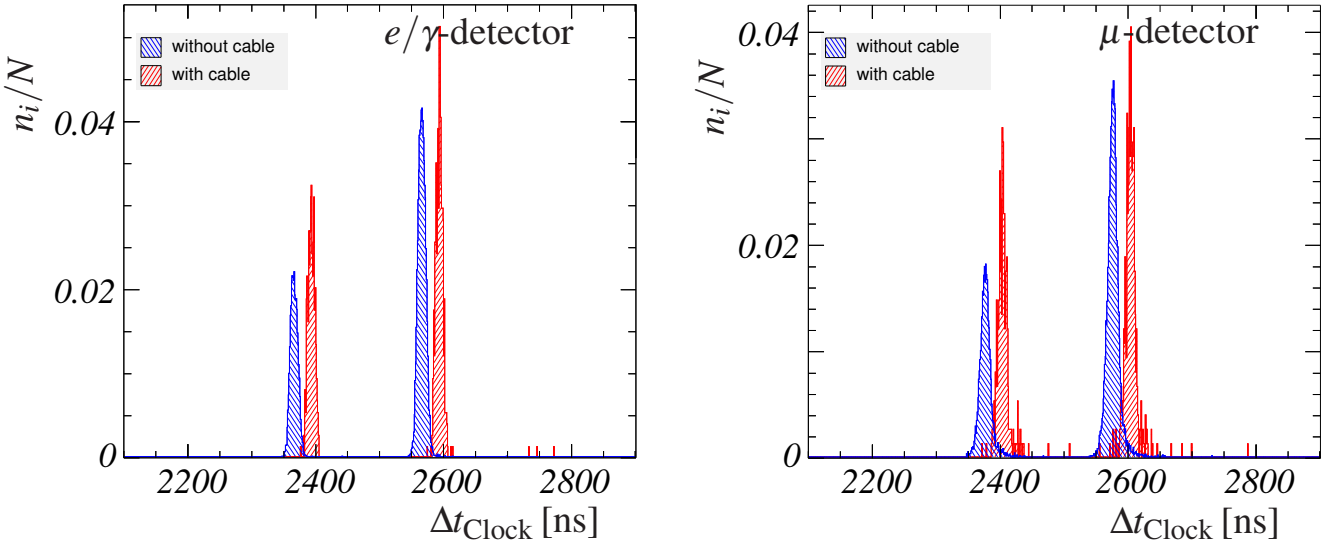
Figure 6.4: *Left:* Distributions of the time offset between the Grande array and the electron detector of the KASCADE array with and without the delay $t_{\text{Delay}} = 15\,\text{ns}$ in the 5 MHz signal line. *Right:* Same as left for the time offset between Grande and the muon detector of the KASCADE array. For comparison the bin contents n_i of the distributions were normalized to the total number of entries N of the corresponding distribution.

As explained earlier, the true offset values have to be extracted from the corresponding offset distributions. The true offset results from the combination of cable delays and can thus be regarded as an effective cable delay, i.e. a hardware parameter that does not change with time. The unavoidable simultaneous measurements of unaccompanied cosmic muons fill a small background contribution of uniformly distributed offset values invisible in figure 6.3. These background offset values represent outliers in the offset distributions. It was found that due to the sparse population of the uncorrelated background, the arithmetic mean from the distribution depends on the size of the interval of offset values used for the calculation. To avoid this bias, a Gaussian distribution was fitted to each offset distribution. The offset values are then given by the means of the Gaussians. The errors of the offset values are given by the errors of the corresponding fit values. As an example, in figure 6.5 the lower offset distribution for the electromagnetic detector of the KASCADE array is depicted together with the fitted Gaussian distribution and the fit results.

In this case, the offset amounts to $(2377.0 \pm 0.1)\,\text{ns}$. In appendix A all fits to offset distributions are shown. The four offset values extracted by this method are listed in table 6.1. Because equation 6.1 takes already the cable delays from the detectors to the DAQ electronics into account, the calculated offset represents the unknown running time Δt_{Clock} of the reset signal from the KASCADE to the Grande electronics, which was expected to be in the order of $\Delta t_{\text{Clock}} \approx 2.5\,\mu\text{s}$. The offset values extracted from the upper offset distributions are a measurement of the correct 5 MHz clock signal. Hence they correspond, apart from contributions from differences between the experimental setup of the KASCADE e/γ- and μ-detector, to the running time Δt_{Clock} of the reset
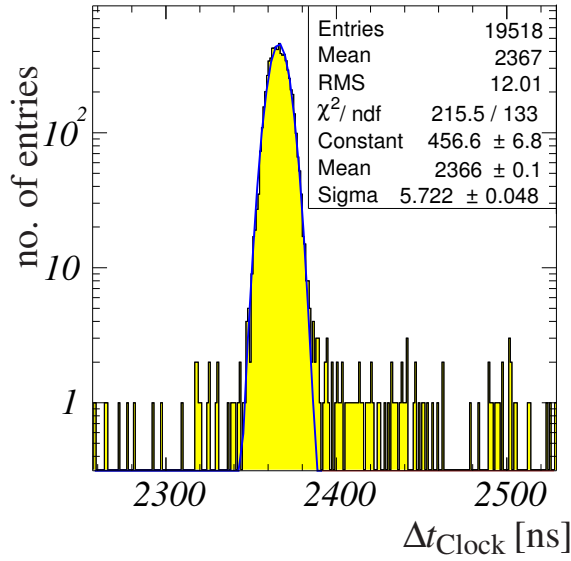
Figure 6.5: Lower distribution of offset values for the e/γ-detector fitted with a Gaussian to extract the offset value

KASCADE detector type	lower offset [ns]	upper offset [ns]
e/γ	2366.0 ± 0.1	2566.0 ± 0.1
μ	2376.0 ± 0.1	2576.0 ± 0.1

Table 6.1: Offset values between Grande and the KASCADE e/γ- and μ-detector extracted from a Gaussian fit to the corresponding offset distributions. The 10 ns difference between the offsets of the e/γ-detector and the μ-detector are caused by the difference in the hardware setup.

signal. These offset values agree well with the expected $2.5\,\mu$s.

A method to decide on an event-to-event basis if the upper or lower offset value has to be used to synchronize both arrays is described in the next section.

6.4 Assignment of the correct offset

As shown in figure 6.2, the 5 MHz signal reaches the real time clock module and the TDC input on different signal lines. The difference in length of these lines results in an additional delay of $\Delta t_{5\,\mathrm{MHz}}$ for the 5 MHz clock signal at the input of the TDC. If a certain 5 MHz signal arrives in the real time clock module, the relative time (phase) to the next incoming EVENT signal plus the constant running time of the VETO signal to the TDC will determine the total running time of the VETO signal to the TDC. If this time is smaller than the time delay $\Delta t_{5\,\mathrm{MHz}}$, the VETO signal will arrive too early and block the correct 5 MHz clock signal to be measured. The only variable contribution to the above mentioned signal delays is the phase between the generation of the EVENT signal and the preceding 5 MHz clock cycle. All other delays are fixed due to constant cable lengths. Therefore, the delay $\Delta t_{5\,\mathrm{MHz}}$ of the 5 MHz clock minus the time the VETO

signal needs to cross the cable from the real time clock module to the TDC represents a time window, i.e. maximum phase, for the phase between the EVENT signal and the 5 MHz clock. If this phase is smaller than the time window, the correct 5 MHz signal is blocked at the TDC input by the VETO signal. If the phase is larger, the correct 5 MHz clock signal reaches the TDC before the VETO signal blocks the input.

Besides, the EVENT signal is also used as common stop signal for the TDC. The online software adjusts the TDC to store the hits arriving in an interval of $\pm 5\,\mu$s around the arrival time of this stop signal. Since the stop signal and the VETO signal are identical, the last 5 MHz signal measured by the TDC can only occupy TDC values in a range of 200 ns before the arrival time of the stop signal. Additionally, this 200 ns interval is divided into two parts by the above mentioned time window for the phase between the EVENT signal and the 5 MHz clock. The wrong 5 MHz clock cycle will always be measured in a range of TDC values starting at -200 ns relative to the arrival time of the common stop signal with a width corresponding to the maximum phase. If the maximum phase is reached, the correct 5 MHz signal starts to arrive at the TDC input earlier than the VETO signal. The measurements of the correct 5 MHz signal are accordingly distributed over the remaining part of the 200 ns time window. The distribution of measured TDC values and the resulting separation of the offset distributions can be seen in the left part of figure 6.6. The abscissa shows the TDC values measured for the 5 MHz
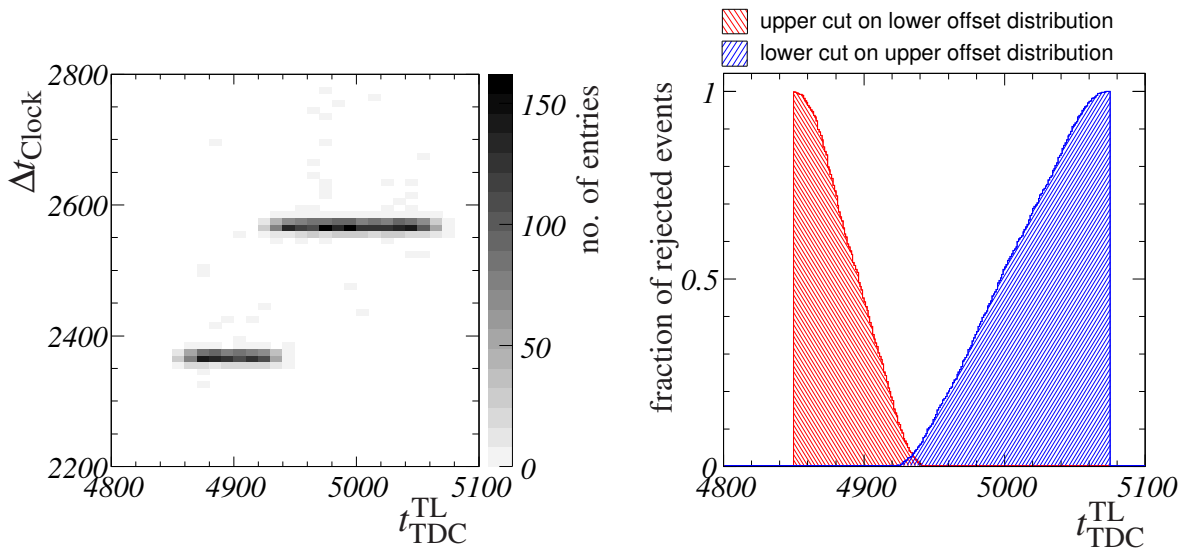
Figure 6.6: Selection of the appropriate offset value according to the measured TDC value of the 5 MHz clock signal $t_{\mathrm{TDC}}^{\mathrm{TL}}$. *Left:* Offset value $\Delta t_{\mathrm{Clock}}$ vs. TDC measurement $t_{\mathrm{TDC}}^{\mathrm{TL}}$. *Right:* Fraction of suppressed events from the lower offset distribution as function of an upper threshold and the fraction of suppressed events from the upper offset distribution as function of a lower threshold.

clock signals, transformed into nanoseconds by multiplying the TDC entries with the TDC resolution of 0.8 ns. Since the online software configures the TDC in a way that TDC hits arriving about $\pm 5\,\mu$s around the stop signal are being stored [Ove04], the TDC values of the 5 MHz clock are distributed between 4860 ns and 5060 ns, close to the stop signal, which represents the center of all possible TDC values ($t_{\mathrm{TDC}}^{\mathrm{STOP}} \approx 5000\,ns$). The

range of measured TDC values t_{TDC}^{TL} corresponds to the time window of 200 ns as expected. On the ordinate the corresponding offsets Δt_{Clock} between the electromagnetic detector of the KASCADE array and the Grande array are shown. A correlation between the separation of the distributions and the range of TDC values t_{TDC}^{TL} for TL_{Grande} is clearly visible. Both ranges of TDC values are filled uniformly as expected, because there is no fixed phase between an EVENT signal and the 5 MHz clock.

Using this information, apart from an overlap region in which the separation is ambiguous, the two offset distributions can be separated by the TDC value t_{TDC}^{TL} measured for the 5 MHz clock. To exclude the overlap region, the effects of an upper and lower cut on the measured TDC value onto the population of the lower and upper offset distributions, respectively, have been analyzed. The results are shown in the right part of figure 6.6. The distribution on the left shows the fraction of rejected events from the lower offset distribution as a function of an upper limit onto the TDC value t_{TDC}^{TL} measured for the 5 MHz clock. The right hand side distribution shows the fraction of rejected events from the upper offset distribution as a function of a lower limit onto t_{TDC}^{TL}.

A symmetrical window of ± 15 ns around the interception point of both distributions at 4935 ns was found in which the separation is ambiguous. Therefore, the offset extracted from the lower offset distribution has to be used for events with $t_{TDC}^{TL} < 4920$ ns. Consequently, the offset extracted from the upper offset distribution has to be used for events with a $t_{TDC}^{TL} > 4950$ ns. In total, 15.2 % of all Grande showers are being discarded by these cuts. The limits hold for the offset between Grande and the electromagnetic detector of the KASCADE array as well as for the offset between the Grande detector and the muon detector, because they are determined by deficiencies of the time measurement of the 5 MHz clock on the Grande side and thus are independent of the detector type on the KASCADE side.

6.5 Summary

In this chapter the determination of the time offset between the electromagnetic or the muon detector of the KASCADE array and the Grande array was described. The offset has to be known in order to extract particle arrival time distributions from time measurements of KASCADE with respect to the arrival time of the shower core calculated from timing information measured by Grande. It has been shown that two contributions to the time mismatch dominate. The first contribution is caused by the differing cable lengths from the detector stations to the data acquisition electronics of the corresponding array. The second contribution is the shift between the 5 MHz clock counter values of KASCADE and Grande. This shift is caused by the relative delay between the reset signals for the clock counters of KASCADE and the Grande array, due to the distance between the KASCADE central detector building and the DAQ station of the Grande array.

The offset was calculated by estimating the true arrival time of the shower plane, first

using KASCADE data only and secondly with Grande data only. Both time estimates were subtracted from each other to provide the desired offset.

A dedicated TDC measurement to measure the time of the 5 MHz signal belonging to the TL information of the Grande data was introduced into the Grande electronics. This TDC measurement allows to determine the global time of single Grande station events. Due to a racing condition this TDC measurement leads to a splitting of the offset distributions by exactly one 5 MHz clock cycle.

The offsets extracted from both distributions have to be used, since most of the data used for the analysis was already taken with the deficiencies of the TDC measurement of the 5 MHz clock signal. It was shown that it is possible to decide on an event-by-event basis which of both offsets has to be used to synchronize the KASCADE array with the Grande array, since certain intervals of TDC values can be assigned to one of the two offsets.

Due to the different experimental setup of the electromagnetic and muon detector of the KASCADE array, separate offset values were determined for both detector types. The offset values extracted from the distributions are listed in table 6.1 for both detector types.

Unfolding particle arrival times from FADC signals

A signal pulse recorded with the FADC system is a combination of the true particle arrival time distribution, the overall detector response and the response of the data acquisition electronics. Hence, a measured signal $S(t)$ is described by a convolution of the true arrival time distribution $T(t)$ and the single particle system response $S_1(t)$

$$S(t) = \int_0^t T(t')S_1(t-t')dt'. \tag{7.1}$$

If the response $S_1(t)$ is known, it is possible to apply an unfolding algorithm to extract the true arrival time distribution $T(t)$ from the measured signal pulse. In this chapter the determination of the input necessary for the unfolding algorithm and the unfolding itself are described.

7.1 The unfolding algorithm

Equation 7.1 is another representation of the general integral equation

$$y(t) = \int R(t,t')x(t')dt'. \tag{7.2}$$

Herein, $x(t)$ denotes the actual spectrum of the observable t, and $y(t)$ represents the distribution arising as a result of the measurement. The function $R(t,t')$ is called response function of the detection system. Solving the integral equation 7.2 represents the general unfolding problem. For a detailed description of the general unfolding problem and a description of various unfolding algorithms see for example [Cow98, Blo98].

In order to process discrete or binned data, the integral equation is approximated by a matrix equation with the integral replaced by a sum over all bins

$$y_i = \sum_{j=1}^{M} R_{ij} \times x_j \qquad \text{with} \qquad i = 1, \dots, N \qquad (7.3)$$

if the discrete values of the measured and the true spectrum are represented as histograms. For a more concise representation, the N elements y_i of the measured data and the M elements of the true spectrum x_i are written as data vectors $\vec{y}$ and $\vec{x}$, respectively, resulting in the equivalent formula

$$\vec{y} = R\vec{x}. \qquad (7.4)$$

The parameter N is the dimension of the measured spectrum, i.e. the total number of samples of the measured FADC signal pulse. M is the dimension of the actual spectrum, i.e. the number of bins of the true arrival time distribution in histogram representation. In general, N and M may differ and the response matrix R is of dimension $N \times M$. In the case of unfolding FADC signal pulses, the measured vector $\vec{y}$ is given by the FADC signal pulse to be deconvolved. A measured FADC signal pulse is represented as a vector or histogram of the FADC samples. Due to the sampling frequency of 1 GHz of the FADC modules, the bin width of this signal histogram corresponds to 1 ns. Therefore, the bin number or sample number translates directly into a time given in nanoseconds. Hence, the total number of samples N of the measured FADC signal pulse corresponds to the length of the signal pulse in nanoseconds. The parameter M is the number of bins of the resulting reconstructed arrival time spectrum. Since both spectra are given in the same units, namely in nanoseconds, the dimension of the measured spectrum N is equal to the dimension of the true spectrum M. Thus, the response matrix is quadratic for the unfolding performed in this analysis and the further description of the unfolding algorithm is only given for this case.

In most cases only the diagonal elements of the response matrix and their neighboring elements differ significantly from zero. Since the off-diagonal elements are close to be symmetric with respect to the diagonal, the matrix is nearly singular and the determinant of the matrix is close to zero ($det\ R = |R| \approx 0$). This makes a simple inversion of the matrix R to solve the matrix equation impossible, because it requires the use of $|R|^{-1}$. Hence, a different strategy is used, which makes the inversion of the detector response matrix R unnecessary. An initial guess of the solution vector $\vec{x}$ is improved step by step that it approaches the measured data $\vec{y}$ when being multiplied with the detector response matrix R. For illustration, this method is explained in the following using the iterative method called the Van Cittert algorithm [vC33]. The iteration formula for the improvement of the solution vector $\vec{x}$ from step k to step $k+1$ is given by

$$x_i^{k+1} = x_i^k + \mu \times \Big(y_i - \underbrace{\sum_{j=1}^{M} R_{ij}x_i^k}_{y_i'^k}\Big). \qquad (7.5)$$

The term in brackets controls the correction of the initial guess for the next iteration step separately for each single element of the solution vector. If the initial value x_i^k is far off,

$y_i^{\prime k}$ is far away from the measured value y_i and the term in brackets, i.e. the correction for the next iteration is large. The correction is small if the initial value is close to the solution or approaches the true value. The parameter μ ensures the convergence of the algorithm and has to be restricted to $0 < \mu < \frac{2}{\lambda_{\max}}$ in which $\lambda_{\max}$ is the largest eigenvalue of the matrix R. The problem of this unfolding algorithm is that it may also provide negative solutions. A negative value represents a negative number of particles arriving at a specific time, which is unphysical.

An alternative unfolding method is the Gold algorithm [Gol64]. It is an extension of the Van Cittert algorithm. The iteration equation of the Gold algorithm is given by

$$x_i^{k+1} = \frac{x_i^k}{\sum_{j=1}^{N} R_{ij} x_j^k} \times y_i. \tag{7.6}$$

Each iteration step is regarded as a more accurate scaling of the elements y_i of the measured data. As seen in equation 7.6, the solution is positive for positive measurements y_i. For this reason and because the algorithm is fast as well, the Gold algorithm was chosen to unfold the PMT signals sampled by the KASCADE FADC system. For the application of the Gold algorithm on FADC signal pulses, the elements of the solution x_i^k represent the elements t_i of the reconstructed particle arrival time distribution $T_{\mathrm{rec}}(t)$ obtained after k iterations.

7.2 Determination of the average minimum ionizing particle detector response

A mandatory input for the deconvolution is the detector response matrix. It has to be constructed from the single particle detector response signal $S_1(t)$, in the following referred to as average minimum ionizing particle (MIP) detector response. Since two types of detectors are being read out by the FADC system, two separate average MIP detector responses, one for the electron detectors and one for the muon detectors, have to be determined.

The detector response is not a constant function which can be determined a priori. It varies during normal operation of the experiment due to changing run conditions like temperature, variations in voltage supply etc.. Therefore, it has to be measured as an average detector signal pulse of many single particle signal pulses recorded during the regular operation of the experiment.

7.2.1 Selection of the FADC signal pulses used for the determination of the average MIP detector response

The DAQ electronics of the KASCADE array does not offer a single particle trigger. Hence, no clean sample of single particle signal pulses was available to determine the average MIP detector response. Instead, regular air shower data had to be used. A disadvantage of this data was that pulses could also originate from two or more particles simultaneously traversing the scintillator.

The reconstructed number of measured particles per detector cannot be used to select single particle events due to the following reason. The reconstruction software only gives an estimate for the number of particles which have crossed the scintillator. This is obtained by dividing the measured energy deposit by the most probable energy deposit E_{MOP} extracted from a calibration spectrum of the corresponding detector [Sch96]. This simple division does not take potential high energy deposits from single particles into account. These would be misinterpreted as energy deposits of two or more minimum ionizing particles. Thus, a cut on the reconstructed number of particles, i.e. a cut on the energy deposit, translates into a cut on the signal amplitude, causing the amplitude of the average MIP detector response to be underestimated. In order to avoid this bias of the average MIP detector response a different method for the selection of FADC signal pulses was chosen.

Since no single particle trigger is available, the use of signal pulses from multi-particle energy deposits cannot be excluded with 100 % efficiency. Only the probability of using such multi-particle events can be reduced. This is achieved by using only particle pulses which are measured by detectors located more than a minimum distance from the shower axis. With increasing distance from the shower axis the particle density decreases and reaches one particle per m^2 or even less. In order to find the minimum distance from the shower center, the spectrum of deposited energy in the detectors was histogrammed for several distance intervals. Sample spectra from the e/γ-detector in array station 11 determined with data from Run 5145 are shown in figure 7.1. The picture shows the distribution of energy deposits measured in the distance ranges $R = (0 - 200)\,\text{m}$ (left hand side) and $R = (200 - 400)\,\text{m}$ (right hand side). The peak at $E_{\text{dep}} \approx 8\,\text{MeV}$ in both spectra represents the energy deposit of a MIP. The spectrum for $R = (0 - 200)\,\text{m}$ shows peaks at about $2 \times 8\,\text{MeV}$ and $3 \times 8\,\text{MeV}$. In the spectrum for $R = (200 - 400)\,\text{m}$ the peak at $3 \times 8\,\text{MeV}$ has vanished, but a deformation of the expected Landau distribution is still visible at $2 \times 8\,\text{MeV}$. Therefore, $R = 400\,\text{m}$ was chosen as the minimum core distance for detector stations providing the FADC signal pulses, which enter the determination of the average MIP e/γ-detector response. This value is in agreement with the radius where the lateral density distribution of electrons reaches one electron per m^2 as shown in figure 7.2.

The corresponding spectra for muons, shown in figure 7.3, are much smoother at energies above the one particle energy deposit. The shape represents a Landau distribution as expected for the energy deposit of a single particle. To be on the safe side, a mini-
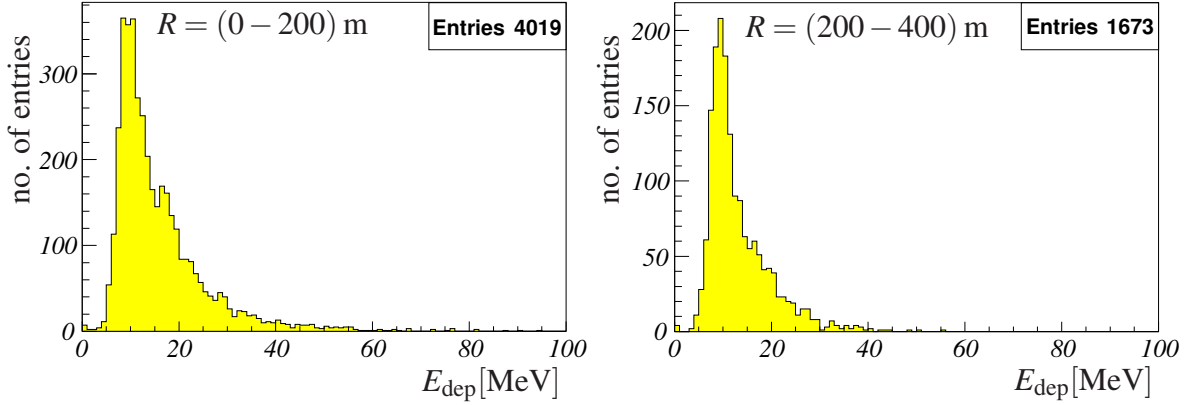
Figure 7.1: Distribution of the energy deposits in the e/γ-detectors for two ranges of the core distance R of the detectors. The deposited energies have been scaled by $\cos\vartheta$ (ϑ zenith angle of the air shower) to cancel the increase of the deposited energies due to the particle inclination. The spectra were determined with data of Run 5145. *Left:* Distribution of the energy deposits in detectors located within the core distance range $R = (0-200)$ m. *Right:* Distribution of the energy deposits in detectors located within the core distance range $R = (200-400)$ m. Both spectra show peaks at a multiple of the single particle energy deposition.

mum core distance of $R = 200$ m was chosen for the detector stations which provide the muon signal pulses to be included in the determination of the average MIP μ-detector response. This value agrees with the point in figure 7.2 where the muon density reaches $1/\text{m}^2$ in the simulated lateral muon density distribution. The lateral particle density, however, depends on the primary energy. At higher energies the initiated air shower extends further and the particle density at a constant distance from the shower core increases. In order to avoid that multi-particle signal pulses from large air showers contribute to the average MIP detector response, a cut on the shower size was applied. Only air showers which triggered less than 30 Grande detector stations are used.

Furthermore, the measured hit pattern is used to reduce the probability of including multi-particle signal pulses. Only those detector signal pulses are used which were marked with a hit pattern indicating that only one cone of the e/γ-detector or one segment of the μ-detector was hit (see table 3.1 on page 24).

The average MIP detector responses are determined by averaging all signal pulses from the corresponding detector type exceeding the lower limit for the distance from the shower core mentioned above. The energy deposit of a particle traversing the scintillator is directly proportional to its path length within the scintillator. The path length is minimal for vertical particles. It increases by the geometric factor $(\cos\vartheta_P)^{-1}$ for a particle with an inclination angle of ϑ_P. The inclination angle is not measured separately for each individual particle by KASCADE-Grande. In a first order approximation the particle's inclination angle ϑ_P coincides with the inclination or zenith angle ϑ of the air shower. Hence, to account for the change in path length within the scintillator material and the related increase in energy deposit, each signal pulse was scaled by the inverse of
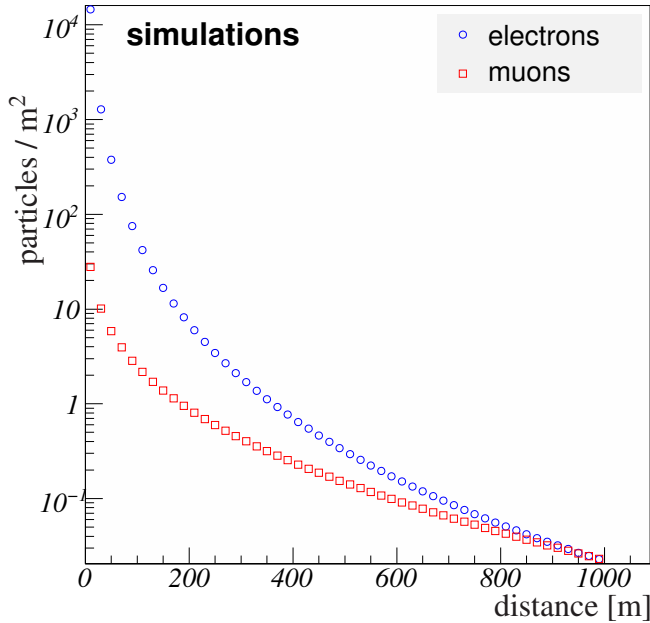
Figure 7.2: Lateral distributions of the electron and muon densities determined from proton and iron showers. For each particle type 50 vertical showers were simulated with primary energies of 10^{16} eV and 10^{17} eV, respectively. The showers were simulated with CORSIKA using the interaction models QGSJET II and Fluka.

the factor $(\cos\vartheta)^{-1}$ before it entered the average MIP detector response. The inversion cancels the effect of the inclination.

Since the threshold, which is used by the data acquisition software of the FADC system to determine the beginning of a detector signal pulse, varies between runs (see section 4.2), the position of the detector signal pulse within the transferred range of data samples also varies. Therefore, in order to prevent a broadening of the average MIP detector response, it is necessary to match the leading edges of the signal pulses which contribute to the average MIP detector response. In each signal pulse, the point on the leading edge is determined where the signal pulse height reaches half of the amplitude with respect to the pedestal. The FADC signal pulses are then summed with respect to this point. In order to determine the pedestal, the mean of 20 samples out of the 100 samples in front of the real particle signal pulse is determined. To assure that no samples at the leading edge are used, these 20 samples are taken from the region starting with sample 51 well before the expected location of the leading edge at about sample 100.

The resulting average MIP detector responses of the electromagnetic and muon detector are shown in figure 7.4. The bump on the right hand side of the peak in the average MIP μ-detector response was already described in [Hor01]. Contributions from the hardware setup like reflections in signal cables are unlikely since the shift of the bump with respect to the maximum does not correspond to any cable length used in the experiment [Hor01]. A study of the origin of this deformation is beyond the scope of this thesis.

7.2.2   Calibration with the mean most probable energy deposit

In order to adjust the average MIP detector response to the current detector performance, a distribution of the detector calibration values was generated in parallel to the averaging
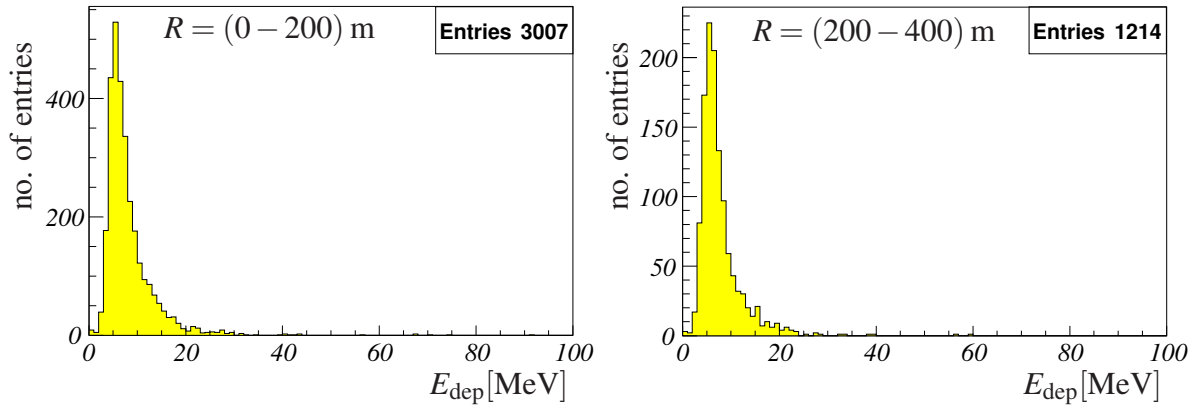
Figure 7.3: Distribution of the energy deposits in the μ-detectors for two ranges of the core distance R of the detectors. The spectra were determined with data of Run 5145. *Left:* Distribution of the energy deposits in detectors located within the core distance range $R = (0 - 200)$ m. *Right:* Distribution of the energy deposits in detectors located within the core distance range $R = (200 - 400)$ m.
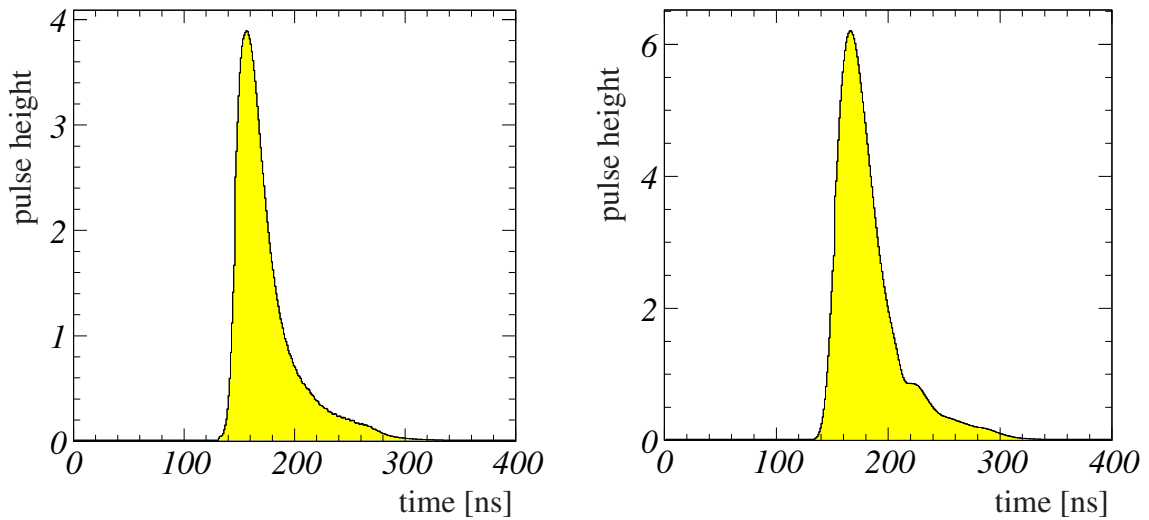
Figure 7.4: Average detector response for a single particle transition as extracted from regular air shower data. *Left:* The average MIP e/γ-detector response. *Right:* The average MIP μ-detector response.

of the FADC signal pulses. These calibration values correspond to the average most probable energy deposit $\overline{E_{\mathrm{MOP}}^{\mathrm{detector}}}$ of a single MIP in the array detectors. These values are taken from calibration spectra, which are filled during the normal operation of the experiment. By fitting these single particle spectra, the most probable energy deposit E_{MOP} of a single particle is extracted as the position of the main peak in the spectrum. As fit function a combination of an approximation to the Landau distribution, the Moyal distribution, and a straight line as background distribution is used [Sch96]. The E_{MOP} value is determined for each detector cone of the e/γ-detector and for each segment of the μ-detector separately. In order to obtain the mean $\overline{E_{\mathrm{MOP}}^{\mathrm{detector}}}$ value for the whole detector type, the reconstruction program KRETA was extended to provide an average from all triggered e/γ-detector cones or μ-detector segments. In order to identify the subdetector components the hit pattern as described in section 3.1.3 is used.

Figure 7.5 shows the distribution of E_{MOP} values belonging to detectors which provided the FADC signal pulses which enter the determination of the average MIP detector response. The mean value of this distribution $< E_{\mathrm{MOP}} >$ is then used to determine a
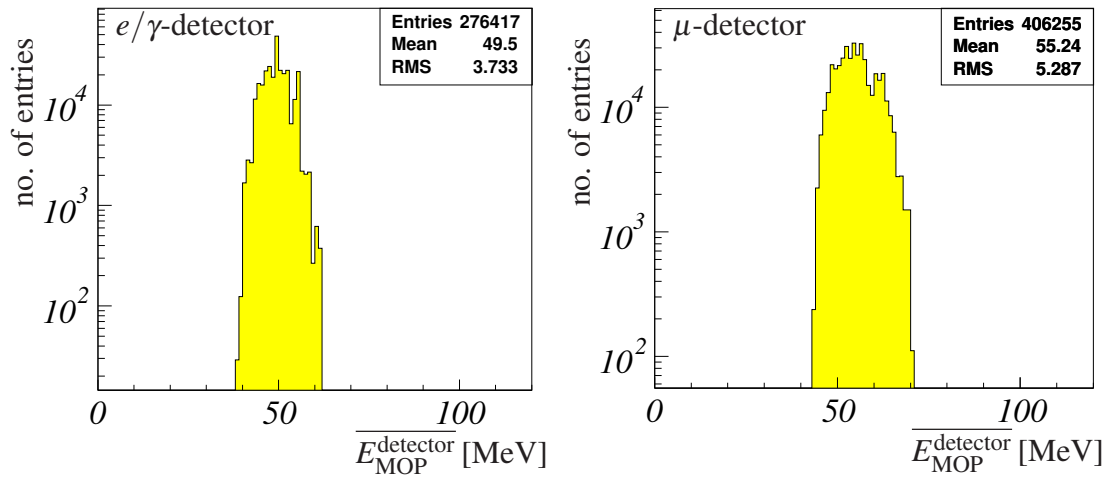
Figure 7.5: Distribution of the most probable energy deposit $\overline{E_{\mathrm{MOP}}^{\mathrm{detector}}}$ for a single minimum ionizing particle. For each FADC signal pulse, which enters the average MIP detector response, the E_{MOP} value of the corresponding detector is filled. *Left:* Distribution of $\overline{E_{\mathrm{MOP}}^{\mathrm{detector}}}$ for the e/γ-detector of all stations with FADC modules except station 16. *Right:* Distribution of $\overline{E_{\mathrm{MOP}}^{\mathrm{detector}}}$ values for the μ-detector of all stations without station 16.

calibration factor

$$f_{\mathrm{cal}} = \frac{\overline{E_{\mathrm{MOP}}^{\mathrm{detector}}}}{< E_{\mathrm{MOP}} >}$$

separately for each FADC signal pulse to be unfolded. The parameter $\overline{E_{\mathrm{MOP}}^{\mathrm{detector}}}$ denotes the run specific average most probable energy deposit of the particular detector which provides the FADC signal pulse. The calibration factor f_{cal} is used to scale the average detector MIP response in order to take variations in detector performance between stations and between runs into account. The advantage of this procedure is that only one average MIP detector response has to be determined, which is used for all stations.

During the determination of the above calibration factor it was observed that the calibration values of station 16 behave differently. The values of $\overline{E_{\text{MOP}}^{\text{detector}}}$ for station 16 are almost twice as high as the values for all other stations. Figure 7.6 shows the distribution of $\overline{E_{\text{MOP}}^{\text{detector}}}$ values for the e/γ-detectors for all stations equipped with FADC modules including station 16. For this picture only a subset of runs was processed to illustrate the characteristics of station 16. This confirms a problem with signal pulses from station
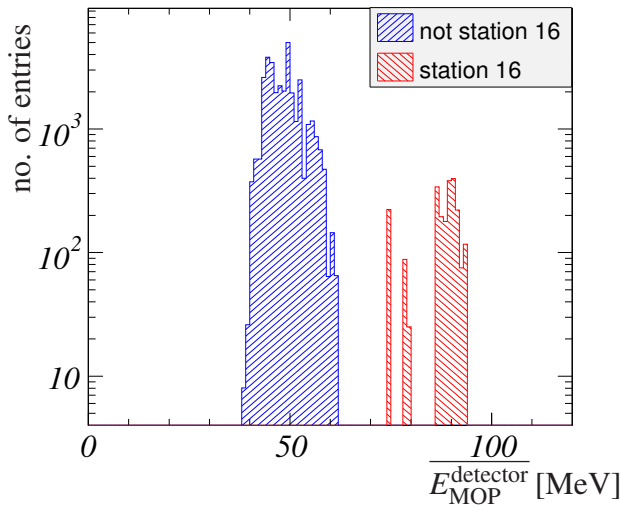
Figure 7.6: Distribution of the most probable energy deposit in the e/γ-detector. The values of station 16 are almost twice as high than the values of all other stations.

16 already observed in [Hor01]. Therefore, FADC signal pulses from station 16 are not used for the determination of the average MIP detector response. Furthermore, to avoid a bias of the unfolded arrival time distributions, station 16 is discarded completely from the data analysis.

7.3 Generation of the response matrix

For each FADC signal pulse to be unfolded a dedicated response matrix is generated by filling the columns of the matrix with the average MIP detector responses. In order to generate a diagonally dominated matrix, the maximum entry of the average MIP detector response has to be aligned with the diagonal of the response matrix. Since the average MIP detector response corresponds to vertical particles, it is scaled by $(\cos\vartheta)^{-1}$ before it is filled into the matrix to account for the effective increase in detector thickness for inclined particle tracks. In addition, it is scaled by the calibration factor f_{cal} to adjust the average MIP detector response to the characteristics of the detector which provided the FADC signal pulse. As an illustration, the upper 50×50 submatrix of example response matrices is shown in figure 7.7. The left hand side corresponds to a part of a response matrix which was generated using the unmodified average MIP detector response of the e/γ-detector. Correspondingly, the right hand side shows a part of a response matrix generated with the non-scaled average MIP detector response of the μ-detector. The axis labeled with "*arrival time [ns]*" represents the bin number within the unfolded arrival time distribution in histogram representation. Since each
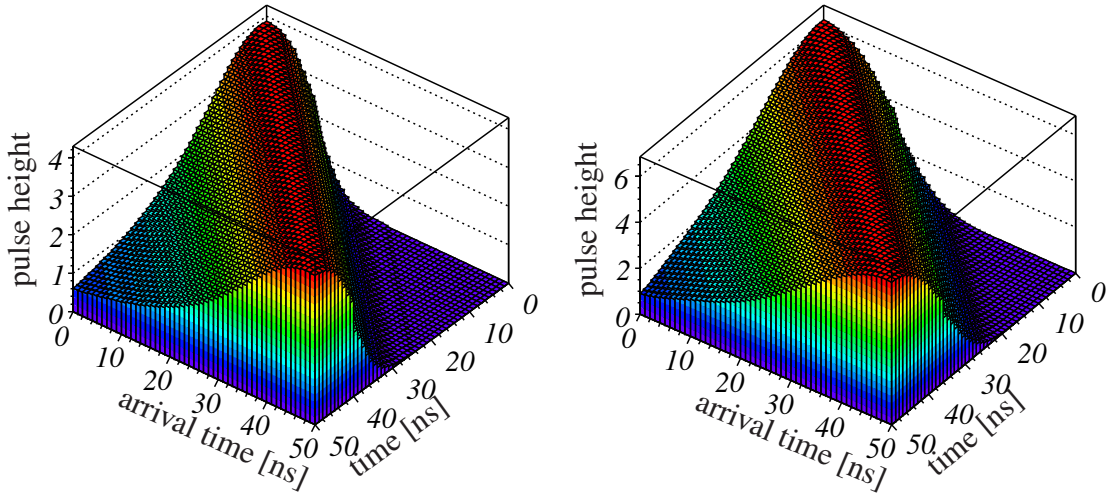
Figure 7.7: The first 50×50 elements of the response matrices. *Left:* Response matrix gener-
ated with the average MIP e/γ-detector response. *Right:* Response matrix gener-
ated with the average MIP μ-detector response.

bin has a width of 1 ns, the bin number corresponds to the reconstructed arrival time in
nanoseconds within the time window given by the length of the FADC signal pulse to
be unfolded. The axis labeled "*time [ns]*" refers to the time axis of the average MIP
detector response representing the columns of the matrices. The z-axis gives the pulse
height of the average MIP detector response in the columns. By adjusting the magnitude
of the elements of the solution vector, i.e. the current guess of the true particle arrival
time distribution hidden in the FADC signal pulse, the unfolding algorithm optimizes
the mixture of average MIP detector responses to fit the measured FADC pulse.

7.4 Determination of the number of iterations for the unfolding algorithm

In order to prevent an unphysical amplification of noise in the FADC signal pulses by
the unfolding, the iterative algorithm has to be stopped after a reasonable number of
iterations. A criterion to stop the algorithm is reached if the solutions $\vec{x}^{(m^+)}$ that are
obtained with more than a reasonable number of iterations m do not differ appreciably
from the solution $\vec{x}^{(m)}$ obtained after exactly m iterations.

In order to find the number of iterations to be used, the behavior of the solution of the
unfolding is tested with signal pulses of Run 5250 for different numbers of iterations.
The FADC signal pulses are unfolded and an overall arrival time distribution is gener-
ated separately for electrons and muons. This is achieved by a simple superposition of
the arrival times unfolded from each single FADC signal pulse without adjusting them
in time. The overall arrival time distributions are compared successively one by one for

increasing number of iterations. Four observables are calculated for each overall arrival time distribution to be used in the comparison of the different solutions. These observables are the mean of the distribution $< t >$, the total number of unfolded particles N, the center of gravity ($< t >_{\mathrm{cog}}$) and the average bin fluctuation $< \sigma >_{\mathrm{bin}}$. The center of gravity is determined from

$$< t >_{\mathrm{cog}} = \frac{\sum_{i=1}^{M} n_i t_i}{\sum_{i=1}^{M} n_i}$$

with M being the number of bins of the overall arrival time distribution which is constant for all numbers of iterations, since always the same set of FADC signal pulses is used. The parameter t_i is the reconstructed arrival time corresponding to bin i and n_i is the bin content, i.e. the number of reconstructed particles at time t_i resulting from the unfolding. The average bin fluctuation corresponds to

$$< \sigma >_{\mathrm{bin}} = \sqrt{\sum_{k=1}^{M} \left(n_k^m - n_k^{m'} \right)^2}.$$

The parameters n_k^m and $n_k^{m'}$ represent the number of unfolded particles in time bin k after m and m' iterations, respectively. In figure 7.8 the behavior of the parameters mentioned above with increasing number of iterations are shown for the arrival time distributions determined from signal pulses of the e/γ-detector. In the following, m refers to the lower number of iterations used for the unfolding and m' to the upper number of iterations. The distribution corresponding to the lower number of iterations m always serves as the reference. Thus, in order to determine the differences between the parameters describing the distributions, the parameter obtained with m' iterations is subtracted from the parameter obtained with m iterations. This is not the case for $< \sigma >_{\mathrm{bin}}$ since it is calculated already from the difference between two overall arrival time distributions obtained with two different numbers of iterations. The expression $(m \; ; \; m')$ denotes the pairs of m and m'. It means that the distribution obtained with m iterations is compared to the distribution obtained with m' iterations.

In the upper left part of figure 7.8 the difference of the mean value of the distribution unfolded with m iterations and the mean value of the distribution unfolded with m' iterations is shown. The error bars correspond to the error of the mean value taken from the distribution corresponding to the lower number of iterations. The errors from both distributions are not added, because they are strongly correlated. The distribution is flat and no dependence on the number of iterations is seen.

In the upper right part, the difference in the number of entries, i.e. the total number of unfolded particles, between distributions resulting from two different number of iterations is shown. The errors represent the statistical error $\sqrt{N}$, with N being the total number of unfolded particles taken from the distribution which corresponds to the lower number of iterations. The number of unfolded particles increases with increasing number of iterations. For $m > 600$ iterations, the total number of unfolded particles is constant.

The lower left figure shows the variation of the center of gravity ($< t >_{\mathrm{cog}}$) for different numbers of iterations used. No dependence on the number of iterations is seen.
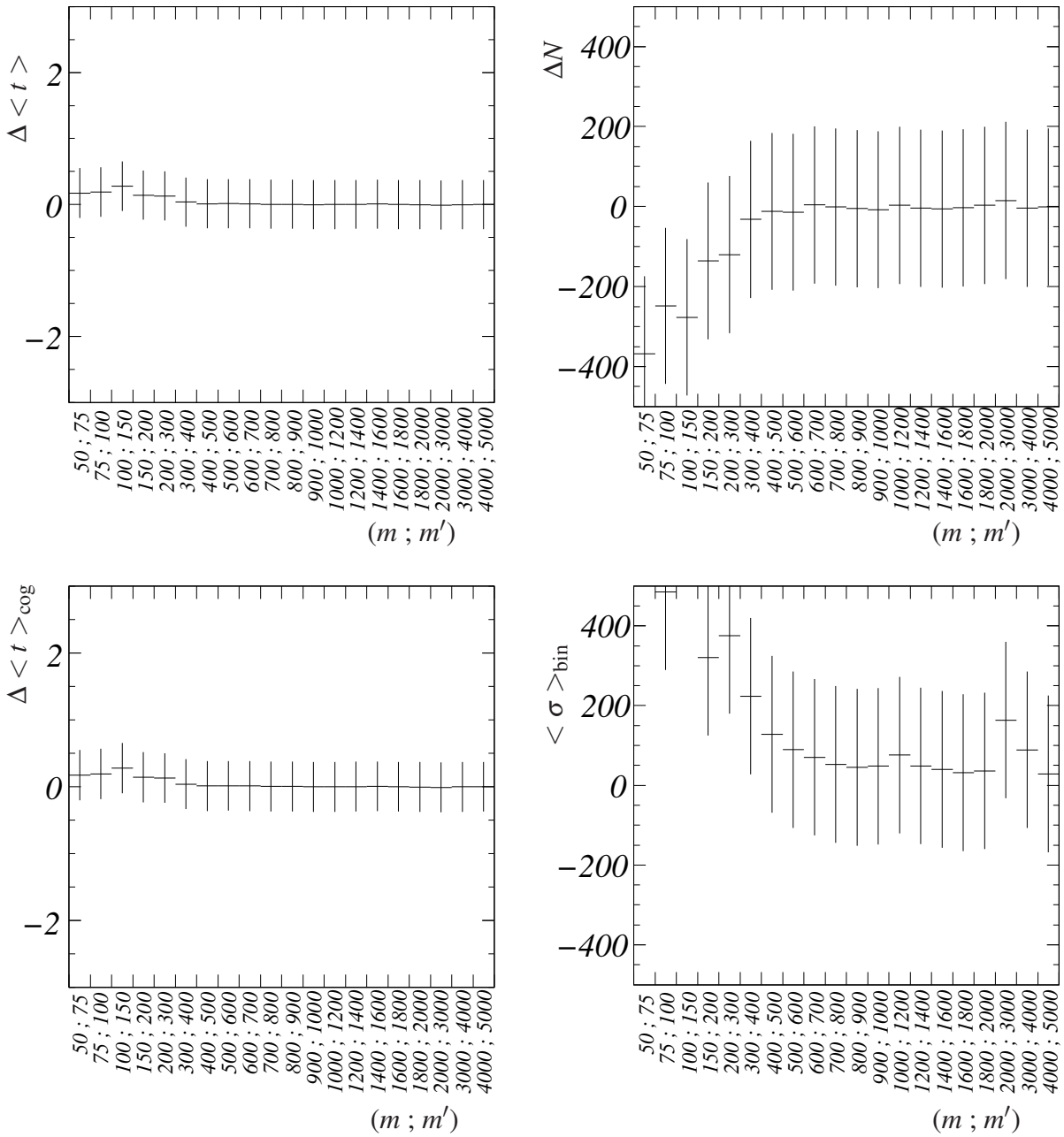
Figure 7.8: Comparison of characteristic quantities of the overall electron arrival time distributions unfolded with a different number of iterations. The graphs show the case for distributions obtained from FADC signal pulses of the e/γ-detector. The expression $(m \; ; \; m')$ refers to the pairs of the lower number of iterations m and the next higher number of iterations m'. See text for details. *Upper left:* Differences in the mean of the distributions. *Upper right:* Differences in the number of entries. *Lower left:* Differences of the center of gravity of the distributions. *Lower right:* Average bin fluctuation between the distributions. Note that the error bars are strongly correlated since always the same sample is used.

In the lower right part of figure 7.8 the average bin fluctuation is shown. This fluctuation is large for a small number of iterations. Above $m \approx 600$ iterations, this fluctuation does not depend on the number of iterations any more. It reaches a constant value of about 50, which has to be compared to the average width of the FADC signal pulses in Run 5250 represented by the average full width at half maximum (FWHM), which is shown in figure 7.9. This average signal pulse width is used as a lower limit for the
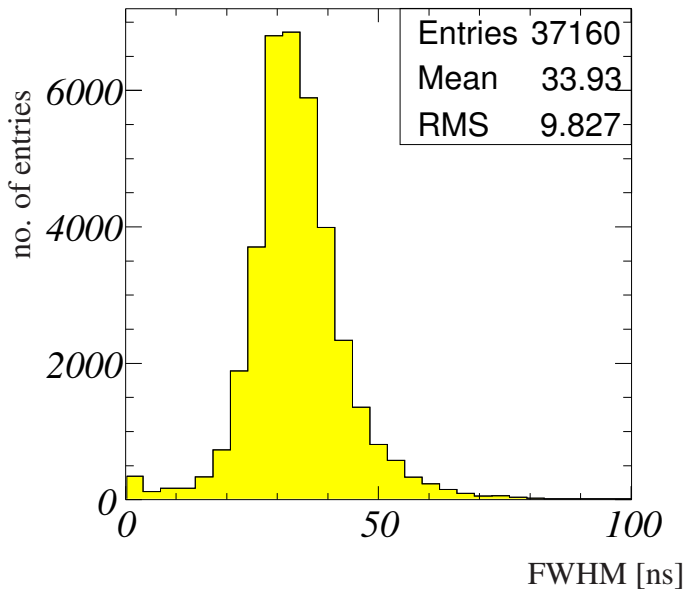
Figure 7.9: Distribution of the FADC signal pulse widths in terms of FWHM for Run 5250.

number of bins occupied by the overall arrival time distribution. The average width determined from Run 5250 corresponds to $< \text{FWHM} > \approx 34\,\text{ns}$ or 34 bins. The average bin fluctuation $< \sigma >_{\text{bin}}$ represents the total sum of individual bin fluctuations and is not yet normalized to the number of bins. Using the lower limit for average width of the overall arrival time distribution 34 ns, the upper limit of the average bin fluctuation per bin corresponds to $50/34 \approx 1.5$. That means, by increasing the number of iterations beyond $m = 600$, the absolute number of particles calculated at a certain arrival time changes by only 1.5 unfolded particles. Compared to the average number of unfolded particles at a certain arrival time, which is in the order of 100, the influence on the total shape of arrival time distributions by this bin fluctuation is negligible.

The variations of the characteristic quantities of the overall arrival time distribution determined from muon FADC signal pulses are shown in appendix B in figure B.1. According to these results, $m = 600$ was found to be a reasonable number of iterations for the unfolding algorithm. All results presented in later chapters are obtained by using this number of iterations.

7.5 Performance of the unfolding algorithm

For each FADC signal pulse to be unfolded a dedicated response matrix is generated. It takes into account the detector performance during the run being analyzed and the

prolonged path length crossed by the particle within the detector material due to its inclination.

It turns out, that the unfolding algorithm is very sensitive to the noise contributions in the pedestal samples before and after the signal pulses. The pedestal samples are selected by the DAQ software of the FADC system and are part of the stored FADC signal pulses. If the unfolding algorithm is applied to the full range of the FADC signal pulses, the algorithm makes no difference between the pedestal samples and samples belonging to the signal peaks. Hence, the unfolding algorithm tries to describe noise contributions in the pedestal samples at the cost of the real signal peaks, which results in less unfolded particles in the signal region. Since the pedestal samples are known not to contain a signal pulse, an additional smoothing of the samples before and after the pulse is applied. Samples within the first and the last 100 samples showing a deviation of less than 1 unit in pulse height are set to the value of the corresponding pedestal. This increases the quality of the unfolded arrival time distribution.

In figure 7.10 example signal pulses are shown together with the corresponding particle arrival time distribution resulting from the deconvolution of these signal pulses. In addition, the forward folded solution is drawn (smooth line) to illustrate the description of the signal pulse by the solution. The small pulse, which is depicted as a dashed line together with the signal pulse and the forward folded solution, represents the adjusted average MIP detector response, which is used to generate the corresponding response matrix. The two graphs on the left hand side show how the unfolding algorithm behaves for small single particle signal pulses. The two graphs on the right hand side show the behavior for FADC signal pulses belonging to the simultaneous measurement of many particles. The lower graphs represent the particle arrival time distributions obtained from the individual FADC signal pulses. Distributions of this kind are used to generate overall arrival time distributions for certain distance intervals as described in chapter 8. Uncertainties of the unfolding algorithm will be discussed in chapter 9.

7.6 Summary

In this chapter, the unfolding algorithm to obtain arrival time distributions from the measured FADC signal pulses was described. From the available unfolding methods the Gold algorithm was chosen, because it is fast and provides only positive entries in the solution vector as required by the nature of the particle arrival time distributions.

The unfolding algorithm depends on a detector response matrix which has to be generated by making use of the average detector minimum ionizing particle (MIP) response. The determination of this response for the e/γ-detector and the μ-detector was described. Since the candidates for single particle FADC signal pulses used for this calculation had to be taken from regular data of extensive air showers, the probability for the inclusion of FADC signal pulses from multi-particle events has to be reduced. This is done by using a lower limit for the core distance of the detector stations which pro-
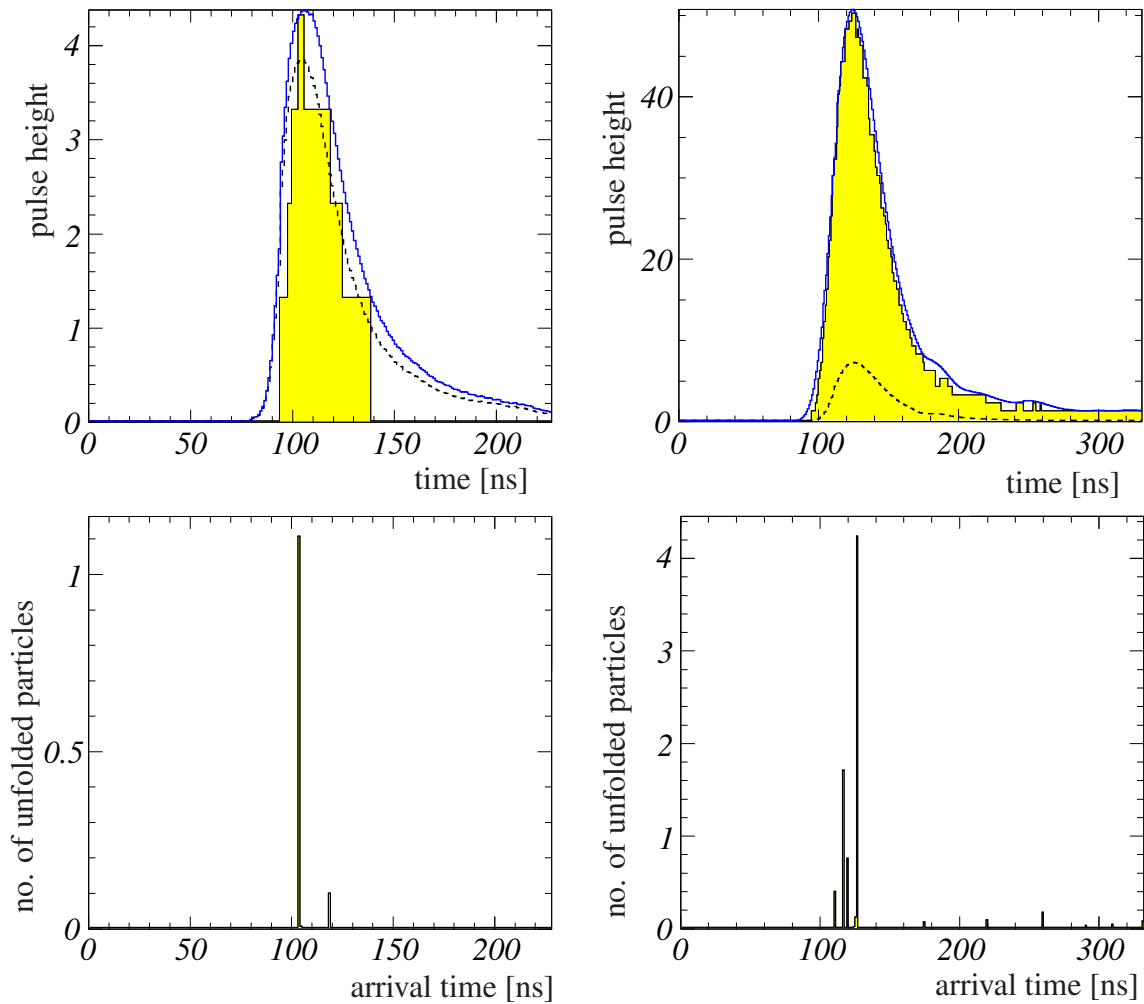
Figure 7.10: Examples of unfolded FADC signal pulses. *Upper left:* The histogram depicts
the FADC signal pulse (from a e/γ-detector) to be unfolded. The size of the
signal pulse suggests a transition of a single particle. The dashed line corresponds
to the average MIP detector response, which was used to generate the response
matrix. The continuous line represents the forward folded solution which is the
product of the unfolded arrival time distribution and the response matrix. *Lower
left:* Unfolded particle arrival time distribution for the signal pulse above. *Upper
right:* The same as for the upper left picture but with a FADC signal pulse (from
a μ-detector) belonging to a multi-particle transition. *Lower right:* The particle
arrival time distribution calculated from the signal pulse above.

vided the FADC signal pulses used for the average MIP detector response. Due to the lateral density distributions for electrons and muons, the average particle density above these limits is less than one per m^2. The lower limit of the core distance for detectors providing the electron signal pulses was determined to $R^e_{min} = 400$ m and $R^\mu_{min} = 200$ m for detectors providing the muon signal pulses.

The preparation of the response matrix was described. Each FADC signal pulse is scaled by a calibration factor f_{cal} and $(\cos\vartheta)^{-1}$ (with ϑ being the zenith angle of the air shower) to take into account the run specific detector performance and the variation of path length of the particle within the scintillator due to the inclination of the particle track.

A study of the behavior of the solution for a different number of iterations used for the iterative unfolding algorithm was presented. For each number of iterations, an overall arrival time distribution is generated. The characteristics of this distributions was described by its mean value, the number of entries, its center of gravity and its average bin fluctuation. It was shown that from $m = 600$ iterations onwards these values do not vary significantly. Therefore, all FADC signal pulses are unfolded using $m = 600$ iterations.

The performance of the unfolding algorithm was illustrated with two example FADC signal pulses. With 600 iterations the unfolding provides a particle arrival time distribution which describes the measured FADC signal pulses well when it is forward folded, i.e. multiplied with the corresponding detector response matrix.

Extraction of particle arrival time distributions

In chapter 2 a simple model has been described which motivates the origin of the difference in arrival time of the electromagnetic and the muonic component of air showers. One contribution to the time difference was identified to be the difference in path-lengths to be traversed by the corresponding particles to reach the same distance from the shower axis. According to the geometry, this difference in path-length increases with the distance from the shower core and accordingly the arrival time difference between electrons and muons. Therefore, it is necessary to study the arrival times of electrons and muons as a function of the distance from the shower axis.

Having only 8 detector stations with a maximum distance of $d = 55\,\mathrm{m}$ in between, it is impossible to study the arrival time difference over the full extension of the shower front on a shower to shower basis. Furthermore, at core distances larger than $R \approx 400\,\mathrm{m}$ the densities of muons and electrons are less than one particle per m^2. The probability that a detector station is being hit simultaneously by more than one particle and of both particle types thus is low. It is only possible to compare electron and muon arrival times on a statistical basis, which requires the extraction of particle arrival time distributions. The only common reference time for all particles measured by different detector types and different detector stations is the arrival time of the shower plane or shower core, respectively. Therefore, in this chapter, the extraction of particle arrival time distributions with respect to the shower plane is described.

8.1 Alignment of unfolded particle arrival times relative to the shower plane

In order to calculate the particle arrival times t_i^{plane} with respect to the shower plane or shower core, the following equation is used

$$t_i^{\text{plane}} = t_j^{\text{detector}} + \frac{z_i^{\text{SDC}} - z_{\text{core}}^{\text{SDC}}}{c} - t_{\text{core}}^{\text{KASCADE}} + t_i. \tag{8.1}$$

The individual terms are described in detail below.

The time t_j^{detector} is the time measurement of KASCADE array station j as described in chapter 6. This time corresponds to the time of the discriminator threshold transition by the detector signal, which is measured with a precision of one nanosecond by a TDC. It reflects the arrival time of the shower front at the position of detector station j.

The detector times t_j^{detector} should only reflect the curvature of the shower front. However, in inclined air showers they contain also the geometrical effect that the observation level is not parallel to the shower plane. A distance d of a detector station to the shower core adds a contribution of $t_\vartheta = d/c \times \sin \vartheta$ to the arrival time of the shower front measured by the specific detector. Depending on the position of the detector station relative to the shower core this contribution may be negative or positive. The effect is illustrated in figure 8.1. In shower disk coordinates (SDC) the contribution is caused by a differ-
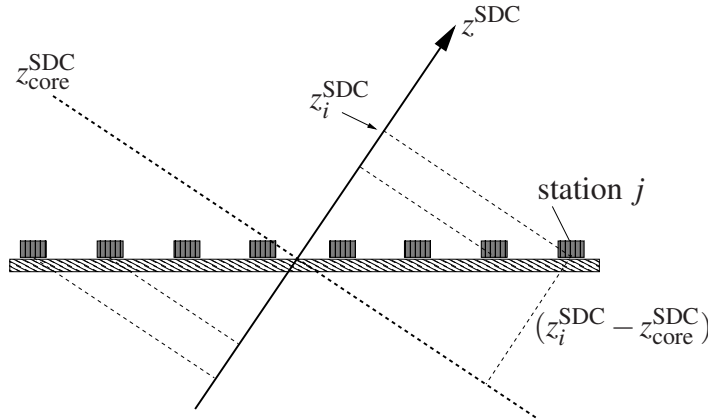
Figure 8.1: Effect of shower inclination on the arrival times.

ence in the z^{SDC}-coordinates between the shower core and the detector station. In order to eliminate the effect of the shower inclination, the detector times t_j^{detector} are corrected by the time contribution caused by the difference in the z^{SDC}-coordinates. This is accomplished by the term $(z_j^{\text{SDC}} - z_{\text{core}}^{\text{SDC}})/c$ in equation 8.1. It represents a transformation of the measured detector times t_j^{detector} into shower disk coordinates or a rotation of the observation level so that it is parallel to the shower plane.

The parameter $t_{\text{core}}^{\text{KASCADE}}$ describes the same time information as the detector time t_{detector}^i but for a virtual KASCADE array detector located exactly at the position of the shower core. This time is not measured, but calculated by transforming the arrival time $t_{\text{core}}^{\text{Grande}}$

into the time reference system of the KASCADE experiment. The transformation of the arrival time $t_{\text{core}}^{\text{Grande}}$ into the time reference system of the KASCADE experiment is performed using the synchronization offset Δt_{Clock} determined in chapter 6 taking into account the delays caused by the assumed cable lengths. The transformation of $t_{\text{core}}^{\text{Grande}}$ into $t_{\text{core}}^{\text{KASCADE}}$ is given by:

$$
\begin{aligned}
t_{\text{core}}^{\text{KASCADE}} &= (\text{TL}_{\text{Grande}} - \text{TL}_{\text{KASCADE}}) + (40\,\text{m} \times 5\,\frac{\text{ns}}{\text{m}} - 700\,\text{m} \times 4\,\frac{\text{ns}}{\text{m}}) \\
&+ (t_{\text{core}}^{\text{Grande}} - t_{\text{TDC}}^{\text{TL}}) + \Delta t_{\text{Clock}}.
\end{aligned}
\tag{8.2}
$$

As described in chapter 6 the parameters $\text{TL}_{\text{Grande}}$ and $\text{TL}_{\text{KASCADE}}$ correspond to the 5 MHz clock counter values which are stored for the event data of the Grande and the KASCADE array, respectively. The numbers in the second pair of brackets in equation 8.2 represent the assumed lengths of the signal cables from the detector stations to the corresponding DAQ electronics station and the approximated signal velocities. The parameter $t_{\text{core}}^{\text{Grande}}$ is the reconstructed arrival time of the shower core or shower plane to be transformed. It is provided by the reconstruction of the Grande showers, which is described in chapter 5. It is obtained by fitting an average shower front to the Grande detector times, which are available as TDC values only. Therefore, the shower core arrival time $t_{\text{core}}^{\text{Grande}}$ is given in TDC values as well. It has to be transformed into a real absolute time value. This is achieved using the TDC value $t_{\text{TDC}}^{\text{TL}}$ which is measured for the 5 MHz clock signal belonging to event timestamp $\text{TL}_{\text{Grande}}$. The parameter Δt_{Clock} represents the offset value determined in chapter 6.

The time values t_i in equation 8.1 represent the particle arrival times which result from the unfolding of the FADC signal pulse. As shown in figure 7.10, the reconstructed particle arrival times t_i are given in the time reference system determined by the length of the unfolded FADC signal pulse. They correspond to the time relative to the first sample of the FADC signal pulse given in nanoseconds. In particular, they contain the time offset with respect to the arrival time of the shower front which corresponds to the 100 samples in front of the first peak of the signal pulse. Therefore, they still have to be aligned to the arrival time of the shower front t_j^{detector} measured by the detector j which provided the FADC signal pulse. This alignment procedure is described in the following.

8.1.1 Determination of the discriminator threshold transition within the FADC signal pulses

In order to align the unfolded particles in time to the arrival time of the shower plane, the time information measured by the KASCADE array stations are used. Each individual time information of a KASCADE array station provides the instant when the threshold of its corresponding discriminator was transcended by the detector signal. This time value is measured with a precision of one nanosecond by a TDC as described in section 3.1.3. The detector signal, which triggers this measurement, is sampled by the KAS-CADE FADC system, but the moment of the threshold transition in the resulting FADC signal pulse is unknown since the discriminator signal is not used by the DAQ of the

FADC system. This problem is illustrated in figure 8.2. The figure shows a sketch of
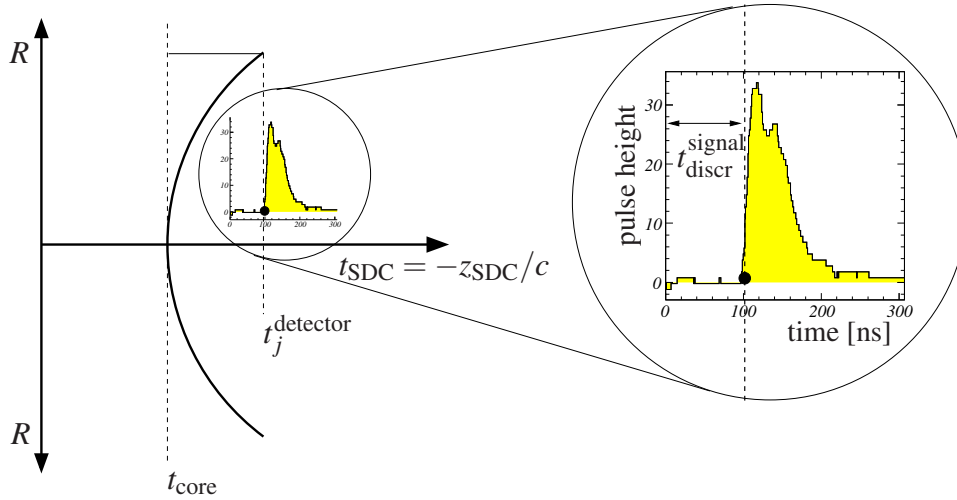
Figure 8.2: Sketch of the alignment of FADC signal pulses to the time of discriminator threshold transition measured by the KASCADE detectors.

the measurement of the shower front arrival time after the transformation into shower disk coordinates. The time value t_{core} represents the arrival time of the shower core and is per definition the earliest arrival time in the shower front. Because of the curvature of the shower front, points on the shower front are measured later for increasing distance to the shower core. The time value indicated by t_j^{detector} represents the time of the threshold transition measured by an arbitrary station j. The FADC signal pulse provided by station j is also sketched. Since the FADC signal pulse contains about 100 samples in front of the first signal peak, the particle arrival times unfolded from the FADC signal pulses cannot be added directly. They still contain the time offset $t_{\text{discr}}^{\text{signal}}$ in nanoseconds. This offset denotes the difference between the first sample of the FADC signal pulse and the sample which corresponds to the moment of threshold transition. The moment of threshold transition is not measured and has to be reconstructed for each individual FADC signal pulse.

In order to find the FADC sample number within the signal pulse which corresponds to the moment of threshold transition, the operation of the discriminator is emulated. As described in section 3.1.3, the discriminator thresholds for the e/γ-detector and the μ-detector are adjusted to 2/5 and 1/3 of the average energy deposit of a minimum ionizing particle (MIP), respectively.

The integral of the detector signal is proportional to the energy deposit in the detector. Therefore, the integrals of the average MIP detector responses of both detector types are used as representative values for the energy deposit of a MIP in the corresponding detector type. By scaling the integral value for the e/γ-detector by 2/5, and the integral value for the μ-detector by 1/5, respectively, a discriminator threshold value in units of the signal pulse integral is derived for each detector type. The time value $t_{\text{discr}}^{\text{signal}}$ within the measured FADC signal pulse, which corresponds to the time of the threshold transition, is then found by iteratively integrating the measured FADC signal pulse from

its beginning to $t_{\text{discr}}^{\text{signal}}$ and comparing the result to the corresponding threshold value. The upper limit $t_{\text{discr}}^{\text{signal}}$ is increased by one nanosecond for each iteration until the integral value exceeds the threshold value. The last value of $t_{\text{discr}}^{\text{signal}}$ is then the moment of threshold transition within the FADC signal pulse.

In order to study the reconstruction accuracy of the time value $t_{\text{discr}}^{\text{signal}}$, the measurement of a detector signal by a KASCADE FADC module is simulated. The average MIP detector response is used as the true continuous detector signal, which is sampled by a simulated FADC module. The contribution of random noise to the signal is generated as random numbers drawn from a Gaussian distribution, which are added to the signals. To determine the width of this Gaussian, a distribution of sample values from the pedestal of the measured FADC signal pulses was generated. The width of this distribution is used as width for the Gaussian smearing. The signal is then sampled with a sample step of one nanosecond by adjusting the value of the pulse height down to the nearest integer. The signal distortion caused by the different characteristics of the four interleaved FADCs per module is simulated as well. Typical values for the differences between the FADCs were extracted from measured FADC signal pulses and are added as different offset values to the samples. A constant offset is then added to all samples to emulate the pedestal. The sampled signal is then processed as described in section 4.3, which includes smoothing and a subtraction of the pedestal. The time value $t_{\text{discr}}^{\text{signal}}$ is then determined by the integral method for the continuous unmodified detector signal and for the sampled and processed simulated FADC signal pulse, respectively. The former is considered as true time of the threshold transition and will be referred to as $t_{\text{discr}}^{\text{true}}$ in the following. The latter is the corresponding reconstructed time value $t_{\text{discr}}^{\text{rec}}$. To study the reconstruction accuracy versus the pulse height, the unmodified signal is scaled accordingly before the sampling is simulated. For each value of the pulse height 100 detector pulses are simulated and a distribution of the differences $(t_{\text{discr}}^{\text{true}} - t_{\text{discr}}^{\text{rec}})$ is generated. The mean values $\Delta t_{\text{discr}} = < t_{\text{discr}}^{\text{true}} - t_{\text{discr}}^{\text{rec}} >$ and the widths (error bars) of these distributions are shown versus the simulated pulse height in figure 8.3. A dependence of the mean

χ^2 / ndf	10.29 / 246
p0	8.268 ± 0.495
p1	-11.31 ± 1.22
p2	-0.1009 ± 0.0182
p3	0.0003544 ± 0.0000894
p4	$-5.393e{-}07 \pm 1.675e{-}07$
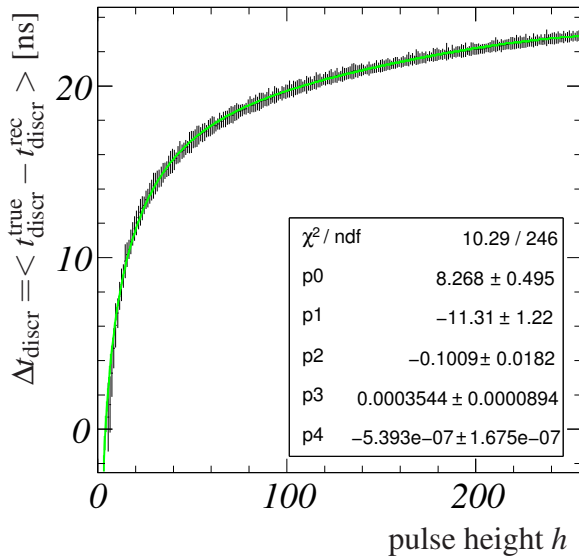
Figure 8.3: Correction to the reconstructed time of threshold transition as a function of the pulse height.

difference Δt_{discr} on the signal height h is visible. The dependence is parameterized by

$$\Delta t_{\text{discr}}(h) = p_0 \times \log(h) + p_1 + p_2 h^2 + p_3 h^3.$$

This deviation results in a systematic underestimation of the time value $t_{\text{discr}}^{\text{signal}}$ and Δt_{discr} has to be added for a correct alignment of the unfolded arrival times.

8.1.2   Accuracy of the reconstructed shower core arrival time

By comparison of the reconstructed shower core arrival time $t_{\text{core}}^{\text{rec}}$ to the true arrival time $t_{\text{core}}^{\text{true}}$ of simulated air showers, a systematic deviation Δt_{core} is observed, which is depicted in figure 8.4 as a function of the electron shower size. The simulated air showers
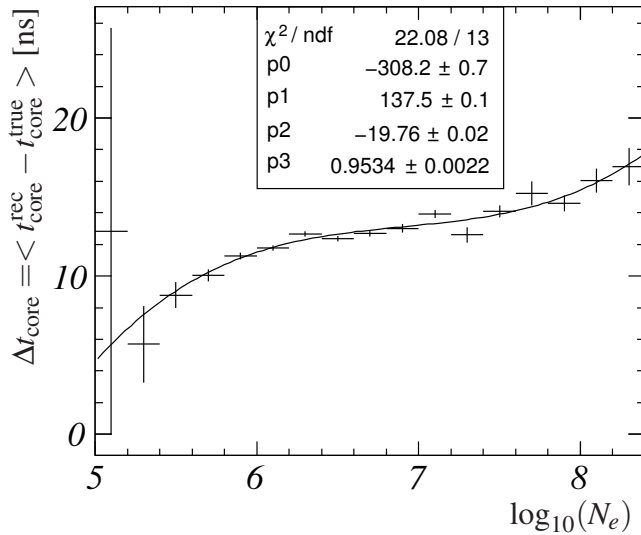
Figure 8.4: Systematic deviation of the reconstructed shower core arrival time with respect to the true shower core arrival time.

are taken from the three simulation sets described in chapter 5. Only showers with a primary energy above 10^{16} eV are used, because the same energy cut is applied to the real data as described later in this chapter. The systematic deviation was parameterized as a function of the logarithm of the shower size N_e by a third-grade polynomial

$$\Delta t_{\text{core}}(\log_{10} N_e) = p_0 + p_1(\log_{10} N_e) + p_2(\log_{10} N_e)^2 + p_3(\log_{10} N_e)^3.$$

This systematic deviation means that the arrival time of the shower core is reconstructed too late. Therefore particle arrival times with respect to the shower core are systematically shortened. Thus, the deviation $\Delta t_{\text{core}}(\log_{10} N_e)$ has to be added to the particle arrival times with respect to the shower plane to correct for this systematic shift.

8.1.3   Application of corrections

By taking the alignment of the unfolded particle arrival times and the systematic correction to the shower core arrival time into account, equation 8.1 changes to

$$
\begin{aligned}
t_i^{\text{plane}} \;=\;& t_j^{\text{detector}} + \frac{z_i^{\text{SDC}} - z_{\text{core}}^{\text{SDC}}}{c} \\
&- t_{\text{core}}^{\text{KASCADE}} + \Delta t_{\text{core}}(\log_{10} N_e) + (t_i - (t_{\text{discr}}^{\text{signal}} + \Delta t_{\text{discr}}(h))).
\end{aligned} \tag{8.3}
$$

In the following, equation 8.3 is used to calculate the unfolded particle arrival times with respect to the shower core. The calculated particle arrival times are used to extract the particle arrival time distributions for the electromagnetic and muonic shower component, respectively.

8.2   Data selection

Since air showers measured by the Grande array are studied with the FADC system which is installed in the KASCADE array, the minimum requirement for the data is, that all three subdetectors, the KASCADE array, the Grande array and the KASCADE FADC system, participated in the measurements. However, the calculation of particle arrival times relative to the shower core requires the transformation of the core arrival time $t_{\text{core}}^{\text{Grande}}$ reconstructed from Grande data into the time reference system of the KASCADE experiment. This transformation is given by equation 8.2. The transformation relies on the TDC measurement $t_{\text{TDC}}^{\text{TL}}$ of the 5 MHz clock signal, which belongs to the time label $\text{TL}_{\text{Grande}}$ representing the timestamp for the Grande event data. Therefore, only data are used for the analysis which include the TDC measurement of the 5 MHz clock signal. The first run which includes the measurement of $t_{\text{TDC}}^{\text{TL}}$ is Run 5240. The last run which is used for the analysis is Run 5599. The runs Run 5509-Run 5533 are excluded since in these runs an extra cable delay of 15 ns was installed in the Grande DAQ electronics as described in chapter 6. This additional delay affects the offset between the KASCADE array and the Grande array and would cause an incorrect transformation of $t_{\text{core}}^{\text{Grande}}$ to $t_{\text{core}}^{\text{KASCADE}}$.

Run 5240 was started on 2005-01-31 and Run 5599 was stopped on 2006-02-13. This corresponds to approximately one year of data taking. As basic data sample serve all air showers measured in this time period which triggered at least a (7/7)-coincidence in the Grande array. In total, 8,331,776 of such air showers have been measured. This sample of air showers is subject to further cuts, which are described in the following.

Minimum number of triggered Grande stations
Studies of the trigger and reconstruction efficiencies for air showers measured with the Grande array have shown that full efficiency is reached for air showers initiated by a primary particle of at least $E_{\text{prim}} = 10^{16}$ eV [Bur06]. Therefore, only showers with at least this minimum energy are included in the analysis to assure that the reconstructed shower

observables are of high quality. However, the primary energy is not determined by the shower reconstruction and is hence not directly available to apply a cut on. A value which is correlated with the primary energy and directly measured by the experiment is the number of Grande detector stations which are triggered by an air shower. In figure 8.5 the increase of this number as a function of the primary energy is shown. The figure
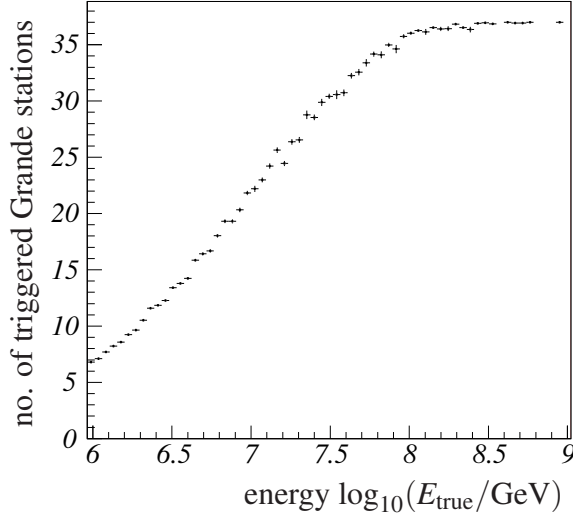
Figure 8.5: Number of triggered Grande detector stations as a function of the simulated primary energy. From primary energies of 10^{16} eV onwards, air showers trigger on average at least 20 Grande detector stations.

was created using one full set (CORSIKA 6.156) of simulated air showers in the energy range from 10^{14} eV to 10^{18} eV. The x-axis shows the true primary energy in the range $E_{\mathrm{prim}}^{\mathrm{true}} = (10^{15} - 10^{18})$ eV. The y-axis represents the mean number of triggered Grande stations for the corresponding primary energy bin. The errors describe the spread of the number of triggered stations divided by the number of showers. At high energies the mean number of triggered stations saturates (as all 37 stations are triggered). And therefore, the errors become small. At an energy of $E_{\mathrm{prim}}^{\mathrm{true}} = 10^{16}$ eV the air showers trigger on average 20 Grande detector stations. Therefore, only air showers are included in the analysis which triggered at least 20 Grande detector stations.

Fiducial area
The reconstructed shower core coordinates $(x_{\mathrm{core}}, y_{\mathrm{core}})$ were restricted to the range $-550\,\mathrm{m} < x_{\mathrm{core}} < 50\,\mathrm{m}$ and $-550\,\mathrm{m} < y_{\mathrm{core}} < 50\,\mathrm{m}$, respectively. This excludes air showers whose core is located outside or at the border of the Grande detector array, for which the reconstruction is likely to fail [Gla05a].

Zenith angle
Air showers with a zenith angle $\vartheta > 30°$ are discarded from the analysis. The reason for this limit is the strong increase of the systematic difference between the reconstructed and the true arrival time of the shower core for larger zenith angles. This behavior is shown in figure 8.6. The set of simulations is identical to the set which was used for figure 8.4.

TDC value of the Grande time label
As described in chapter 6, events cannot be analyzed for which the value of the TDC measurement $t_{\mathrm{TL}}^{\mathrm{TDC}}$ of the 5 MHz signal belonging to the time label of the Grande event
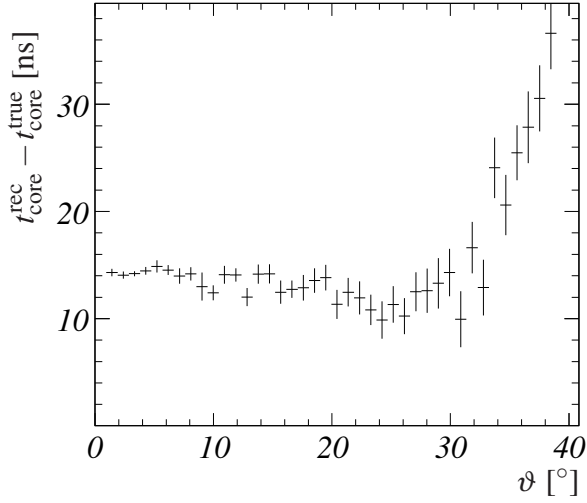
Figure 8.6: Difference between reconstructed and true shower core arrival time as function of the zenith angle. Due to the increase of the systematic deviation for $\vartheta > 30°$ only air showers with a smaller zenith angle are used for the analysis.

data is in the range $4920 \, \text{ns} < t_{\text{TL}}^{\text{TDC}} < 4950 \, \text{ns}$. In this range, it is impossible to decide which of both time offsets has to be used because the assignment to one of the two offset distributions is ambiguous.

Candidates for ANKA induced fake events

During the operation of the Grande array, it was observed that the nearby synchrotron radiation facility ANKA generates fake events in the Grande array during the beam injection phase. In order to exclude these events, a flag in the Grande data is used which marks candidates for ANKA induced events. The flag is set if a typical event signature of ANKA induced events is observed or a corresponding entry is found in a dedicated data base for the ANKA activity.

Successful reconstruction in level 3

As described in chapter 5 a negative-log-likelihood minimization determines all important shower parameters like the core position, shower arrival direction, shower size and the arrival time of the shower core. The most precise values are provided by level 3 of the iterative reconstruction procedure. Therefore, a successful minimization on level 3 is required for the inclusion of an event in the analysis. This selection criterion ensures also the quality requirements for the reconstruction of the shower muon content from the data of the KASCADE muon detectors.

In table 8.1 the cut criteria for the selection of air showers and their effect on the statistics are summarized. In total 291,245 air showers remain after the application of these cut criteria. This represents 3.5 % of the total number of shower events which triggered a (7/7)-coincidence.

8.2.1 Signal selection

The 291,245 events which enter the analysis contain 829,050 FADC pulse signals from the e/γ-detector and 494,656 FADC pulse signals from the μ-detector, respectively.

cut criterion	no. of discarded events (from 8,331,776)	fraction [%]
>20 triggered stations	6,794,864	81.6
core within fiducial area	3,008,121	36.1
zenith angle below 30°	2,170,971	26.1
valid t_{TDC}^{TL}	1,267,267	15.2
ANKA flag not set	585,547	7.0
successful reconstruction	20,387	0.2

Table 8.1: Cuts applied to the data set and their effect on the event statistics with respect to the total number of air showers.

These pulse signals are subject to further selection criteria, which are described in the following.

Station 16
In chapter 7 the distinct behavior of the KASCADE array station 16 was described. Its performance is different from all other stations equipped with FADC modules. For this station, the average calibration factor, which is used to adjust the average MIP detector response, is invalid. Hence, signals from station 16 are excluded from the analysis.

Signal height
Due to the limited dynamic range of the FADC modules, it is possible that the FADC modules saturate for detector signals with a large amplitude. These signals are predominantly measured close to the shower core. These saturated signals are distorted as depicted in figure 8.7. Signals of this kind are discarded from the analysis by applying
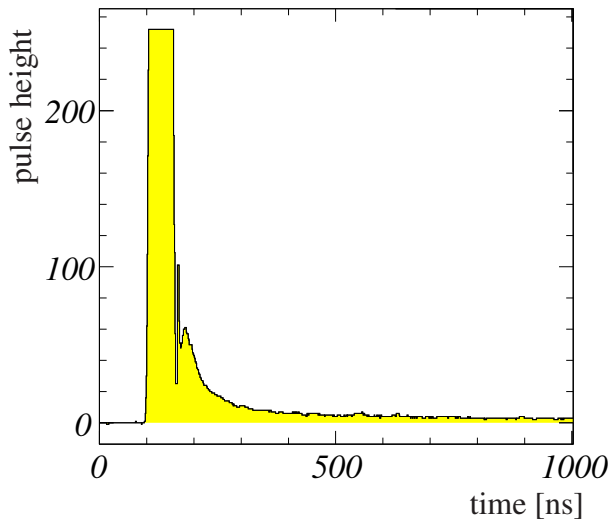
Figure 8.7: Distortion of FADC signal pulses caused by saturation.

an upper cut on the signal amplitude at 240 pulse height units.

Missing time measurement from the KASCADE array station
In some cases the time information $t_j^{detector}$ from an array detector station is missing in the data. Without this time information, the particle arrival time unfolded from a FADC

signal pulse provided by this station cannot be aligned with respect to the shower plane. Therefore, FADC signal pulses are discarded if no time information is provided by the corresponding array station.

The effect of these cut criteria onto the statistics of FADC signal pulses from the e/γ-detector and μ-detector are shown in table 8.2 and table 8.3, respectively. In total 651,133 out of 829,050 (78.5 %) FADC signal pulses from the e/γ-detector and 359,541 out of 494,656 (72.7 %) FADC signal pulses from the μ-detector remain after application of these cuts.

cut criterion	no. of discarded signal pulses (from 829,050)	fraction [%]
amplitude height	25,281	3.1
station 16	111,119	13.4
no time information from detector	37,139	4.5

Table 8.2: Effect of the cuts applied to the FADC signal pulses of the e/γ-detector.

cut criterion	no. of discarded signal pulses (from 494,656)	fraction [%]
amplitude height	5,672	1.1
station 16	60,629	12.3
no time information from detector	63,236	12.8

Table 8.3: Effect of the cuts applied to the FADC signal pulses of the μ-detector.

8.3 Subtraction of the muon content in the electron arrival time distributions

In order to study the difference in the arrival time of the electromagnetic and muonic shower component as a function of the core distance, the arrival times calculated according to equation 8.3 are used to extract particle arrival time distributions binned in 13 intervals of the core distance. These intervals are listed in table 8.4. The widths of these intervals increase with the distance from the shower core to take the decreasing event statistics at larger distances into account. The minimum width of the distance intervals (20 m) is chosen to be larger than the average error of the core position $\langle\sigma\rangle_{\text{core}} \approx 8$ m in order to reduce statistical fluctuations between the distance intervals. The core resolution as a function of the shower size N_e was studied in [Bur06].

The particle arrival time distributions are created separately for both particle types. Example arrival time distributions of electrons and muons are shown in the upper part of figure 8.8 for two ranges of the core distance.

interval	distance range [m]	interval	distance range [m]
1	0-20	8	150-175
2	20-40	9	175-200
3	40-60	10	200-250
4	60-80	11	250-300
5	80-100	12	300-400
6	100-125	13	>400
7	125-150		

Table 8.4: The 13 intervals of distance to the shower core for which particle arrival time distributions are created.
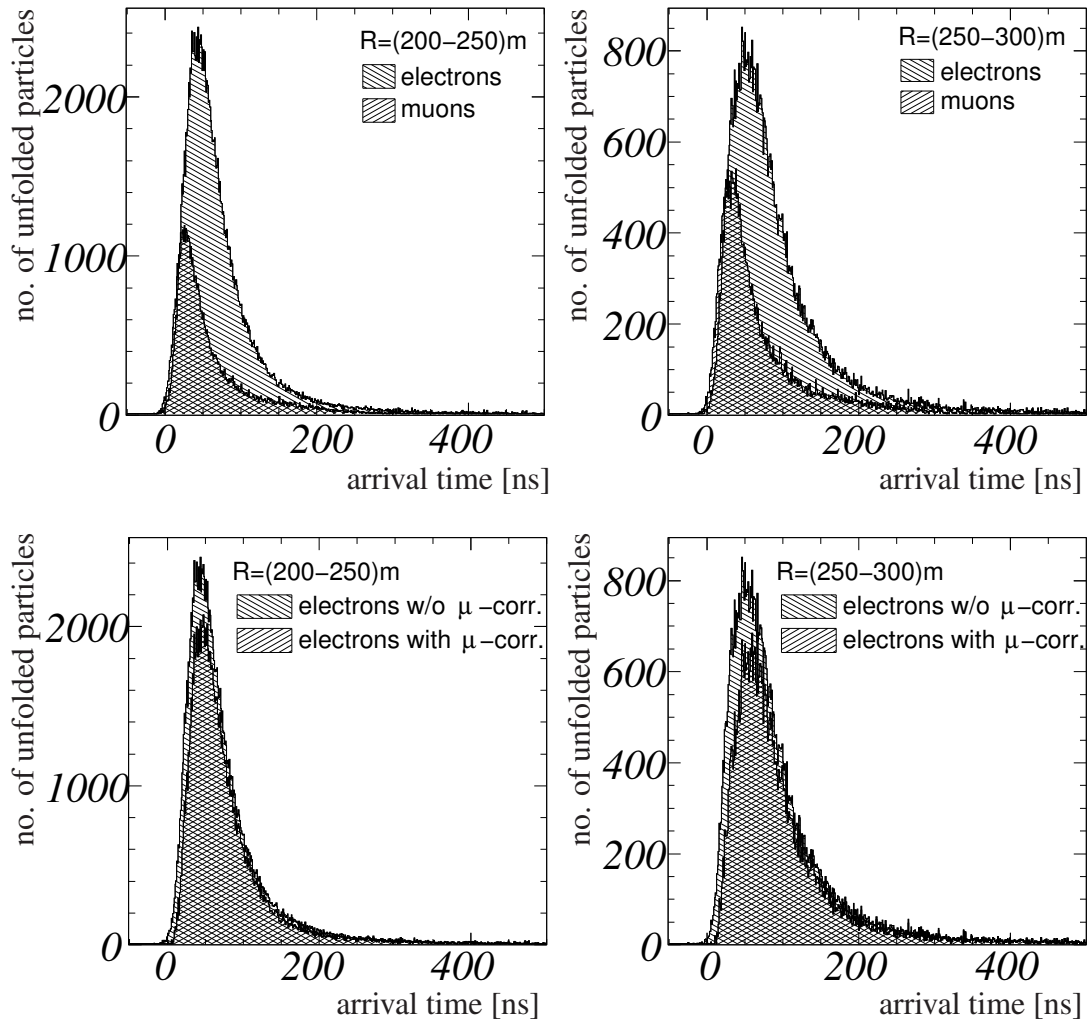
Figure 8.8: *Top:* Example arrival time distributions of the electromagnetic and muonic shower component, respectively, for two intervals of the distance to the shower core. *Bottom:* Illustration of the effect of the subtraction of the μ-content from the distribution of the electromagnetic component. The distributions are shown for the same two intervals of distance from the shower core as in the upper part.

Since the e/γ-detector is located above the μ-detector, it also measures passing muons which are detected by the μ-detector. Therefore, the arrival time distribution of the electromagnetic component also contains the arrival times of the muonic shower component. In order to correct for this contribution, the muon content has to be subtracted from the arrival time distribution of the electromagnetic component. This can only be achieved on a statistical basis by subtracting the arrival time distribution of the muonic shower component. The distribution of the muonic component is scaled down by a factor

$$f = \frac{A_{e/\gamma}}{A_\mu} = \frac{2 \times \pi \times R_{\text{cone}}^2}{4 \times a^2} = 0.4848$$

before the subtraction. This factor arises from the difference between the size of the detection area of the e/γ-detector $A_{e/\gamma}$ and the μ-detector A_μ. The parameter $R_{\text{cone}} = 0.5\,\text{m}$ represents the radius of a single e/γ-detector cone and $a = 0.9\,\text{m}$ is the side length of a single muon scintillator segment. The factor f takes into account that due to the smaller detector area of the e/γ-detector not all muons measured by the μ-detector also passed the two cones of the e/γ-detector. In the lower part of figure 8.8 the effect of this correction on the arrival time distributions of the electromagnetic component is illustrated. The slopes of the leading edges of the arrival time distributions are slightly decreased which shifts the maxima of the distributions to larger arrival times. The correction by the μ-content is applied to the arrival time distributions of the electromagnetic component for all intervals of the core distance. Only the corrected distributions are used for further analysis. In appendix C the arrival time distributions of both shower components are shown for all intervals of the core distance.

The arrival time distributions of the muonic shower component for the first intervals of the core distance, i.e. close to the shower core, show unexpected structures. In the left hand part of figure 8.9 the muon arrival time distribution for the core distance interval $R = (0 - 20)\,\text{m}$ is shown. The structure directly on the right next to the main peak is caused by the unexplained bump in the muon FADC signal pulses, which has
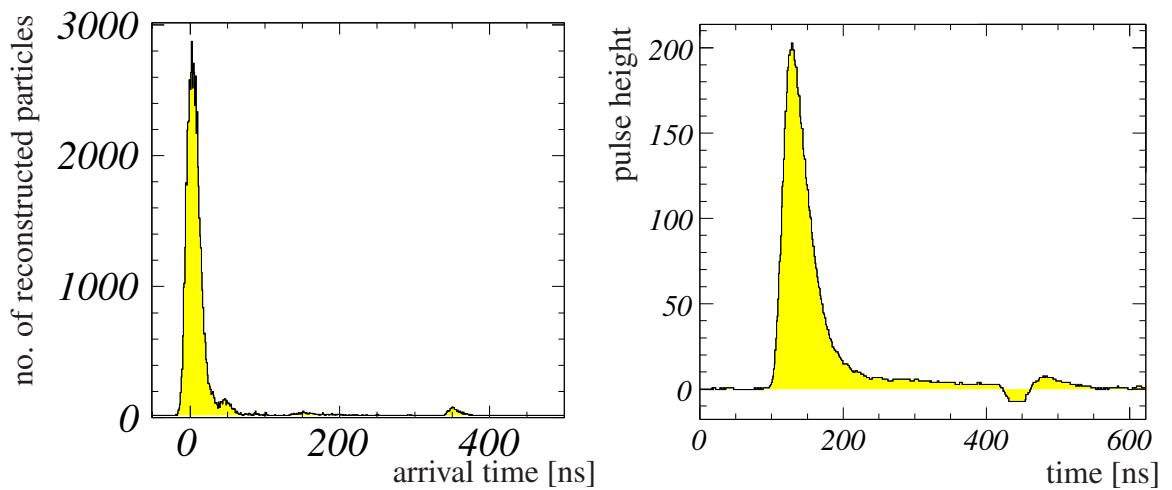
Figure 8.9: *Left:* Muon arrival time distribution for core distances $R = (0 - 20)\,\text{m}$. *Right:* Example of a distorted FADC signal pulse from the μ-detector.

already been described in chapter 7. While the bump is also present in the average MIP μ-detector response used for the unfolding it is not canceled out by the unfolding. The reason is the large size of the bump in FADC signal pulses which are measured close to the shower core. The size of the bump is assumed to be proportional to the amplitude of the detector pulse since it appears only in conjunction with a real detector signal and is never observed by itself. A signal reflection with still unknown origin or a "ringing" of the photomultipliers are the most probable explanations [Hor01]. For detector signals with large amplitudes which are measured predominantly close to the shower core the height of the bump exceeds even the amplitude of the average MIP μ-detector response. For the unfolding algorithm the bump looks identical to a peak caused by delayed particles and the unfolding algorithm tries to describe the bump with a superposition of average MIP μ-detector responses. This results in fake "unfolded" particles with corresponding delays which enter the arrival time distribution and cause the structure to the right of the main peak.

The structure in the arrival time distribution at approximately 350 ns has two reasons. The first reason is that it has a one-to-one correspondence to a distortion in the individual μ-detector FADC signal pulses as shown in the right hand part of figure 8.9. This distortion is caused by a reflection of the detector signal in the cluster electronics stations. This reflection is due to the connection of the 75 Ω signal cables from the detector stations to 50 Ω cables in the electronics station without a proper match of the impedance [Hor01]. The second reason is that this distortion does not enter the average MIP μ-detector response. This is caused by the DAQ software of the KASCADE FADC system. As described in chapter 4, the online software discards FADC samples which do not belong to a detector signal pulse. Only 100 samples before and after the signal pulse are stored permanently. The end of a detector signal pulse is defined as two adjacent samples below the threshold calculated at run start. Since the height of the reflection is proportional to the signal amplitude, it is below the threshold for signals which are produced by a single particle. The DAQ software only transmits the main signal and the following 100 samples. The reflection at 310 ns later is discarded and is thus not included in the determination of the average MIP μ-detector response which only contains FADC signal pulses corresponding to the detection of a single particle. In signals of large amplitude, as measured close to the shower core, the reflection is large enough to be recognized by the DAQ software as a contribution to the detector signal and it is stored together with the detector pulse. As a result of the unfolding this reflection is described by delayed fake particles which enter the arrival time distribution as well.

These effects are associated with signals of large amplitudes only. Because signals with a large amplitude are mainly measured close to the shower core, where the particle density is high, only the time distributions close to the shower core are affected. Furthermore, the muon arrival time distributions for distances close to the shower core are contaminated by electromagnetic and hadronic punch-through. At distances larger than 200 m the effects caused by distorted FADC signal pulses vanish. As will be shown in chapter 9, the distortion of the arrival time distributions for the intervals close to the shower core are of no importance for the results of the analysis.

8.4 Summary

In this chapter the extraction of particle arrival time distributions with respect to the shower core arrival time has been described. For the calculation of the arrival time with respect to the shower core, the reconstructed arrival time of the shower core is subtracted from the arrival time of the shower front measured by the KASCADE array stations. To cancel the effect of the shower inclination, the times from the KASCADE detectors are transformed into shower disk coordinates. A correction is applied to the systematically biased reconstructed arrival time of the shower core. This correction is a function of the shower size $\log_{10} N_e$. It has been determined with simulated air showers by parameterizing the systematic difference between the true shower arrival time and the reconstructed arrival time. The unfolded times are aligned to a reference time given by the time of discriminator transition measured by the KASCADE array detector which provided the FADC signal pulse. This is achieved by reconstructing the position within the FADC signal pulse which corresponds to the time of the discriminator transition of the signal. The accuracy of the reconstructed position has been studied by comparing the positions reconstructed in a continuous signal and reconstructed in the same signal after the latter has been sampled by an emulated FADC module. A systematic deviation has been found which depends on the pulse height. This deviation has been parameterized and included as a correction to the calculation of particle arrival times with respect to the shower plane.

The selection criteria for the air showers and the corresponding FADC signal pulses which are included in the analysis have been described.

The unfolded arrival times from the selected FADC signal pulses have been used to create particle arrival time distributions for the electromagnetic and the muonic shower components. In order to study the difference between the arrival times of both components, the particle arrival time distributions have been determined for 13 intervals of the distance from the shower core.

The arrival time distributions of the electromagnetic component also contain contributions from the muons which passed the e/γ-detector. To correct for this contribution a fraction of the arrival time distribution of the muonic component is subtracted as explained above.

At small distances from the shower core the arrival time distributions of the muonic shower component show unexpected structures. The origin of these structures has been explained as distortions of the FADC signal pulses of the μ-detector introduced by deficiencies of the detector setup. These distortions are considered as real contributions from particle energy deposits by the unfolding algorithm. Hence, the distortions of the individual FADC signal pulses enter the particle arrival time distributions as fake "unfolded" particles. However, these distortions are only present for distances close to the shower core.

Analysis of the particle arrival time distributions

In this chapter, the particle arrival time distributions are used to determine a cut on the particle arrival times, which may be used by an experiment without dedicated muon detectors in order to distinguish between electrons and muons if their arrival times are measured. The muon arrival time distributions contain only muons exceeding the kinetic energy threshold of 230 MeV. The arrival time distributions of electrons analyzed in this chapter have been statistically corrected for the contribution of the muonic shower component. For the particle arrival time cut obtained, the purity of a potential muon number reconstruction is determined. In the second part of the chapter, effects of various systematic uncertainties on the particle arrival time cut and the corresponding muon number purity are studied.

9.1 Determination of the particle arrival time cut

In a first step, the particle arrival time distributions are used to create the time profiles of the electromagnetic and the muonic shower front in order to confirm the expected earlier arrival time of muons as well as the increase of the arrival time difference with the distance from the shower core R. The time profiles for both shower components are shown in figure 9.1. On the left hand side, the mean arrival times for electrons $\langle t \rangle_{e/\gamma}$ and muons $\langle t \rangle_{\mu}$ are depicted as a function of the core distance R. The errors are the errors of the mean $\sigma/\sqrt{N-1}$, with σ being the standard deviation of the distribution and N the number of unfolded particles in the distribution. The errors are smaller than 1 ns and therefore not visible in the figure. Up to distances of $R = 200$ m the difference in the arrival times of electrons and muons amounts to maximal 4 ns. Contrary to the expectation

(see chapter 2), electrons arrive earlier than muons in this distance range. Electrons and photons have a smaller mass than muons. Assuming equal average momenta, particles of the electromagnetic shower component have therefore a higher velocity than muons. The effect of this difference in particle velocity may counterbalance the effect of a difference in path length for distances $R < 200$ m, causing particles of the electromagnetic shower component to arrive earlier than particles of the muonic shower component. For distances $R > 200$ m the time profiles of the shower fronts start to show the expected earlier arrival time of the muonic shower component. As expected, also the difference of the mean arrival times increases with increasing core distance. The right hand part
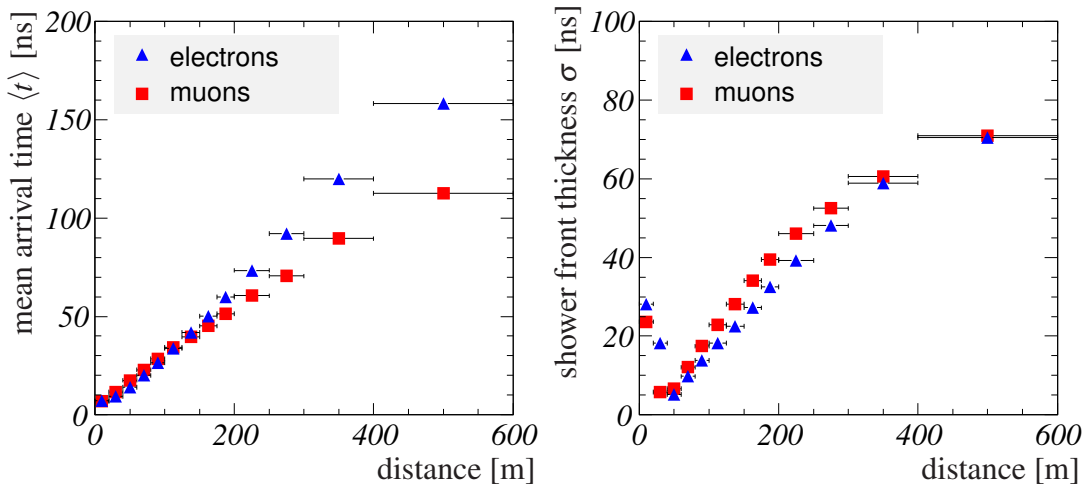
Figure 9.1: *Left:* Mean arrival time of electrons and muons as a function of the core distance according to the mean values of the particle arrival time distributions. *Right:* Thickness of the electromagnetic and muonic shower front as a function of the core distance in terms of the standard deviation of the particle arrival time distributions.

of figure 9.1 shows the average thickness of the electromagnetic and muonic shower front as a function of the core distance. The thickness corresponds to the widths of the particle arrival time distributions in terms of their standard deviation σ. The error of the thickness is calculated according to $\sigma/\sqrt{2 \times (n-1)}$ and is smaller than 1 ns and therefore not visible in the figure. Up to $R = 200$ m, the thickness of the muonic shower disk is on average 10 ns larger than the thickness of the electromagnetic shower disk. This difference decreases for distances larger than $R = 200$ m. For core distances larger than $R = 400$ m, the width of the average muonic shower disk is approximately 5 ns smaller than the width of the average electromagnetic shower front.

The values of the mean arrival times are used to determine an arrival time cut t_{cut} for each core distance interval. This cut is intended to separate the muonic and the electromagnetic shower component. Since muons arrive earlier, all particles measured with $t < t_{cut}$ are considered muons. Accordingly, all particles with $t > t_{cut}$ are considered part of the electromagnetic shower front. As indicated by the time profile of the shower fronts, an application of the cut for $R < 200$ m is impossible. In this distance range, electrons may even arrive earlier than muons. Therefore, the analysis will focus on larger core distances $R > 200$ m and the range $R = (0 - 200)$ m is just analyzed for completeness.

9.1.1 Separation cut values determined from the mean values of the distributions

The separation cut t_{cut} is calculated as the average of the mean arrival times for electrons and muons at the core distance R

$$t_{\text{cut}}^{\text{mean}}(R) = \frac{1}{2} \times \left(\langle t \rangle_{e/\gamma}(R) + \langle t \rangle_{\mu}(R) \right).$$ (9.1)

The error of the separation cut t_{cut} values is calculated via error propagation using the errors of the mean values $\langle t \rangle_{e/\gamma}$ and $\langle t \rangle_{\mu}$. On the left hand side of figure 9.2 the arrival time cut $t_{\text{cut}}^{\text{mean}}(R)$ is shown as a function of the core distance. The vertical errors are smaller than the markers (typically 0.2 ns).
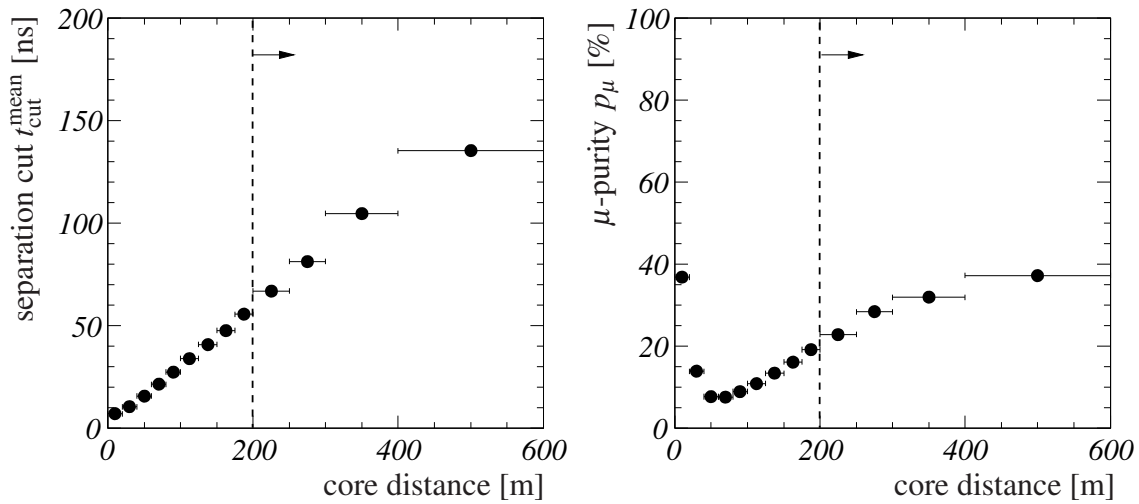
Figure 9.2: *Left:* Separation cut values t_{cut} calculated from the mean values of the particle arrival time distributions as a function of the core distance R. *Right:* The calculated muon purities if the separation cut is applied to the arrival time distributions. The dashed line in both figures indicates the core distance above which a separation of muons and electrons according to their arrival times becomes feasible.

Due to the spread of the particle arrival times, as indicated by the thicknesses of both shower fronts, a 100 % separation of muons from electrons is not achievable. Instead, the estimated muon number will be contaminated by electrons which arrive earlier, i.e. $t < t_{\text{cut}}^{\text{mean}}$. Therefore, applying the separation cut will result in a certain purity of the reconstructed muon number, depending on the exact separation cut value. Hence, the muon purity p_{μ}

$$p_{\mu}(R) = \frac{n_{\mu}(t < t_{\text{cut}}^{\text{mean}})(R)}{n_{\mu}(t < t_{\text{cut}}^{\text{mean}})(R) + n_{e/\gamma}(t < t_{\text{cut}}^{\text{mean}})(R)}$$ (9.2)

is calculated for the separation cut values. Herein, $n_{\mu}(t < t_{\text{cut}}^{\text{mean}})$ denotes the sum of unfolded particles of the muon arrival time distribution with an arrival time earlier than

$t_{\text{cut}}^{\text{mean}}$. The parameter $n_{e/\gamma}(t < t_{\text{cut}}^{\text{mean}})$ denotes the sum of unfolded electrons with an arrival time earlier than $t_{\text{cut}}^{\text{mean}}$. The error of the muon purity is calculated via error propagation using the statistical errors $\sqrt{n_\mu}$ and $\sqrt{n_{e/\gamma}}$. The purity is shown in the right part of figure 9.2. The errors are in the order of 0.5 % and smaller than the markers. Because the arrival time difference for electrons and muons increases with the distance from the shower core, the purity does as well. If the number of muons is calculated by summing all measured particles up to $t_{\text{cut}}^{\text{mean}}$, the purity has to be applied as a correction factor to estimate the true number of muons. The characteristic values of the shower front time profiles, i.e. the mean values and the standard deviations are listed together with the resulting separation cut values and the corresponding muon purities in table D.1 of appendix D.1 for the different intervals in the core distance.

9.1.2 Separation cut values determined from various quantiles of the distributions

In addition, values for the separation cut are determined by calculating the average of the 25 %-quantiles, 50 %-quantiles (median) and the 75 %-quantiles of the electron and muon arrival time distributions. In case of the particle arrival time distribution, the x %-quantile $t^{x\%}$ means that x % of the particles have an arrival time of less than $t^{x\%}$. For example, the 25 %-quantile $t^{25\%}$ is defined by

$$\int_0^{t^{25\%}} \frac{dn}{dt} dt \Big/ \int_0^\infty \frac{dn}{dt} dt = 0.25 \tag{9.3}$$

Herein, dn/dt denotes the particle arrival time distribution being analyzed. The upper limit corresponding to positive infinity is replaced by a reasonable maximum length of the particle arrival time distributions. This value is chosen to 500 ns, which also includes the tails of the arrival time distributions. The separation cut which corresponds to the x % quantile is given by

$$t_{\text{cut}}^{x\%}(R) = \frac{1}{2} \times \left(t_{e/\gamma}^{x\%}(R) + t_\mu^{x\%}(R) \right). \tag{9.4}$$

The calculated values for the separation cut as a function of the core distance R, defined by the quantiles, are shown on the left hand side of figure 9.3. The errors of the separation cut values are calculated via error propagation using the errors of the quantiles. Since there is no method at hand to calculate the error of the quantiles for a large sample, the errors of the mean values are used as an approximation for the errors of the quantiles. The resulting errors are smaller than 1 ns. In the right part of the figure, the muon purities determined from the sum of particles arriving before $t_{\text{cut}}^{x\%}(R)$ are shown. Analog to equation 9.2, they are calculated as

$$p_\mu(R) = \frac{n_\mu(t < t_{\text{cut}}^{x\%})(R)}{n_\mu(t < t_{\text{cut}}^{x\%})(R) + n_{e/\gamma}(t < t_{\text{cut}}^{x\%})(R)}. \tag{9.5}$$
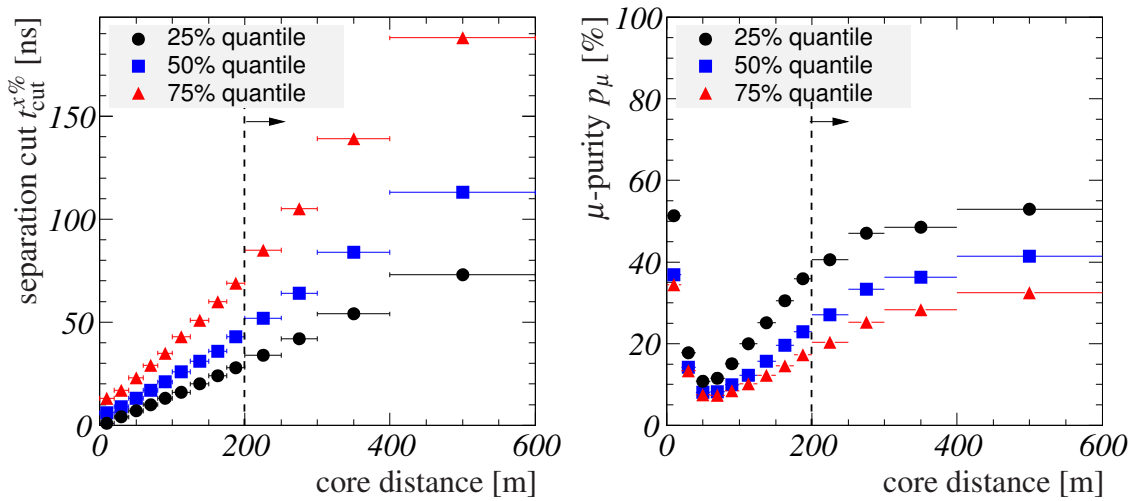
Figure 9.3: *Left:* Separation cut values $t_{\mathrm{cut}}^{x\%}$ calculated from the 25 %-, 50 %- and 75 %-quantiles of the electron and muon arrival time distributions. *Right:* Muon purities corresponding to the separation cut values calculated from the different quantiles. The dashed lines in both figures indicate the core distance above which a separation of muons and electrons according to their arrival time difference becomes feasible.

The values of the 25 %-quantiles, 50 %-quantiles and 75 %-quantiles are listed in tables D.2, D.3 and D.4 in appendix D.2, together with the corresponding values for the separation cuts and muon purities.

9.1.3 Separation cut values determined from results of a Γ-function fit to the distributions

It is a well established practice to analyze the time profile of the shower front by fitting a Γ-function shaped probability density function (Γ-p.d.f.) to the arrival time distributions [Woi75, Agn97]. The Γ-function is defined as

$$\Gamma(t) = a \times t^b \times e^{-ct}. \tag{9.6}$$

The Γ-p.d.f. does not arise from a mathematical model of the shower development. It is empirically justified since its shape is similar to the shape of the arrival time distributions. The Γ-p.d.f. diverges for $t < 0$ and provides a reasonable shape only for $t > 0$. In order to include also the leading edge of the arrival time distributions at $t < 0$ in the fit, the arrival time distributions of electrons and muons are shifted by 1000 ns to later arrival times before fitting them with the Γ-p.d.f.. A location parameter θ has been introduced

$$\Gamma(t) = a \times (t - \theta)^b \times e^{-c(t-\theta)} \tag{9.7}$$

to take this shift into account. As an example, figure 9.4 shows the result of the Γ-function fit to the arrival time distribution of electrons (left hand side) and muons (right hand side) for the core distance interval $R = (250 - 300)$ m.
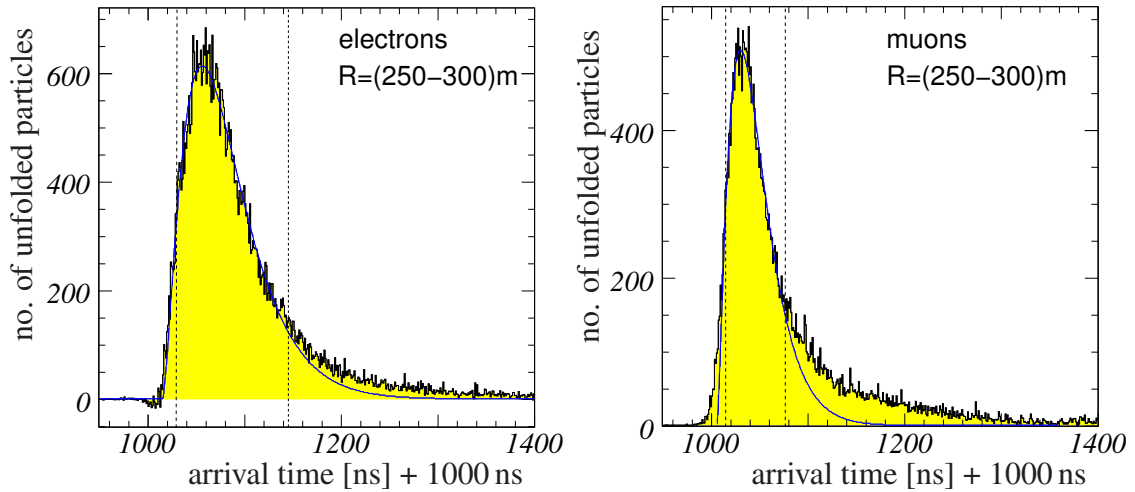
Figure 9.4: Result of the Γ-function fit to the arrival time distribution of electrons (left) and muons (right) in the core distance interval $R = (250 - 300)\,$m. The dashed lines indicate the fit ranges corresponding to the fit results.

The mean value $\langle t \rangle^{\Gamma}$ and standard deviation σ^{Γ} are calculated as

$$\langle t \rangle^{\Gamma} = \theta + \frac{1+b}{c} - 1000\,\mathrm{ns} \qquad \text{and} \qquad \sigma^{\Gamma} = \frac{\sqrt{1+b}}{c}, \qquad (9.8)$$

respectively. The errors of the mean value $\langle t \rangle^{\Gamma}$ and of the standard deviation σ^{Γ} are calculated via error propagation of the errors of the fit parameters. The fit results and their errors are listed with the corresponding fit ranges in tables D.5 and D.6 (in appendix D.3). The time profiles of the electromagnetic and muonic shower front resulting from the Γ-function fit are depicted in figure 9.5. The separation of the muonic and the elec-
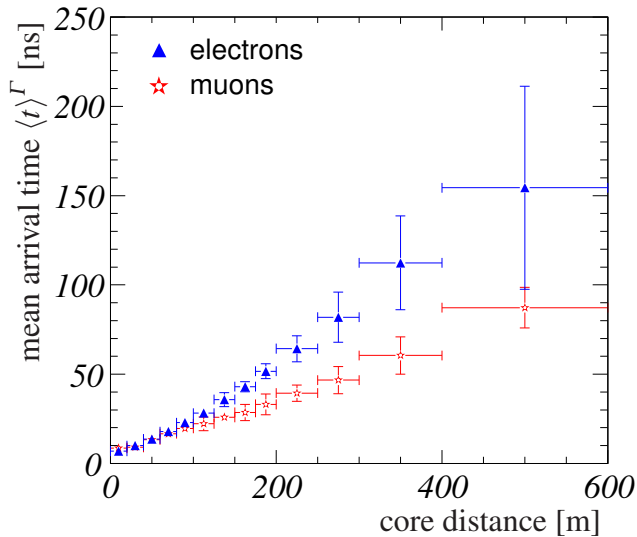
Figure 9.5: Shower front time profile calculated from the results of the Γ-function fit to the particle arrival time distributions.

tromagnetic shower front is more pronounced than for the shower front time profiles extracted from the mean values of the arrival time distributions. The reason is the deficiency of the Γ-p.d.f. to describe the tails of the arrival time distributions. In figure

9.4 this deficiency is visible especially on the right hand side for the muon arrival time distribution. Since the tails of the muon arrival time distributions are more pronounced than the tails of the electron arrival time distributions this leads to a systematic under-estimation of the mean arrival time of the muons. Furthermore, it turns out that the fit values depend strongly on the range of the distribution which is used for the fit. By a variation of the fit range it is observed that the fit results fluctuate by a significant amount of up to 20 ns. The fit results obtained in this thesis correspond to the smallest possible region around the maximum of the distribution for which the fit converged. As minimum width of the fit range the full width at half maximum (FWHM) has been chosen. The maximum of the arrival time distribution has been centered in this fit range. If the fit failed, the fit range has been enlarged iteratively to the right of the distribution until the fit converged. Due to the focus on the peak of the arrival time distribution, the errors of the fit results are large, especially for the core distances of interest $R > 200$ m. The separation cut values which are calculated from the mean values of the Γ-p.d.f. and the resulting muon purities are shown in figure 9.6. The values are also listed in table
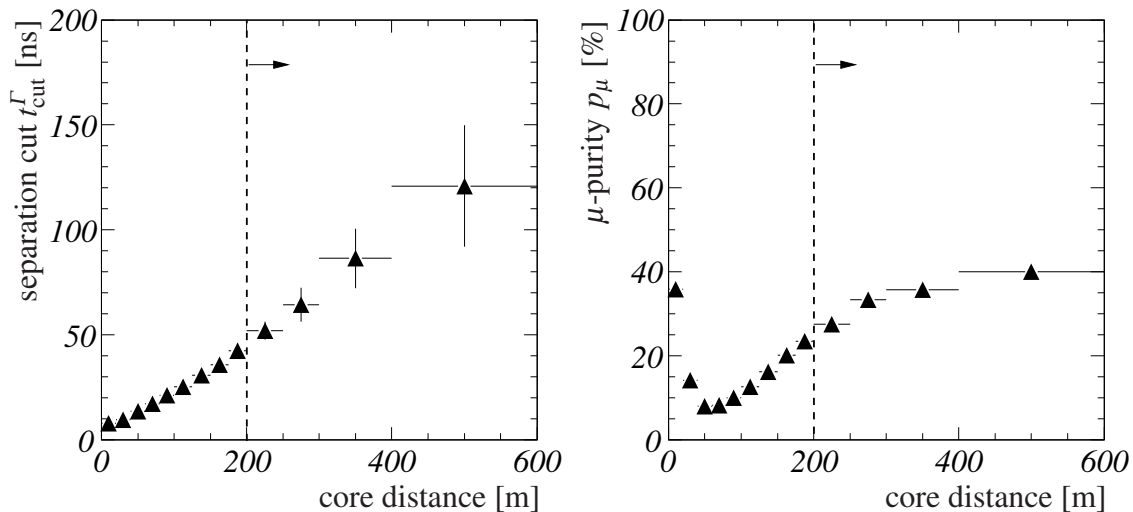
Figure 9.6: *Left:* Separation cut values as a function of the core distance. The cut represents the mean value of the mean values of the Γ-functions fitted to the electron and muon arrival time distributions. *Right:* Muon purities corresponding to the calculated separation cut values. The dashed lines represent the core distance above which a separation of electrons and muons according to their arrival times becomes feasible.

D.7 in appendix D.3. Due to the systematic difficulties introduced by the smaller mean arrival time of the muons, the fluctuation of the fit results varying the fit range and the large errors of the fit results, the separation cut values determined by the Γ-function fit will no longer be considered in the following.

9.1.4 Separation cut values determined from results of a Log-normal-function fit to the distributions

Because the Γ-p.d.f. is unable to describe the tails of the particle arrival time distributions, the Log-normal distribution

$$f(t) = \frac{A}{(t-\theta) \times \sigma \times \sqrt{2\pi}} \times \exp\left(-\frac{1}{2}\left(\frac{\log((t-\theta)/m)}{\sigma}\right)^2\right) \qquad (9.9)$$

is used as an alternative parameterization to describe the arrival time distributions analytically. Herein, σ is the so called shape parameter and m the scale parameter [Eva00]. The Log-normal distribution is only defined for $(t-\theta) > 0$. Therefore, the arrival time distributions are shifted by 1000 ns to later arrival times before fitting. The location parameter θ takes this shift into account. The mean value $\langle t \rangle^{\log}$ and standard deviation $\sigma^{\log}$ are calculated as

$$\langle t \rangle^{\log} = \theta + m \times e^{\frac{1}{2}\sigma^2} - 1000\,\text{ns} \quad \text{and} \qquad \sigma^{\log} = m \times \sqrt{w^2 - w} \quad \text{with} \quad w = e^{\sigma^2}. \qquad (9.10)$$

As for the Γ-fit procedure, the minimum size of the fit range was chosen to be the FWHM. The fit range was centered around the maximum of the arrival time distribution. If the Log-normal-function fit failed, the fit range was iteratively enlarged to the right of the distribution until the fit converged. The resulting fit values and the corresponding fit ranges are listed in table D.8 and D.9 in appendix D.4. As an example, the result of the Log-normal-function fit to the muon arrival time distribution for the core distance interval $R = (200-250)$ m is shown in figure 9.7. Also for the Log-normal-function fit
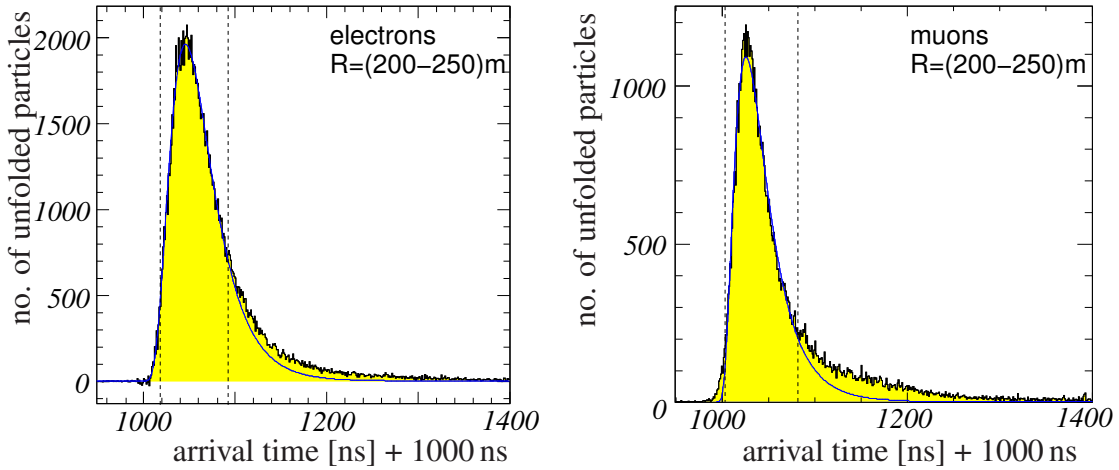
Figure 9.7: Result of the Log-normal-fit to the arrival time distribution of electrons (left) and muons (right) in the core distance range $R = (200-250)$ m. The dashed lines indicate the fit ranges corresponding to the fit results.

it has been observed, that the mean values $\langle t \rangle^{\log}$ and the standard deviations $\sigma^{\log}$ depend strongly on the size of the fit range. The time profiles of the electromagnetic and muonic shower front in terms of the mean values $\langle t \rangle^{\log}$ are shown in figure 9.8. The errors are
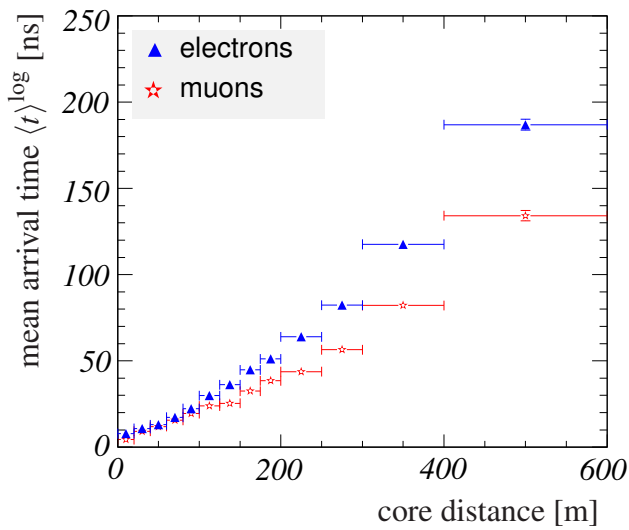
Figure 9.8: Shower front time profile calculated from the results of the Log-normal-function fit to the particle arrival time distributions.

calculated via error propagation of the errors of the fit results. Also in this case the mean arrival time of muons is underestimated because the function does not describe the tails correctly. The separation cut values and the corresponding muon purities calculated from the mean values of the Log-normal-distribution are shown in figure 9.9. The values are also listed in table D.10 in appendix D.4. Due to the systematic difficulties, the Log-normal-function fit will no longer be considered further.
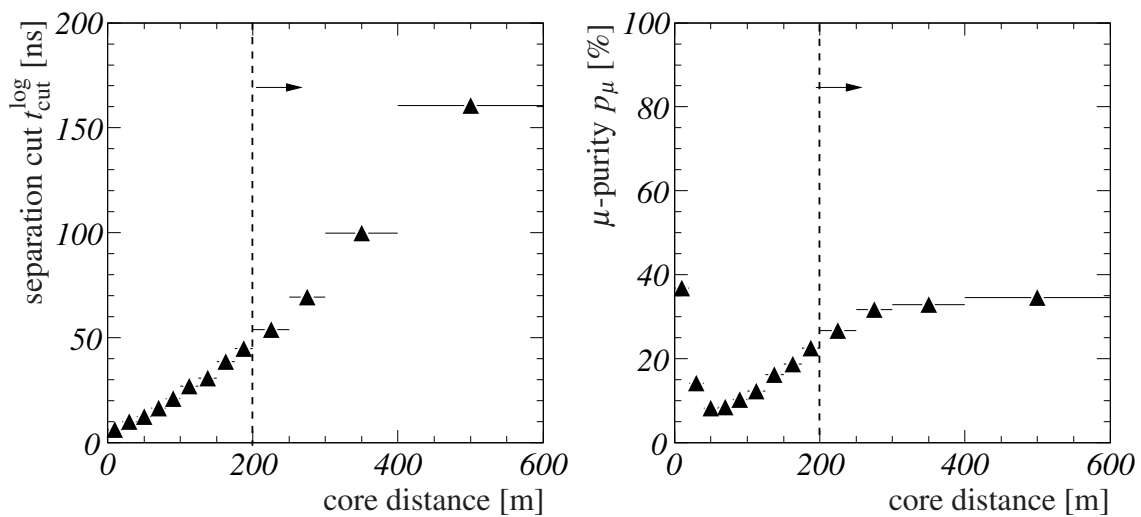
Figure 9.9: *Left:* Separation cut values as a function of the core distance. The cut is calculated from the mean values of the Log-normal-function fitted to the electron and muon arrival time distributions. *Right:* Muon purities corresponding to the calculated separation cut values. The dashed lines represent the core distance above which a separation of electrons and muons according to their arrival times becomes feasible.

9.1.5 Dependence on the zenith angle

The particle arrival time distributions are divided into three ranges of the zenith angle ϑ in order to study the dependence of the separation cut values on the zenith angle. The three intervals are listed in table 9.1. The values represent a constant increase of the at-

interval	1	2	3
ϑ	0°-17.75°	17.75°-24.63°	24.63°-30°

Table 9.1: Zenith angle intervals used to study the dependence on the zenith angle

mospheric thickness in steps of of $50\,\mathrm{g/cm^2}$. From the particle arrival time distributions of all three intervals, the separation cut values and muon purities are determined using the 25 %-quantiles, 50 %-quantiles, 75 %-quantiles and the mean values of the particle arrival time distributions. As an example, in figure 9.10 the separation cut values calculated from the mean values are shown. The left hand side shows the separation cut
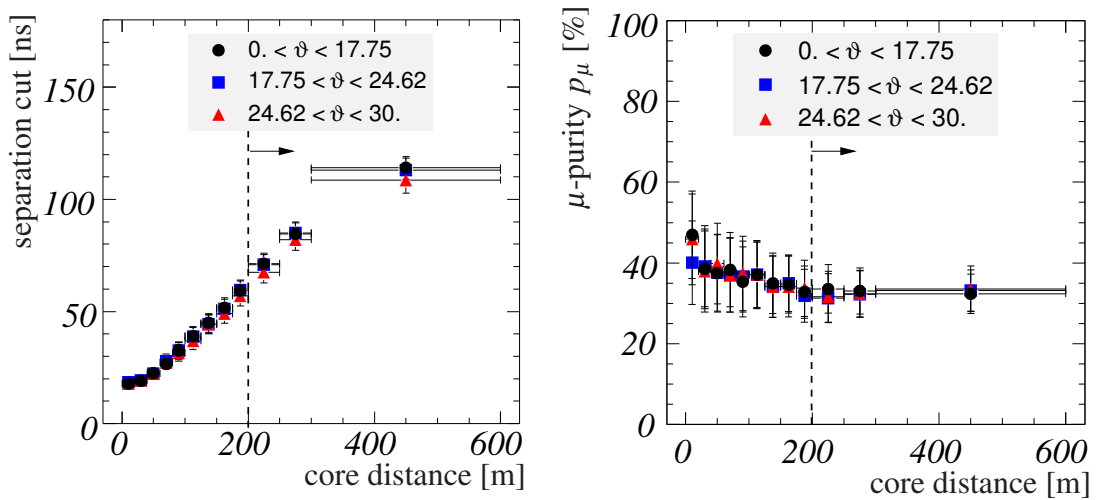
Figure 9.10: *Left:* Separation cut values for the three zenith angle ranges calculated from the mean values of the distributions. *Right:* Muon purities corresponding to the separation cut values for the three zenith angle ranges. The dashed lines represent the core distance above which a separation of electrons and muons according to their arrival times becomes feasible.

values for the three different zenith angle intervals. The right hand part shows the muon purities for the three zenith angle intervals. Since the statistics is reduced by the division into the three zenith angle intervals, the last two core distance ranges have been combined to increase the statistics at large core distances. Furthermore, due to the small statistics in each zenith angle interval the statistical subtraction of the muon content causes distortions in the arrival time distributions of electrons for small distances to the shower core. This affects the calculation of the muon purity. Thus, the dip in the muon purity for core distances $R < 200\,\mathrm{m}$ as visible e.g. in figure 9.2 is not present in figure 9.10. The separation cut values and the muon purities coincide within the statistical

errors. Therefore, neither a significant dependence of the separation cut values on the zenith angle nor a dependence of the muon purities are observed.

9.1.6 Dependence on the primary energy

The extension of the shower front of air showers increases with the primary energy of the incident particle. The particle density at fixed core distance increases with the primary energy as well. This results in changes in the time profile of the shower front. Hence, the dependence of the separation cut value and the corresponding muon purity on the primary energy is studied. The primary energy is estimated for each measured air shower by the formula

$$\log_{10}\left(E_{\text{est}}/\text{GeV}\right) = 0.313 \times \log_{10} N_e + 0.666 \times \log_{10} N_\mu + 1.24/\cos\vartheta + 0.580. \quad (9.11)$$

The parameters N_e and N_μ are the reconstructed electron and muon shower sizes. The parameter ϑ is the reconstructed zenith angle of the measured air shower. Equation 9.11 has been determined by a linear regression analysis of air showers simulated with CORSIKA with fixed energies and five different primary particle types [Gla05b].

The particle arrival time distributions are binned into three intervals of the estimated energy $\log_{10}\left(E_{\text{est}}/\text{GeV}\right)$ in order to study the dependence of the separation cut values on the primary energy. The three intervals are listed in table 9.2. Again the separation

interval	1	2	3
$\log_{10}\left(E_{\text{est}}/\text{GeV}\right)$	6.0-6.6	6.6-7.2	>7.2

Table 9.2: Intervals of the estimated energy to study the dependence of the separation cut values on the primary energy.

cut values and muon purities are determined for all three primary energy intervals using the 25 %-quantiles, 50 %-quantiles, 75 %-quantiles and the mean values of the particle arrival time distributions. As an example, in figure 9.11 the separation cut values and muon purities calculated from the 50 %-quantiles are shown for the three intervals of the primary energy. Since the statistics is reduced by the division into the three primary energy intervals, the last two core distance ranges have been combined to increase the statistics at large core distances. Due to the small statistics in each interval of the primary energy the statistical subtraction of the muon content causes distortions in the arrival time distributions of electrons for small distances to the shower core. This affects the calculation of the muon purity. Thus, the dip in the muon purity for core distances $R < 200\,\text{m}$ as visible e.g. in figure 9.2 is not present in figure 9.11.

Up to the distance $R = 300\,\text{m}$ no dependence on the primary energy is visible. A larger difference is observed for core distances $R > 300\,\text{m}$. These differences in the separation cut values for different primary energies are caused by the different statistics in the particle arrival time distributions. In figure 9.12 the muon arrival time distributions
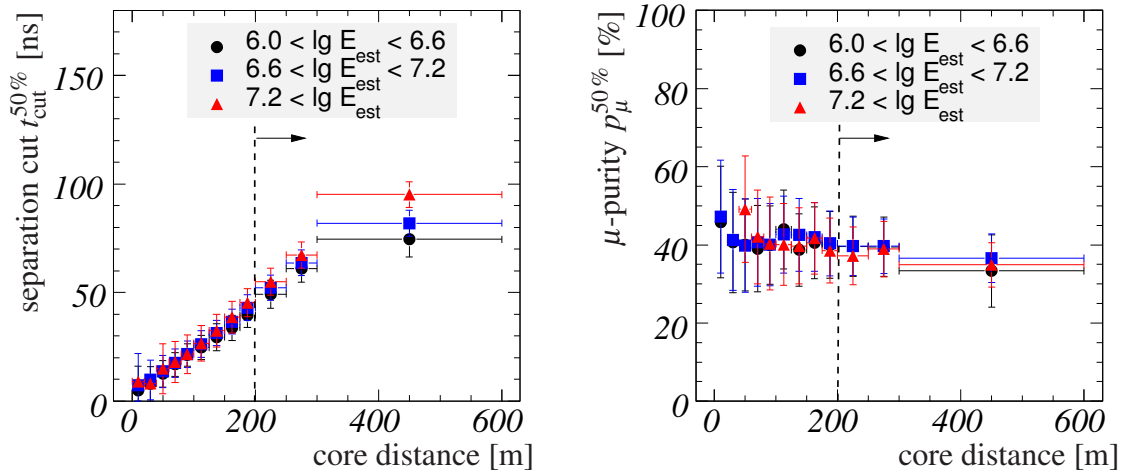
Figure 9.11: *Left:* Separation cut values for the three primary energy intervals calculated from the 50 %-quantiles of the distributions. *Right:* Muon purities corresponding to the separation cut values for the three primary energy ranges. The dashed lines represent the core distance above which a separation of electrons and muons according to their arrival times becomes feasible.

for the estimated energy $6.0 < \log_{10}(E_{est}/\text{GeV}) < 6.6$ and $7.2 < \log_{10}(E_{est}/\text{GeV})$ are shown for core distances $R > 300\,\text{m}$. The muon arrival time distribution is broader for
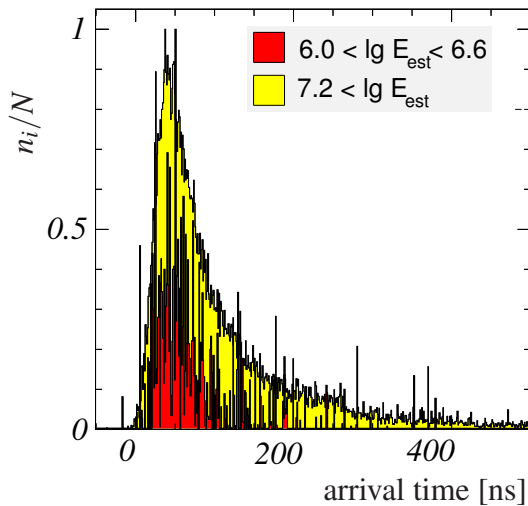
Figure 9.12: Muon arrival time distributions at core distances $R > 300\,\text{m}$ for two ranges of the estimated primary energy. For better comparison, the bin contents n_i of the distributions are normalized by the total number of entries N.

air showers with higher energies. The tail is more pronounced than for air showers with lower energies. This is due to the larger extension of the air showers with higher energies. The particle density at fixed core distance is higher and hence also the probability that delayed particles are measured by the detector. For air showers with lower energies the particle density at large core distances is low. The density of particles with a delay to the foremost part of the shower front is even lower. Thus, the probability that delayed particles hit the detector is lower. Therefore, the tail of the distribution is less occupied. Furthermore, the measured particles of the low energy air showers stem from the

foremost part of the shower front, where the particle density is higher and thus also the probability that a particle hits the detector is larger. Hence, the increase of the separation cut value is an effect of low statistics at large core distances for air showers with low energy E_{est}. In this thesis, no conclusion can be drawn about the systematic dependence of the separation cut value on the primary energy. A detailed analysis requires more data at large distances from air showers with low energy.

9.2 Study of systematic uncertainties

In the following, the systematic errors of the separation cut values $t_{\text{cut}}(R)$ and the corresponding muon purities $p_\mu(R)$ are studied. Systematic uncertainties are introduced by the finite resolution of the shower core position and the uncertainty of the amplitude of the average MIP detector response used in the unfolding. The correction of the shower core arrival time and the correction to the reconstructed position of the discriminator transition have been deduced from simulations. Since the precision of these corrections is not known, they contribute to the systematic uncertainties. Thus, the systematic effect of both corrections on the separation cut values and muon purities is studied.

9.2.1 Influence of the precision of the reconstructed core position

One contribution to the uncertainties of the particle arrival times is the uncertainty in the reconstructed core position. The core position plays a major role for the cancellation of contributions to the shower front arrival time measured by the individual detectors caused by the shower inclination. When the shower front arrival times measured by the detectors are calculated with respect to the arrival time of the shower core, they are transformed into shower disk coordinates (SDC) by eliminating the difference in the z^{SDC}-coordinates between the shower core and the detector stations. The magnitude of the difference in the z^{SDC}-coordinate depends on the core distance of the detector station. Hence, an error of the core position causes an error in the transformation of the shower front arrival times measured by the detectors into SDC. In order to study the dependence of the separation cut values and muon purities on the core position resolution, the reconstructed core position of each measured air shower has been smeared simultaneously in the x- and y-coordinates before the transformation into SDC has been performed. This is achieved by choosing random numbers Δx and Δy from the two-dimensional Gaussian

$$f(x,y) = \frac{1}{2\pi\sigma_x\sigma_y} \times \exp\left[-\frac{1}{2}\left(\left(\frac{x}{\sigma_x}\right)^2 + \left(\frac{y}{\sigma_y}\right)^2\right)\right] \tag{9.12}$$

and adding them to the reconstructed shower core coordinates. The two-dimensional Gaussian is chosen to be symmetrical, i.e. $\sigma_x = \sigma_y = \sigma$. The parameter σ represents the width of the Gaussian and controls the amount of smearing of the core position. The

particle arrival time distributions have been reconstructed for several values of σ and the separation cut values and muon purities have been calculated. As an example, in figure 9.13 the deviations of the separation cut values with core position smearing from the separation cut values without the additional core position smearing are shown. The
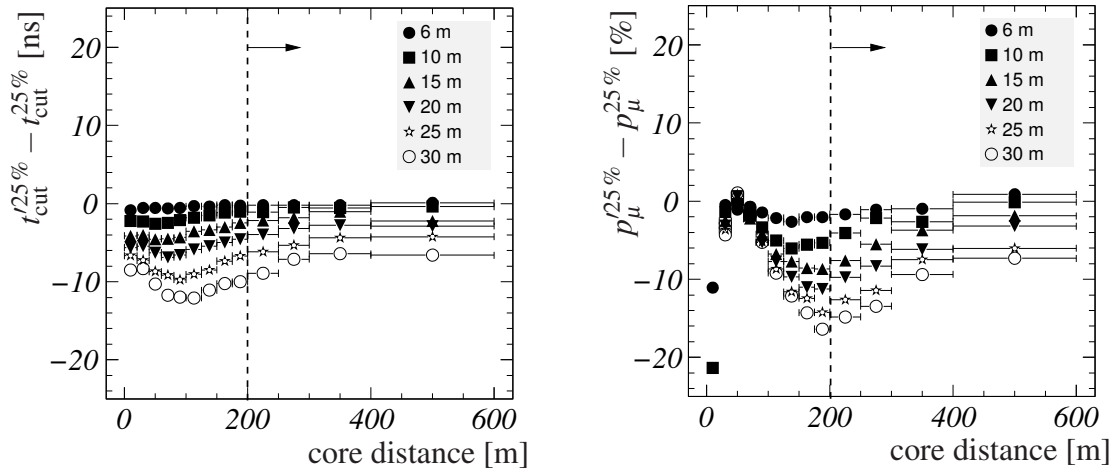
Figure 9.13: *Left:* Relative deviation of the separation cut values calculated from the 25 %-quantile for various values of the core position smearing. *Right:* Relative deviation of the muon purities corresponding to the separation cut values for various values of the core position smearing. The dashed lines represent the core distance above which a separation of electrons and muons according to their arrival times becomes feasible.

core position has been smeared using the values $\sigma =$ 6 m, 10 m, 15 m, 20 m, 25 m, 30 m. The separation cut values shown are calculated using the 25 %-quantiles of the arrival time distributions since the deviations are largest for this case. The impact of the core position smearing on the separation cut values determined from all quantiles and the mean values of the particle arrival time distributions are shown in figures D.1 and D.2 in appendix D.5. The figures show that the deviations increase with a larger amount of smearing. The smearing of the shower core position causes a broadening of the arrival time distributions. Therefore, the values corresponding to the 25 %-quantile shifts towards earlier arrival times and the deviations are always negative. The core smearing causes also a broadening of the tails of the distributions. Thus, the 75 %-quantiles and the corresponding separation cuts are shifted to later times and the deviations are all positive. The separation cuts calculated from the 50 %-quantiles are less affected. The broadening at the beginning and the end of the distributions counterbalance for the calculation of the 50 %-quantile or the median. The impact of the core position smearing onto the separation cut values calculated from the mean values of the arrival time distributions is also small. The impact on the muon purities is even smaller than it is the case for the 50 %-quantiles. Therefore, the separation cut values and muon purities calculated from the mean values and the 50 %-quantiles are favored.

The average resolution of the shower core position of the Grande reconstruction amounts to $\sigma \approx 8$ m. The systematic deviations calculated from the smearing of the shower core

position corresponding to this average resolution are used to correct the results of the separation cut values and muon purities.

9.2.2 Influence of a variation of the average MIP detector response

In chapter 7 the determination of the average minimum ionizing particle (MIP) detector response of the electron and the muon detector has been described. In order to prevent that multi-particle events are included in the determination, a minimum distance from the shower core had been required for the detectors which provided the FADC signal pulses. A comparison between the average MIP detector responses determined for small and large core distances shows a difference in the amplitude as shown in figure 9.14. The
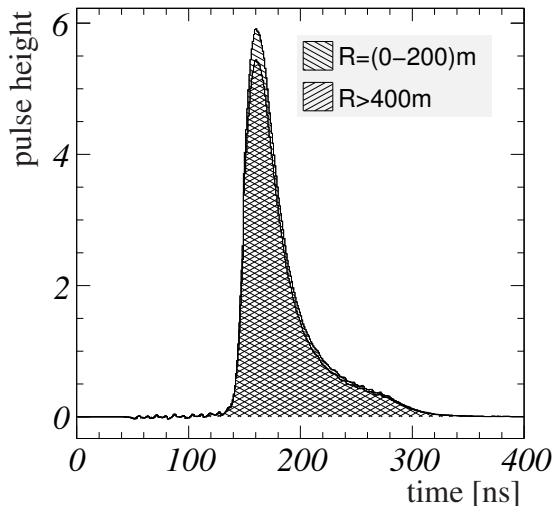
Figure 9.14: Two average MIP detector responses for two different intervals of the core distance.

figure depicts the average MIP detector response of the electron detector for core distances $R = (0 - 200)\,\mathrm{m}$ in comparison to the average MIP detector response for core distances $R > 400\,\mathrm{m}$. The difference of the amplitudes amounts to 9.2 %. Therefore, the choice of the minimum core distance represents a cut on the amplitude of the average MIP detector response. A smaller value of the minimum core distance cut increases the average amplitude and a larger value lowers the average amplitude. Furthermore, scintillator edge effects are not considered. Single particles penetrating the scintillator at the edges could leave the scintillator through the edges without passing the full material. The corresponding smaller FADC signal pulses enter the determination of the average MIP detector response as well. However, the uncertainty of the amplitude of the average MIP detector reponse introduced by this edge effect is small compared to the approximately 10 % uncertainty discussed above.

The results of the unfolding are sensitive to the height of the average MIP detector response. With a larger amplitude small structures in the FADC signal pulses have a lower weight and large peaks in the FADC signal pulses are favored at the cost of small peaks. A smaller amplitude of the average MIP detector response results in a higher weight of small structures in the FADC signal pulses. To study the impact of the amplitude of

the average MIP detector response on the separation cut values and muon purities, the FADC signal pulses have been unfolded with modified average MIP detector responses. They have been scaled to 50 %, 75 %, 90 %, 110 %, 125 % and 150 % of their original amplitude. The deviations of the separation cut values and the muon purities with respect to the values obtained from the unfolding with the unmodified average MIP detector responses are shown in figure 9.15 for the values calculated with the 50 %-quantiles. The impact of the variation of the average MIP detector response on the separation cut
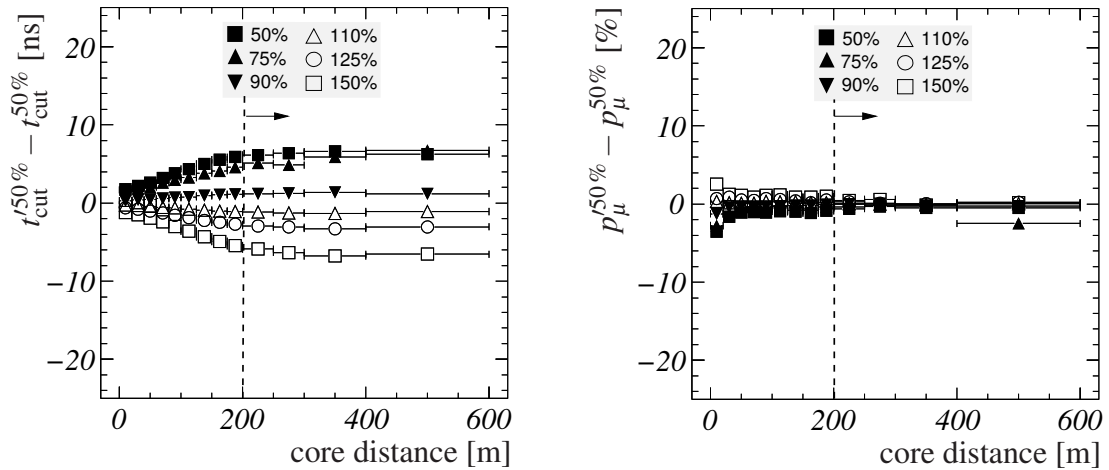
Figure 9.15: *Left:* Relative deviation of the separation cut values calculated from the 25 %-quantile for different sizes of the average MIP detector response. *Right:* Relative deviation of the muon purities corresponding to the separation cut values for different sizes of the average MIP detector response. The dashed lines represent the core distance above which a separation of electrons and muons according to their arrival times becomes feasible.

values determined from all quantiles and the mean values are shown in figures D.3 and D.4 in appendix D.6.

With larger average amplitudes the separation cut values are shifted to earlier times. On average, the early peaks in the FADC signal pulses are larger than delayed signal peaks due to the decrease of the density of delayed particles. The late peaks or late particle arrival times are suppressed when being unfolded with a larger average MIP detector response. Hence, the mean values and the quantiles of the distributions shift towards lower values. Unfolding the FADC signal pulses with a smaller average MIP detector response the separation cut values are shifted to higher values. The small signal peaks at later arrival times receive a higher weight, which increases the tails of the particle arrival time distributions. Thus, the separation cut values are shifted to higher values. Except for the values of the 25 %-quantiles, the muon purities are nearly unaffected by a change of the size of the average MIP detector response.

As shown above, the difference in the amplitude of the average MIP detector response is in the order of 10 %. Therefore, the systematic deviations of the separation cut values and the muon purities obtained from the unfolding using the average MIP detector response with 90 % and 110 % of the original amplitude will be used as contribution to

the overall systematic error. For each value of the separation cut and the muon purity the largest of both deviations will be added quadratically to the overall systematic error.

9.2.3 Influence of the correction to the shower core arrival time

In chapter 8 the reconstructed shower core arrival time has been compared to the true shower core arrival time of simulated air showers. A systematic deviation has been observed. The systematic deviation occurs since the reconstruction algorithm has been optimized for observables other than the arrival time of the shower core. In chapter 8 the correction of this systematic deviation has been described. It corresponds to the parameterization of the systematic deviation between the reconstructed shower core arrival time and the true simulated arrival time of the shower core. However, the difference between the reconstructed shower core arrival time and the true shower core arrival time may be smaller or larger for real air showers. To estimate the influence of the shower arrival time on the separation cut values, the analysis has also been performed without the correction on the shower core arrival time. The results are compared to the analysis with the correction. In the left part of figure 9.16 the difference of the separation cut values calculated from the 50 %-quantiles with correction and without correction are shown as an example. In the right part of the same figure the systematic deviation of the muon purities p_μ is shown. The systematic deviations of the values calculated with the 25 %-quantiles, 75 %-quantiles and the mean values are identical, thus they are not shown explicitly. The systematic deviation shows the expected behavior of a shift of the arrival times to smaller values if the correction to the shower core arrival time is not applied. The correction is a function of $\log_{10}(N_e)$ and is in the order of 10 ns.
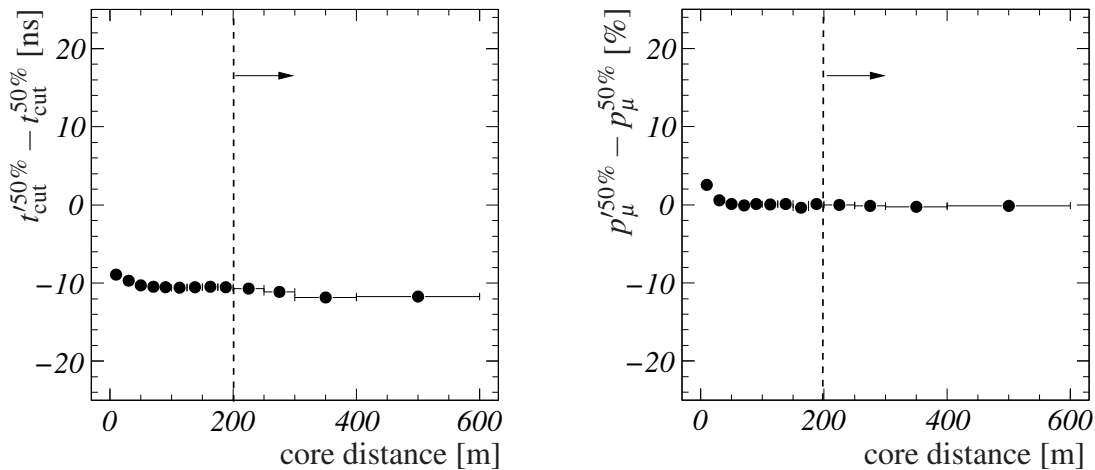
Figure 9.16: *Left:* Difference of the separation cut values without the correction to the shower core arrival time and the separation cut values obtained with correction. *Right:* Difference of the muon purities without the correction to the shower core arrival time and the muon purities obtained with correction. The dashed lines represent the core distance above which a separation of electrons and muons according to their arrival times becomes feasible.

Thus, the systematic deviation corresponds to 10 ns as well. The systematic deviation is close to constant for all core distances since showers with different $\log_{10}(N_e)$ are averaged in each core distance bin.

The studies of the shower core arrival time with simulated air showers show that a correction of the shower core arrival time is necessary. However, the precision of this correction when applied to real air showers is unknown. To give a conservative estimate for the systematic error of the correction, the total magnitude of the effect of the correction on the separation cut values and muon purities is used as their uncertainties. It will be added quadratically to the overall systematic error.

9.2.4 Influence of the correction to the reconstructed position of the discriminator threshold transition

Chapter 8 also describes the correction to the reconstructed position of the discriminator threshold transition within the individual FADC signal pulses. This correction corresponds to the parameterization of the pulse height dependent deviation between the simulated and reconstructed position of the threshold transition. For this simulation a FADC module has been emulated with characteristics extracted from the data of a real FADC module. The average MIP detector response has been used as true continuous detector signal for the simulation. Different signal shapes have not been simulated. The characteristics of the individual FADC modules could possibly be different from the emulated FADC module. Furthermore, the response of the modules could be in general different for different signal shapes. Therefore, the correction applied to the reconstructed position of the threshold transition could be incorrect. In order to study the impact on the separation cut values and the muon purities, the arrival time distributions are reconstructed without the correction to the reconstructed point of threshold transition. From these particle arrival time distributions the separation cut values and muon purities are calculated as well. The systematic deviation of these values from the values with the correction are shown in figure 9.17 for the values calculated using the 50 %-quantiles. The deviation is large at small core distances. This is due to the pulse height dependence of the correction. The correction is large for large pulse heights, which are predominantly measured close to the shower core. The same systematic difference is seen for the values calculated from the 25 %-quantiles, the 75 %-quantiles and the mean values.

The study of the performance of the algorithm for the reconstruction of the position of the discriminator threshold transition shows that a correction of the reconstructed position of the threshold transition is necessary. The correction has been found by a simulation of the FADC module. However, the characteristics of the real FADC modules may differ from the simulation and the precision of the correction is thus unknown. To give a conservative estimate for the systematic error of the correction, the total magnitude of the effect of the correction on the separation cut values and muon purities is used as their uncertainties. It will be added quadratically to the overall systematic error.
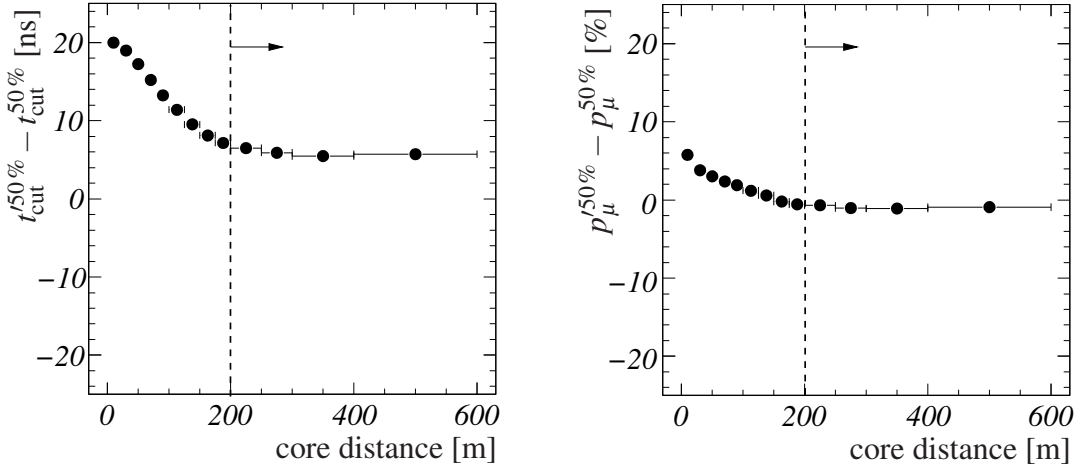
Figure 9.17: *Left:* Difference of the separation cut values determined without the correction to the reconstructed position of the threshold transition and the separation cut values obtained with the correction. *Right:* Difference of the muon purities without the correction to the reconstructed position of the threshold transition and the muon purities obtained with correction. The dashed lines represent the core distance above which a separation of electrons and muons according to their arrival times becomes feasible.

9.2.5 Overall systematic error

In the previous sections, the contributions to the systematic error of the separation cut values and muon purities have been studied. The uncertainty on the shower core position introduces a bias of the separation cut values and muon purities in a certain direction. The precision of the core position is known to be limited. In this work the air showers are averaged over the shower size N_e. The corresponding average resolution of the shower core position with the Grande reconstruction amounts to $\sigma \approx 8\,\text{m}$. Therefore, the systematic deviation has been calculated for the corresponding shower core position smearing. The result has been used to correct the values for the separation cut and the muon purities.

The other contributions to the systematic error are uncorrelated and are thus added quadratically and will be presented as a systematic error band of the separation cut values $t_{\text{cut}}(R)$ and muon purities $p_\mu(R)$. In the following σ_{sys} will refer to the overall systematic error. It is calculated as:

$$\sigma_{\text{sys}} = \sqrt{\sum_i (\sigma_{\text{sys}}^i)^2}. \tag{9.13}$$

The σ_{sys}^i are the systematic contributions from the individual sources of uncertainties discussed above. In tables D.11 and D.12 in appendix D.7 the resulting values for the separation cut values and the muon purities are listed together with their statistical and systematic errors. In figure 9.18 and 9.19 the resulting separation cut values and muon purities are depicted together with the systematic error band.
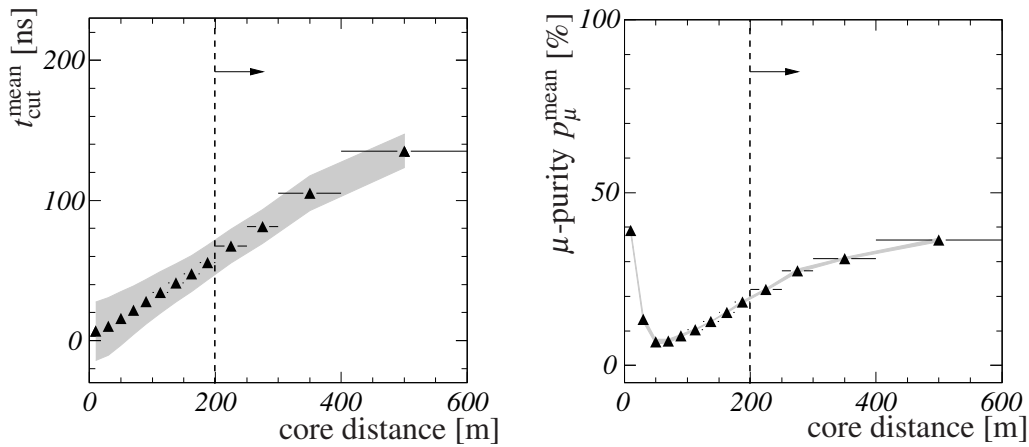
Figure 9.18: Separation cut values and muon purities with the systematic uncertainties repre-
sented by the error bands. The separation cut values and muon purities have been
calculated from the mean values of the particle arrival time distributions. The
dashed lines represent the core distance above which a separation of electrons
and muons according to their arrival times becomes feasible.

The systematic studies have shown that the separation cut values and muon purities
determined with the 25 %-quantiles of the particle arrival time distributions are sensitive
to the uncertainties in the shower core position and the size of the average MIP detector
response. The values calculated from the 75 %-quantiles have been found to be sensitive
to the smearing of the shower core position. The impact of the amplitude of the average
MIP detector response on the values calculated from the 75 %-quantiles is comparable
to the impact on the values calculated with the other quantiles or the mean value. The
values calculated from the 50 %-quantiles and the mean values of the distributions show
a small dependence on the uncertainties studied.

The muons which originate from decays of pions and kaons produced by primary hadrons
are more energetic and have a correspondingly earlier arrival time than muons produced
in a later stage of the shower development. In order to be sensitive to the muons pro-
duced in the first hadronic interactions, the use of lower separation cut values from the
25 %, 50 %-quantiles or the mean value is favored [Ost06]. Due to the smaller depen-
dence on systematic uncertainties like the core position resolution, the values corre-
sponding to the 50 %-quantiles (medians) or the mean values of the particle arrival time
distributions represent robust values of the separation cuts and muon purities. Either of
these two definitions of the separation cut value is therefore favored for the reconstruc-
tion of the muon content of particles measured by a time resolving detector.
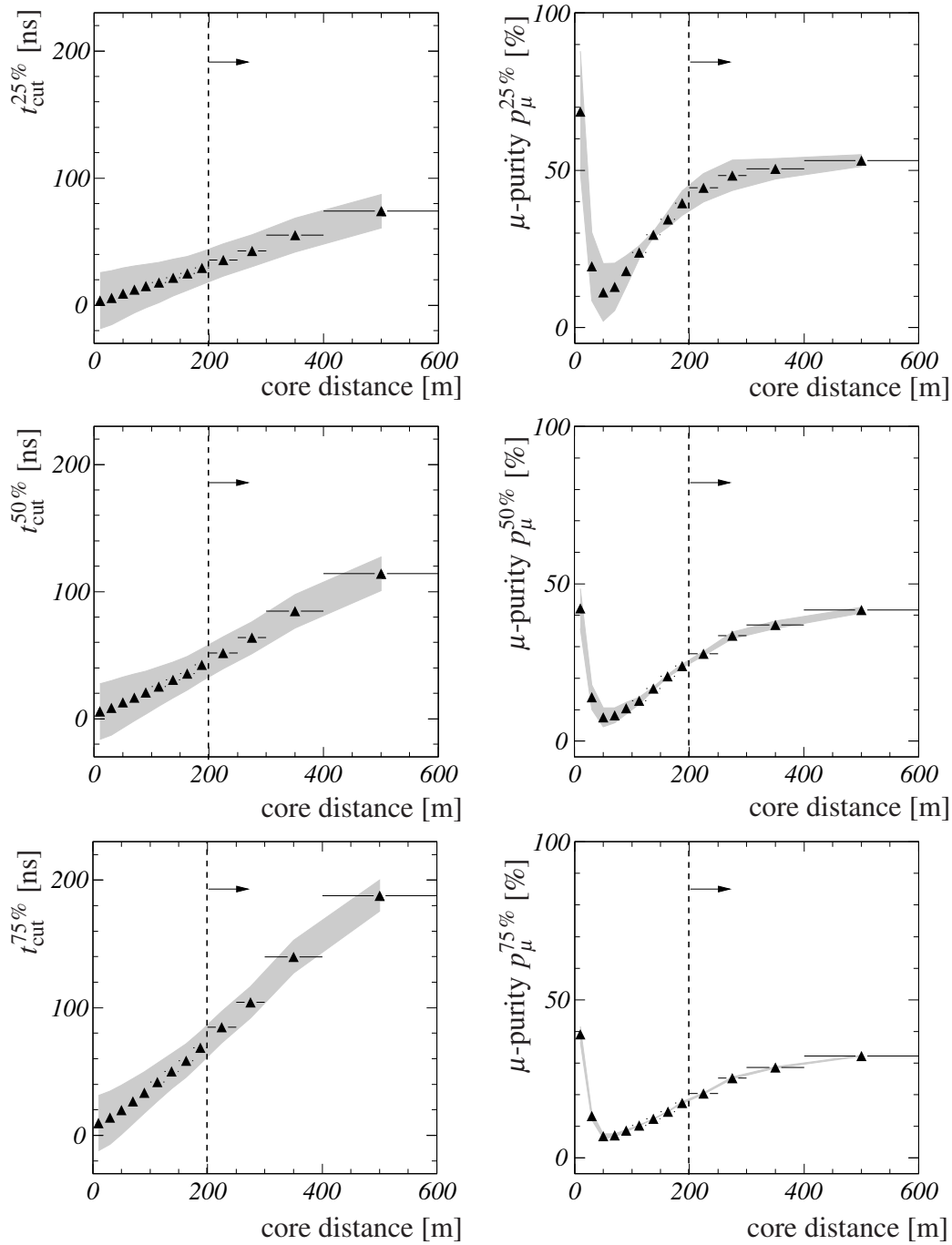
Figure 9.19: Separation cut values and muon purities calculated from different quantiles with the systematic uncertainties represented by the error bands. From top to bottom the separation cut values and muon purities are calculated from the 25 %-, 50 %- and 75 %-quantiles of the particle arrival time distributions. The dashed lines represent the core distance above which a separation of electrons and muons according to their arrival times becomes feasible.

9.3 Summary

In this chapter the particle arrival time distributions have been used to determine a cut on the particle arrival times relative to the arrival time of the shower core in order to distinguish muons from electrons at the observation level. The mean values of the arrival time distributions have been used to study the time profile of the electromagnetic and muonic shower fronts. It is found that for core distances larger than $R = 200\,\text{m}$ muons arrive in average earlier than electrons. The difference in the arrival times of muons and electrons increases with the core distance. The earlier mean arrival time of muons allows to estimate the number of muons measured by a time resolving detector if a suitable cut t_{cut} is placed on the particle arrival times. Particles arriving earlier than a separation cut value t_{cut} are considered muons. Due to the large spread of the particle arrival time distributions, electrons may also arrive earlier. To account for this contamination, the purity of the estimated number of muons has been determined. The purity corresponds to the ratio of the number of muons to the total number of particles arriving with $t < t_{\text{cut}}$. The number of muons and the total number of particles have been determined by applying the separation cut to the arrival time distributions of muons and electrons and summing the number of unfolded particles with $t < t_{\text{cut}}$.

The separation cut value has been determined as the average of the mean values of the muon and electron arrival time distributions. Apart from this definition of the separation cut value, also the mean value of the 25 %-, 50 %- and 75 %-quantiles of the arrival time distributions have been used as additional definitions of the separation cut values.

The attempts to describe the particle arrival time distributions analytically by fitting a Γ-probability density function and a Log-normal-function fail to describe the tails of the distributions. Furthermore, a fluctuation of the fit results depending on the fit range has been observed. Therefore, the separation cut values resulting from the fit results are considered not robust enough to be used to separate muons and electrons.

It has been found that the separation cut values and the muon purity do not depend on the zenith angle for zenith angles $\vartheta < 30°$. A dependence on the primary energy of the incident primary particle has not been observed.

In the second part of the chapter, systematic uncertainties of the separation cut values and the muon purity have been studied. Different values for a shower core position smearing have been used to study the impact of the uncertainty of the shower core location on the separation cut values and the muon purities. It turns out that the values calculated from the mean values and the 50 %-quantiles of the distributions are stable with respect to the shower core position resolution.

The possible effect of a wrong description of the average MIP detector response has been studied by unfolding the FADC signal pulses using modified average MIP detector responses. The response amplitudes have been scaled in the range 50 %-150 % of the original value to account for the uncertainty in the height of the average MIP detector response. This uncertainty is introduced by the uncertainty in the choice of the minimum

core distance for detector stations providing the FADC signal pulses which are used to determine the average MIP detector response. This uncertainty has the largest impact on the values calculated from the 25 %-quantiles of the distributions.

The dominating systematic uncertainties are due to the corrections to the calculation of the particle arrival times with respect to the shower plane. The correction to the arrival time of the shower core shifts the separation cut values on average by 10 ns to larger values. The correction to the reconstructed time of the threshold transition within the FADC signal pulses shifts the separation cut values by 6 ns to lower values in the core distance range of interest. This has been conservatively added to a total systematic error of about 12 ns on average.

The values of the separation cut have been corrected for the systematic errors introduced by the finite shower core position resolution. The corrected values are presented together with the combination of the other systematic uncertainties in figures 9.18 and 9.19.

Summary

In this thesis the arrival time distributions of the electromagnetic and the muonic component of extensive air showers have been studied for large showers measured by the KASCADE-Grande experiment. The data analyzed have been acquired by a Flash-ADC based data acquisition system connected to the e/γ- and μ-detectors of eight detector stations of the KASCADE array.

The need for a common reference time for the particle arrival times measured by the different detector stations requires a synchronization of the KASCADE array and the Grande array. The synchronization is achieved by determining the time difference between the arrival time of the shower core measured by detector stations of both detector arrays.

The particle arrival times are extracted from the FADC signal pulses using an unfolding algorithm. For the construction of the response matrix the average detector response of a single particle transition is determined. This is done by averaging FADC signal pulses provided by detector stations with a radial distance exceeding a minimum distance to the shower core above which the particle density is lower than one per m^2. This minimum distance is determined by investigating the spectra of measured energy deposits for several intervals of the distance to the shower core position.

The data analyzed consist of extensive air showers measured by the Grande detector array in the time period from January 2005 to Febuary 2006. Only showers with a zenith angle $\vartheta < 30°$ are included in the analysis to assure a high quality of the reconstructed shower core arrival time. Futhermore, only air showers with a minimum extension are used to assure full trigger and reconstruction efficiency of the Grande detector array.

The particle arrival times unfolded from the FADC signal pulses are aligned relative to the shower front arrival times measured by the KASCADE detectors which provided

the corresponding FADC signal pulses. The time difference between the shower front arrival times measured by the KASCADE detectors and the arrival time of the shower core is calculated in order to determine the particle arrival times with respect to the shower plane. A correction to the reconstructed arrival time of the shower core is extracted using air showers simulated with the air shower simulation program CORSIKA and processed by the detector simulation CRES.

The arrival times relative to the shower plane are used to determine the particle arrival time distributions separately for electrons and muons for several intervals of the core distance. These particle arrival time distributions are used to study the time profile of the electromagnetic and muonic shower disk. It is found that an arrival time difference of both shower components is observable at core distances $R > 200\,\mathrm{m}$ and increases with the distance to the shower core position.

The particle arrival time distributions are used to determine a cut on the particle arrival times in order to separate muons from electrons. This separation cut is calculated for several intervals of the distance to the shower core using four different methods, employing the mean values, 25 %-quantiles, 50 %-quantiles and the 75 %-quantiles of the particle arrival time distributions. Due to the large spread of the arrival time distributions for electrons and muons, a 100 % separation is not possible. The purity of the extracted muon number, calculated from the sum of particles with an arrival time less than the separation cut value, is calculated for each value of the separation cut. If the muon number is estimated with the help of a time resolving detector using the above cut on the particle arrival times, this purity factor has to be applied as a correction factor in order to statistically cancel the contribution of the electromagnetic component.

The analysis is performed for three intervals of the zenith angle and the primary energy in order to study the dependence of the separation cut on the zenith angle and the primary energy. A zenith angle dependence is excluded for zenith angles $\vartheta < 30°$. Up to core distances of $R = 300\,\mathrm{m}$ no dependence on the primary energy has been observed. For larger distances no conclusion can be drawn due to the limited statistics at large distances for low primary energies.

The systematic contributions to the errors of the separation cut values and the muon purity are studied. The analysis is repeated with different values for the smearing applied to the shower core position and with modified average minimum ionizing particle detector responses, which are important inputs for the unfolding algorithm. The dominating systematic uncertainties are introduced by the correction to the shower core arrival time and the correction to the alignment of the unfolded particle arrival times relative to the time measured by the KASCADE array detectors. Due to their smaller dependence on systematic uncertainties, the separation cut values determined from the 50 %-quantiles or alternatively from the mean values of the particle arrival time distributions are favored for an application on data.

The main conclusions of the analysis are:

- Electrons and muons in extensive air showers have different arrival times at ground level. Above a distance to the shower core of $R = 200\,$m muons arrive on average earlier than electrons. The difference in the arrival time increases with the distance from the shower core.

- The thicknesses of the electromagnetic and muonic shower disks have been determined. Up to distances of $R = 200\,$m the thickness of the muonic shower disk is on average 10 ns larger than the thickness of the electromagnetic shower disk. The difference in the thickness decreases with the distance from the shower core. For core distances larger than $R = 400\,$m, the thickness of the muonic shower disk is approximately 5 ns smaller than the thickness of the electromagnetic shower disk.

- The Γ-probability density function is not applicable for an analytical description of the particle arrival time distribution.

- Electrons and muons can be separated according to the difference in their arrival times at observation level.

The separation cut values calculated from the mean values and the 50 %-quantiles of the particle arrival time distributions and the corresponding purities of the muon number are summarized in the following table:

distance [m]	$t_{\mathrm{cut}}^{\mathrm{mean}}$ [ns]	p_{μ}^{mean} [%]	$t_{\mathrm{cut}}^{50\%}$ [ns]	$p_{\mu}^{50\%}$ [%]
200-250	$67.5 \pm 0.1 \pm 12.0$	$21.9 \pm 0.1 \pm 0.4$	$51.9 \pm 0.1 \pm 12.6$	$27.8 \pm 0.2 \pm 0.7$
250-300	$81.4 \pm 0.2 \pm 12.0$	$27.4 \pm 0.2 \pm 0.5$	$63.7 \pm 0.2 \pm 12.7$	$33.6 \pm 0.3 \pm 1.1$
300-400	$105.2 \pm 0.2 \pm 12.4$	$30.9 \pm 0.3 \pm 0.3$	$84.5 \pm 0.2 \pm 13.1$	$37.0 \pm 0.3 \pm 1.2$
> 400	$135.3 \pm 0.6 \pm 12.0$	$36.3 \pm 0.8 \pm 0.5$	$114.0 \pm 0.6 \pm 13.1$	$41.6 \pm 0.8 \pm 0.9$

The values are listed with their statistical and systematic errors. The separation cut values are only shown for core distances $R > 200\,$m, for which a separation of electrons and muons according to their arrival times becomes feasible.

Extraction of the offset values from the offset distributions

In chapter 6 the determination of the time offset between the Grande array and the e/γ-respectively μ-detector of the KASCADE array has been described. Due to inclined air showers used for the computation of the corresponding offsets, distributions of offset values are measured rather than a single constant value. However, the center of the observed distribution corresponds to the offset in demand. A determination of the offset by calculating the arithmetic mean of the distribution would be biased by outliers caused by background entries from uncorrelated muons. Therefore, a Gaussian distribution was fitted to the distribution to extract the offset as the mean of this Gaussian. Figure A.1 shows all offset distributions together with the fitted Gaussians and the corresponding fit values.
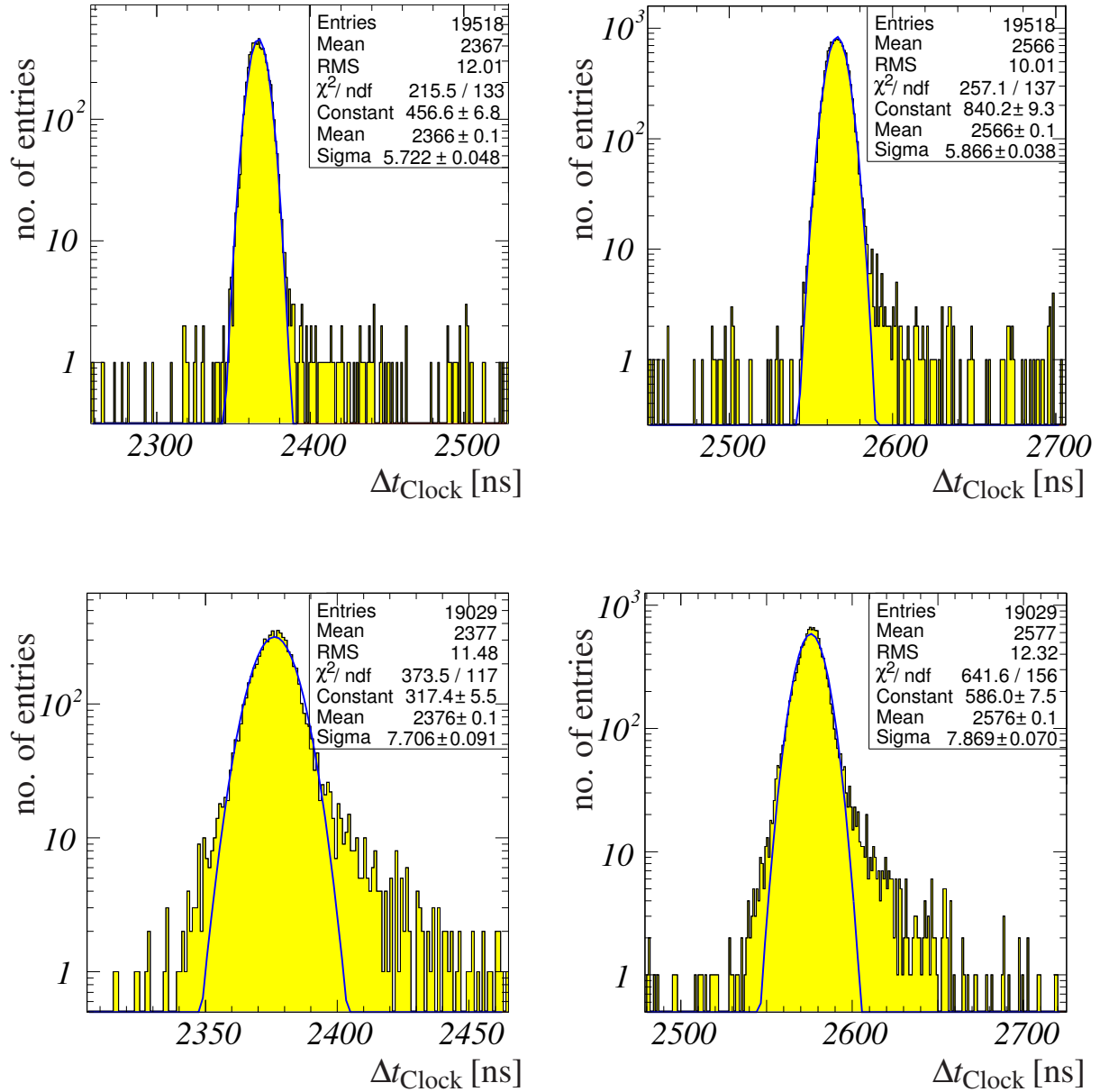
Figure A.1: Determination of the offset values by a Gaussian fit to the offset distributions. *Upper left:* Lower distribution of the offset between the e/γ-detector and Grande. *Upper right:* Upper offset distribution for the e/γ-detector. *Lower left:* Lower offset distribution for the μ-detector. *Lower right:* Upper offset distribution for the μ-detector.

Determination of the number of iterations for the unfolding algorithm

Chapter 7 describes the determination of the number of iterations to be used for the unfolding of FADC signal pulses. The variation of the characteristics of an overall arrival time distribution for different number of iterations were studied. These characteristics are described in chapter 7. In chapter 7 only the results for the e/γ-distributions have been shown. In figure B.1 the variation of these characteristics of the overall arrival time distributions determined from FADC signal pulses of the μ-detector are shown. The variations for different numbers of iterations are even smaller than the corresponding variations of the characteristics of the e/γ-distributions. Therefore, also for the unfolding of FADC signal pulses from the μ-detector $m = 600$ iterations is used.
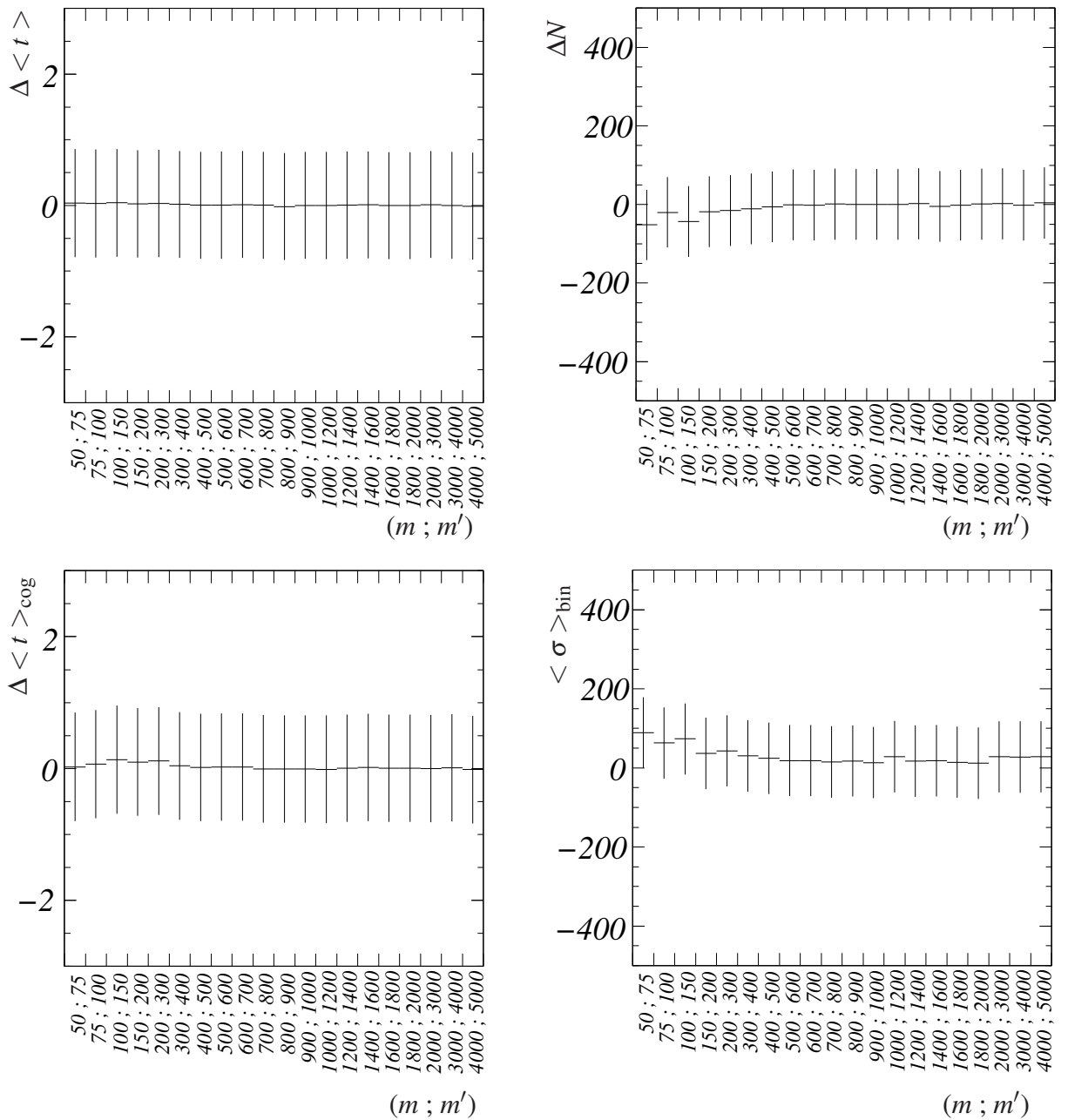
Figure B.1: Comparison of characteristic quantities of the overall muon arrival time distributions unfolded with a different number of iterations. The graphs show the case for distributions obtained from FADC signal pulses of the μ-detector. The expression $(m ; m')$ refers to the pairs of the lower number of iterations m and the next higher number of iterations m'. See text for details. *Upper left:* Differences in the mean of the distributions. *Upper right:* Differences in the number of entries. *Lower left:* Differences of the center of gravity of the distributions. *Lower right:* Average bin fluctuation between the distributions. Note that the errors are strongly correlated since always the same sample is used.

Arrival time distributions of the electromagnetic and muonic shower components

In chapter 8 the transformation of the particle arrival times unfolded from the individual FADC signal pulses into particle arrival times with respect to the arrival time of the shower core or shower plane has been described. The particle arrival times obtained are used to extract particle arrival time distributions for 13 intervals of the distance to the shower core R, separately for electrons and muons. The particle arrival time distributions for the electromagnetic component are corrected for the contribution of muons. In this appendix the 13 corrected electron as well as the 13 muon arrival time distributions are shown.

Figures C.1-C.3 show the arrival time distributions of electrons for the 13 intervals of the core distance. Figures C.4-C.6 show the corresponding 13 muon arrival time distributions. The distributions for the core distance bin $R = (0 - 20)$ m contain less particles than the distributions of the next larger distance bin $R = (20 - 40)$ m. This is caused by the cut on the pulse height of the FADC signal pulses to exclude distorted FADC signal pulses from the analysis. This cut affects mainly FADC pulses measured by stations close to the shower core. The statistics in the other distributions decreases with increasing core distance as expected. In distributions for which the width of the core distance interval is enlarged, this decrease in statistics is reduced.
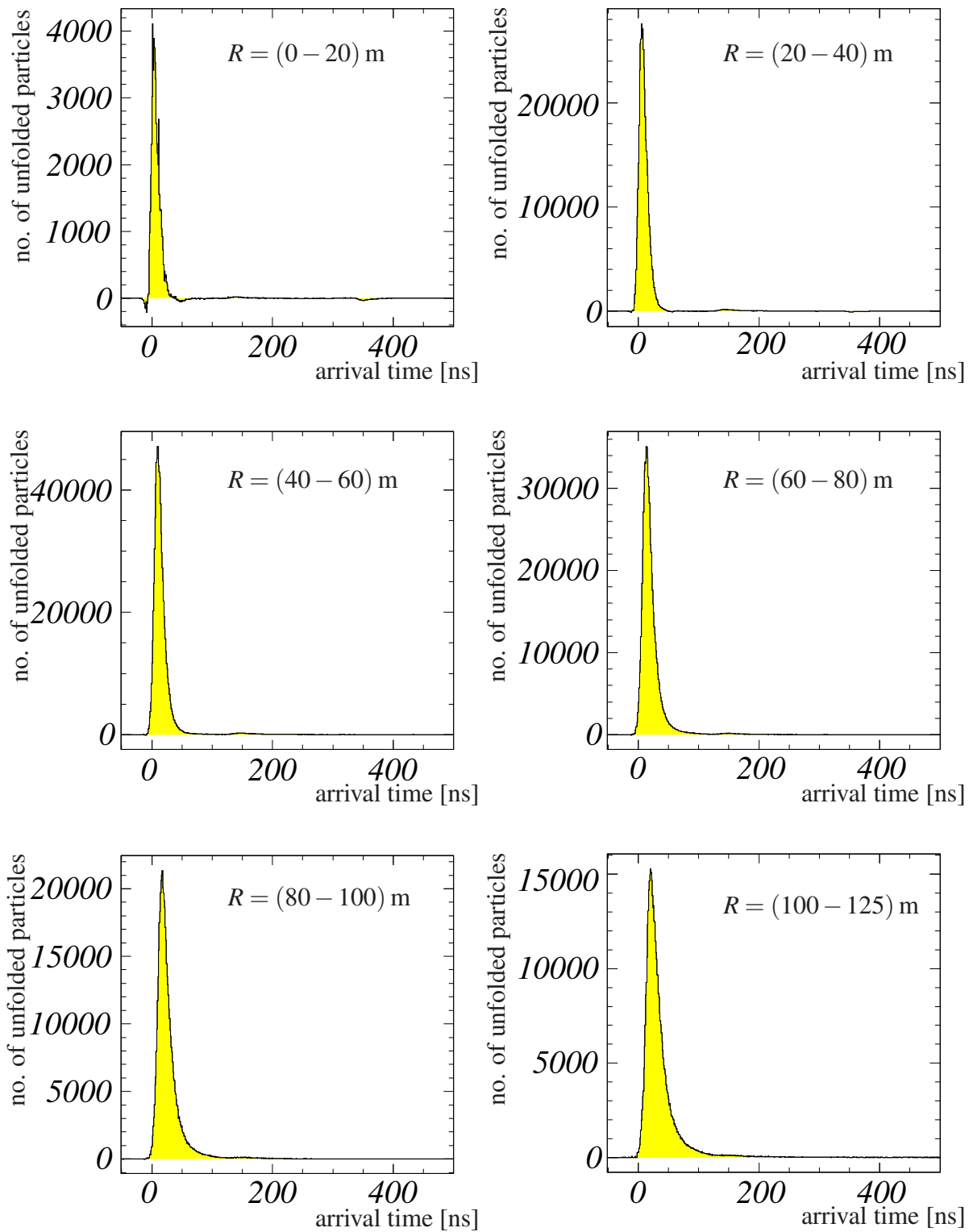
Figure C.1: Electron arrival time distributions for various intervals of the distance from the shower core R in the range from $R = 0\,\mathrm{m}$ to $R = 125\,\mathrm{m}$.
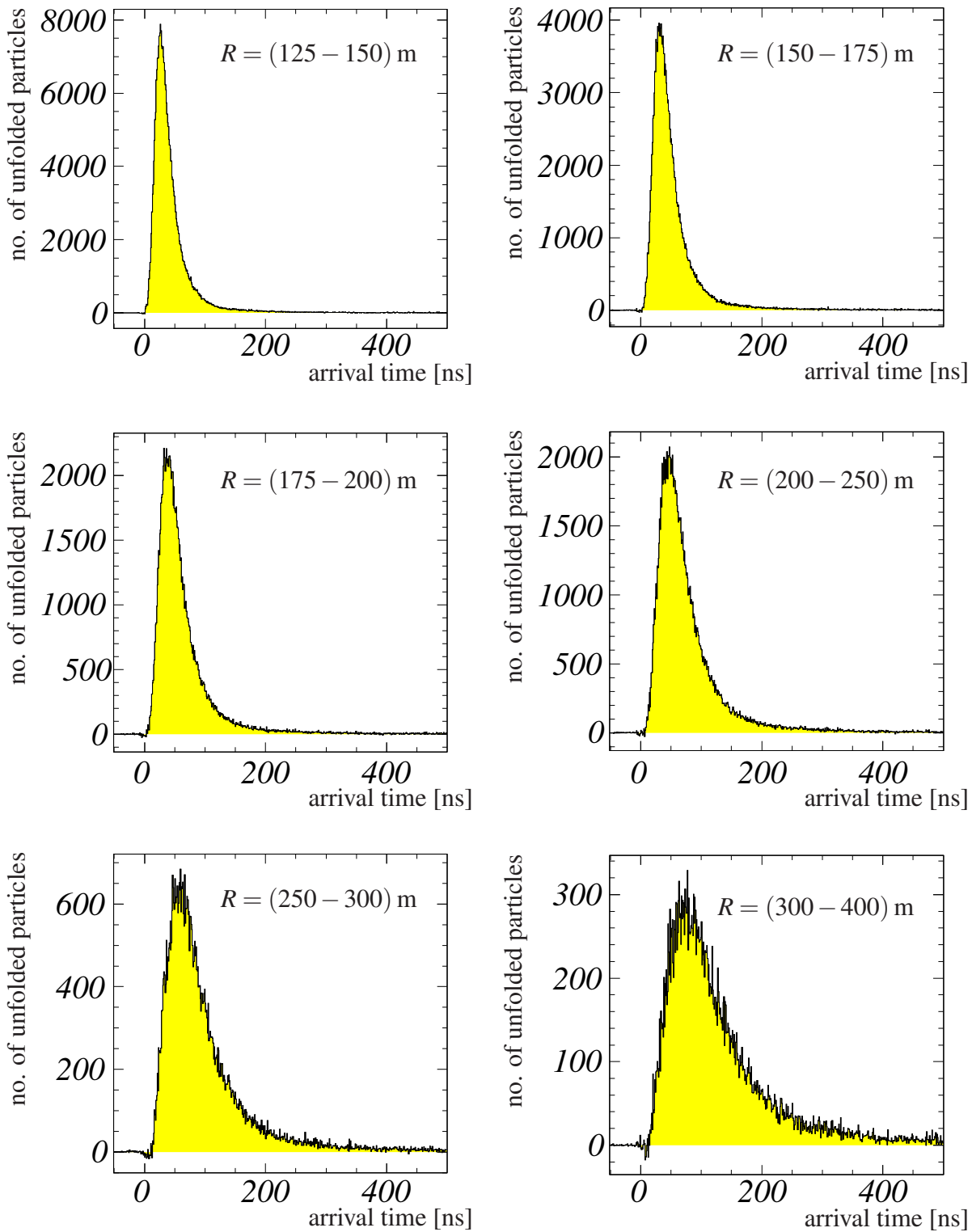
Figure C.2: Electron arrival time distributions for various intervals of the distance from the shower core R in the range from $R = 125$ m to $R = 400$ m.
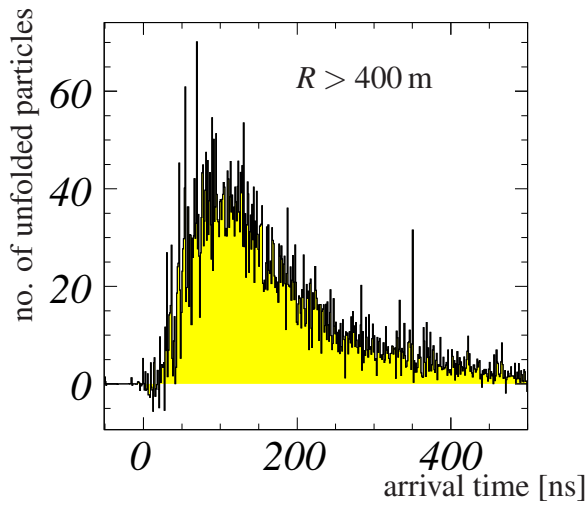
Figure C.3: Electron arrival time distributions for core distances $R > 400$ m.
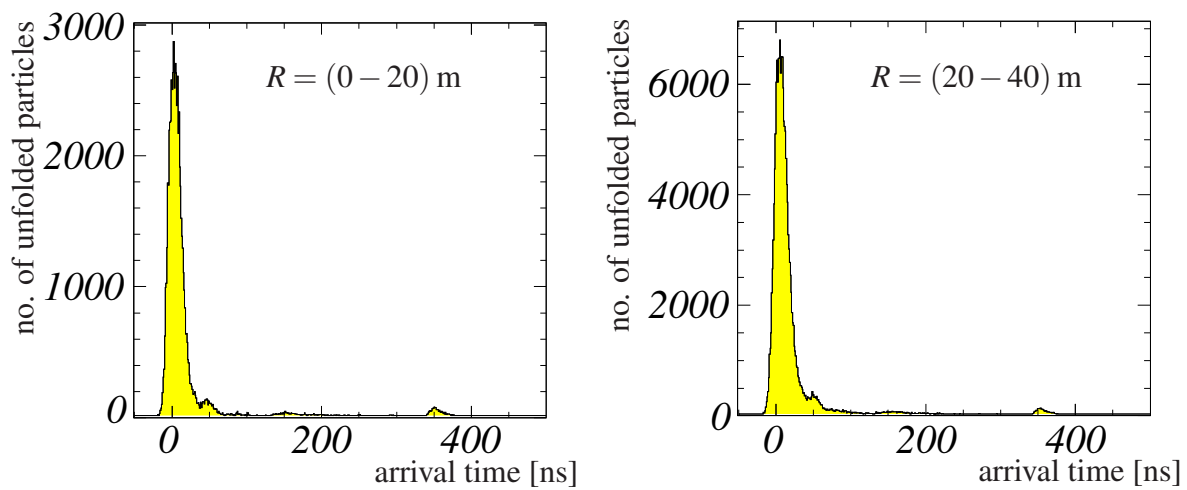
Figure C.4: Muon arrival time distributions for various intervals of the distance from the shower core R in the range from $R = 0$ m to $R = 40$ m.
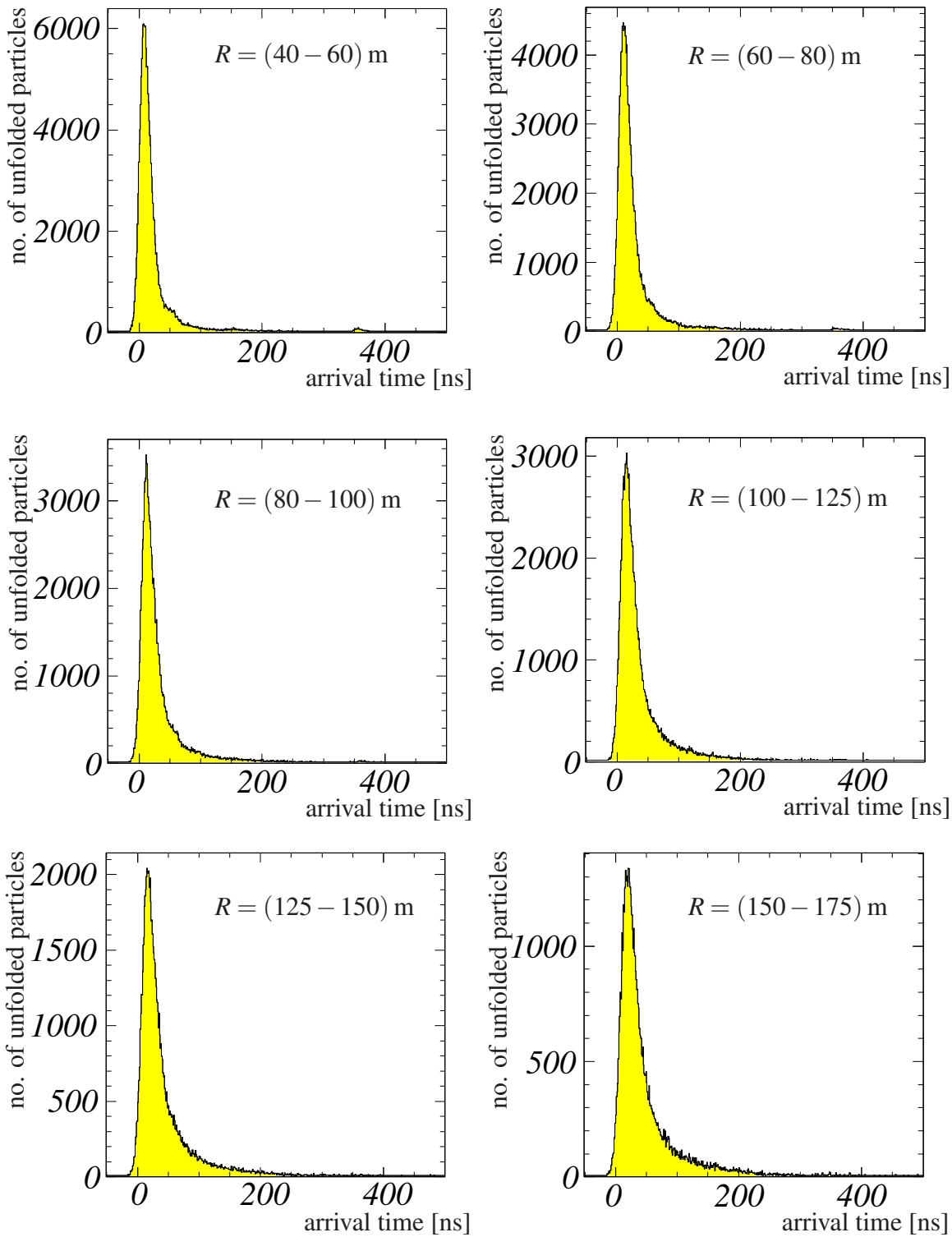
Figure C.5: Muon arrival time distributions for various intervals of the distance from the shower core R in the range from $R = 40\,\text{m}$ to $R = 175\,\text{m}$.
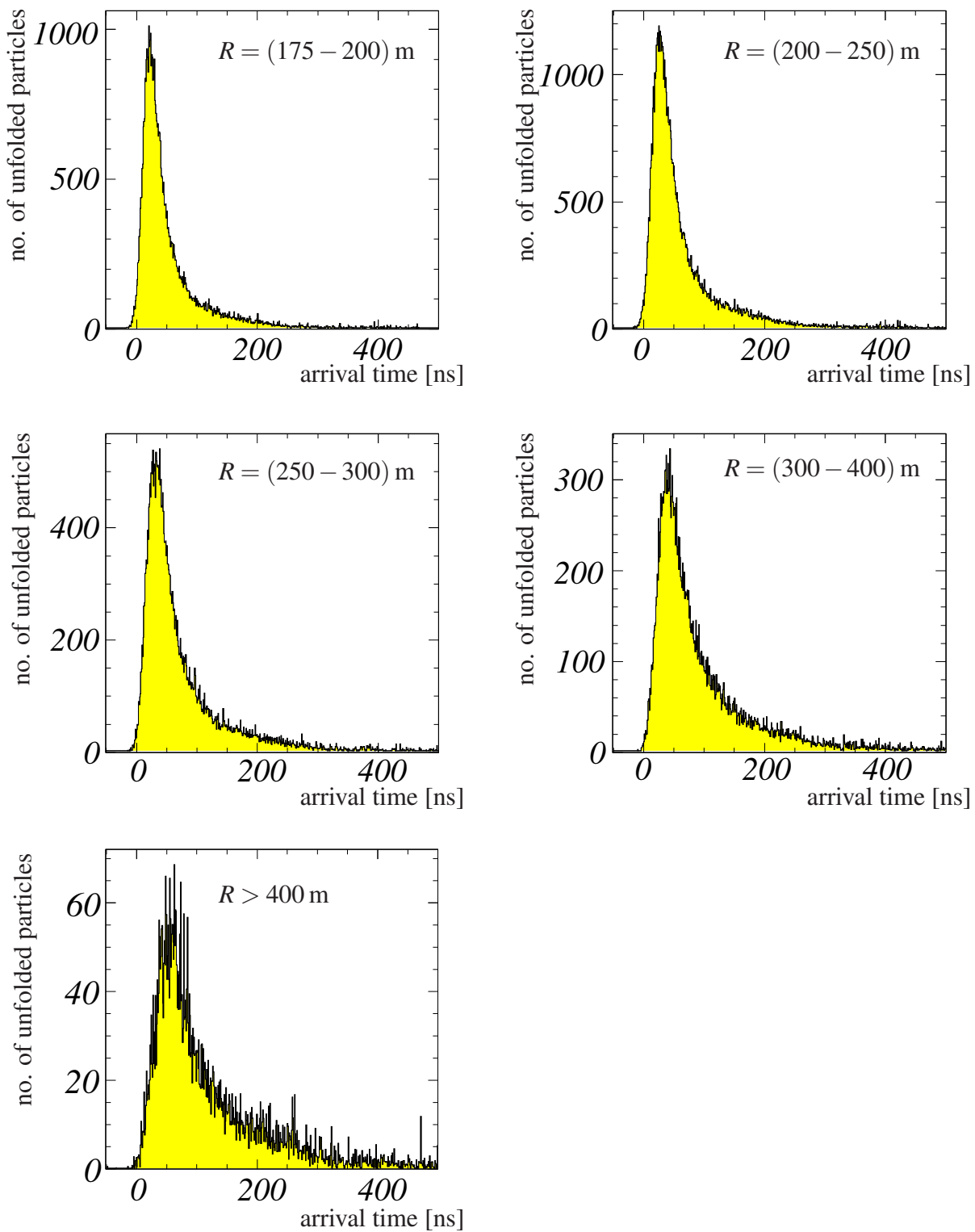
Figure C.6: Muon arrival time distributions for various intervals of the distance from the shower core R for distances $R > 175$ m.

Results for the separation cut values, muon purities and systematic studies

This appendix contains the tables of the values of the separation cuts and the corresponding muon purities calculated by the methods described in chapter 9.

Appendices D.1 and D.2 provide lists of separation cut values and muon purities, which have been calculated using the mean values of the particle arrival time distributions and the 25 %-, 50 %-, and 75 %-quantiles.

In appendix D.3 the fit results of the Γ-function fits to the particle arrival time distributions are shown together with the resulting values for the separation cut values and muon purities. Appendix D.3 contains the same values, but for the Log-normal-function fits to the particle arrival time distributions.

In section D.5 the dependency of the results on the resolution of the shower core position is shown. Appendix D.6 depicts the influence of the size of the average MIP detector response on the results.

Appendix D.7 lists the results for the separation cut values and muon purities after the correction of the systematic errors introduced by the finite shower core position resolution showing statistical and systematic errors.

D.1 Separation cut values determined with the mean values

distance [m]	$\langle t \rangle_{e/\gamma}$ [ns]	$\sigma_{e/\gamma}$ [ns]	$\langle t \rangle_{\mu}$ [ns]	σ_{μ} [ns]	$t_{\text{cut}}^{\text{mean}}$ [ns]	μ-purity [%]
0-20	7.0 ± 0.1	8.36 ± 0.03	6.9 ± 0.3	12.14 ± 0.03	7.0 ± 0.2	36.8 ± 0.2
20-40	9.24 ± 0.03	7.963 ± 0.008	11.53 ± 0.05	15.44 ± 0.03	10.39 ± 0.03	13.89 ± 0.06
40-60	13.970 ± 0.005	10.716 ± 0.008	17.49 ± 0.02	20.08 ± 0.03	15.73 ± 0.01	7.69 ± 0.03
60-80	20.00 ± 0.01	16.12 ± 0.01	22.87 ± 0.02	24.99 ± 0.05	21.43 ± 0.01	7.58 ± 0.04
80-100	26.51 ± 0.02	21.06 ± 0.02	28.36 ± 0.04	30.93 ± 0.07	27.43 ± 0.02	8.92 ± 0.05
100-125	33.68 ± 0.03	25.38 ± 0.03	34.30 ± 0.05	36.27 ± 0.08	33.99 ± 0.03	10.87 ± 0.05
125-150	41.91 ± 0.04	30.07 ± 0.04	39.68 ± 0.08	41.1 ± 0.1	40.79 ± 0.05	13.36 ± 0.07
150-175	50.11 ± 0.06	34.63 ± 0.06	45.1 ± 0.1	45.7 ± 0.1	47.63 ± 0.07	16.1 ± 0.1
175-200	59.85 ± 0.09	40.65 ± 0.08	51.3 ± 0.2	50.5 ± 0.2	55.60 ± 0.09	19.2 ± 0.1
200-250	73.4 ± 0.1	48.46 ± 0.09	60.5 ± 0.2	56.5 ± 0.2	67.0 ± 0.1	22.9 ± 0.1
250-300	92.1 ± 0.2	59.0 ± 0.2	70.5 ± 0.3	63.3 ± 0.2	81.3 ± 0.2	28.4 ± 0.2
300-400	119.9 ± 0.3	73.6 ± 0.3	89.6 ± 0.4	74.0 ± 0.3	104.7 ± 0.2	31.9 ± 0.3
>400	158.2 ± 0.8	90.4 ± 0.8	112.6 ± 0.9	84.7 ± 0.8	135.4 ± 0.6	37.3 ± 0.7

Table D.1: Mean arrival time of electrons and muons and the separation cut values with the corresponding muon purity calculated from the mean values of the arrival time distributions. Only the statistical errors are shown.

D.2 Separation cut values determined with the quantiles

distance range [m]	$t_{e/\gamma}^{25\%}$ [ns]	$t_{\mu}^{25\%}$ [ns]	$t_{\text{cut}}^{25\%}$ [ns]	μ-purity [%]
0-20	2.9 ± 0.1	0.7 ± 0.3	1.8 ± 0.2	51.3 ± 0.4
20-40	4.85 ± 0.03	3.52 ± 0.05	4.18 ± 0.03	17.78 ± 0.1
40-60	8.400 ± 0.005	6.83 ± 0.02	7.61 ± 0.01	10.71 ± 0.07
60-80	11.98 ± 0.01	9.31 ± 0.02	10.64 ± 0.01	11.54 ± 0.08
80-100	15.75 ± 0.02	11.33 ± 0.04	13.54 ± 0.02	15.1 ± 0.1
100-125	19.96 ± 0.03	13.73 ± 0.05	16.85 ± 0.03	19.9 ± 0.1
125-150	25.09 ± 0.04	16.15 ± 0.08	20.62 ± 0.05	25.1 ± 0.2
150-175	30.08 ± 0.06	18.4 ± 0.1	24.23 ± 0.07	30.6 ± 0.2
175-200	35.75 ± 0.09	21.5 ± 0.2	28.62 ± 0.09	35.9 ± 0.3
200-250	43.5 ± 0.1	26.2 ± 0.2	34.8 ± 0.1	40.6 ± 0.3
250-300	53.9 ± 0.2	30.8 ± 0.3	42.3 ± 0.2	47.1 ± 0.4
300-400	69.3 ± 0.3	40.6 ± 0.4	55.0 ± 0.2	48.6 ± 0.5
> 400	93.7 ± 0.8	53.7 ± 0.9	73.7 ± 0.6	53 ± 1

Table D.2: Separation cut values and muon purity calculated from the 25 %-quantiles of the arrival time distributions. The values are listed with their statistical errors only.

distance range [m]	$t_{e/\gamma}^{50\%}$ [ns]	$t_{\mu}^{50\%}$ [ns]	$t_{\text{cut}}^{50\%}$ [ns]	μ-purity [%]
0-20	6.4 ± 0.1	7.2 ± 0.3	6.8 ± 0.2	36.8 ± 0.2
20-40	9.11 ± 0.03	10.22 ± 0.05	9.67 ± 0.03	14.15 ± 0.06
40-60	13.223 ± 0.005	14.15 ± 0.02	13.68 ± 0.01	8.02 ± 0.04
60-80	17.61 ± 0.01	17.56 ± 0.02	17.59 ± 0.01	8.16 ± 0.04
80-100	22.46 ± 0.02	20.63 ± 0.04	21.54 ± 0.02	9.96 ± 0.06
100-125	28.17 ± 0.03	24.33 ± 0.05	26.25 ± 0.03	12.28 ± 0.07
125-150	35.14 ± 0.04	27.79 ± 0.08	31.47 ± 0.05	15.70 ± 0.09
150-175	42.26 ± 0.06	31.3 ± 0.1	36.77 ± 0.07	19.6 ± 0.1
175-200	50.53 ± 0.09	36.0 ± 0.2	43.25 ± 0.09	23.0 ± 0.2
200-250	61.9 ± 0.1	42.9 ± 0.2	52.4 ± 0.1	27.1 ± 0.2
250-300	78.3 ± 0.2	50.2 ± 0.3	64.3 ± 0.2	33.3 ± 0.3
300-400	103.8 ± 0.3	66.0 ± 0.4	84.9 ± 0.2	36.3 ± 0.3
> 400	142.4 ± 0.8	85.4 ± 0.9	113.9 ± 0.6	41.4 ± 0.8

Table D.3: Separation cut values and muon purity calculated from the 50 %-quantiles of the arrival time distributions. The values are listed with their statistical errors only.

distance range [m]	$t_{e/\gamma}^{75\%}$ [ns]	$t_{\mu}^{75\%}$ [ns]	$t_{\text{cut}}^{75\%}$ [ns]	μ-purity [%]
0-20	11.4 ± 0.1	16.3 ± 0.3	13.8 ± 0.2	34.5 ± 0.2
20-40	14.76 ± 0.03	20.40 ± 0.05	17.58 ± 0.03	13.40 ± 0.05
40-60	19.656 ± 0.005	26.60 ± 0.02	23.13 ± 0.01	7.44 ± 0.03
60-80	25.73 ± 0.01	32.74 ± 0.02	29.24 ± 0.01	7.29 ± 0.03
80-100	32.87 ± 0.02	38.70 ± 0.04	35.79 ± 0.02	8.48 ± 0.04
100-125	41.24 ± 0.03	45.89 ± 0.05	43.57 ± 0.03	10.13 ± 0.05
125-150	51.29 ± 0.04	52.22 ± 0.08	51.76 ± 0.05	12.18 ± 0.07
150-175	61.55 ± 0.06	58.6 ± 0.1	60.06 ± 0.07	14.58 ± 0.09
175-200	73.78 ± 0.09	66.1 ± 0.2	69.93 ± 0.09	17.3 ± 0.1
200-250	91.4 ± 0.1	78.8 ± 0.2	85.1 ± 0.1	20.4 ± 0.1
250-300	117.6 ± 0.2	92.6 ± 0.3	105.1 ± 0.2	25.2 ± 0.2
300-400	158.5 ± 0.3	120.8 ± 0.4	139.6 ± 0.2	28.4 ± 0.2
> 400	219.7 ± 0.8	156.8 ± 0.9	188.3 ± 0.6	32.5 ± 0.6

Table D.4: Separation cut values and muon purity calculated from the 75 %-quantiles of the arrival time distributions. The values are listed with their statistical errors only.

D.3   Separation cut values determined with results from the Γ-function fit

distance [m]	χ^2/n.d.f.	a	b	c	θ [ns]	$t_{\min}^{\text{fit}}$	$t_{\max}^{\text{fit}}$
0-20	957.92 / 24	72 ± 24	3.0 ± 0.2	0.296 ± 0.008	993.5 ± 0.3	998	1013
20-40	342.58 / 12	3869 ± 898	1.8 ± 0.1	0.227 ± 0.009	997.6 ± 0.3	1000	1016
40-60	608.75 / 21	2023 ± 460	2.4 ± 0.1	0.232 ± 0.005	999.2 ± 0.3	1003	1028
60-80	361.42 / 19	1153 ± 252	2.4 ± 0.1	0.207 ± 0.004	1001.6 ± 0.3	1006	1029
80-100	314.02 / 21	1241 ± 244	1.9 ± 0.1	0.161 ± 0.004	1004.8 ± 0.3	1009	1034
100-125	221.30 / 21	1088 ± 243	1.7 ± 0.1	0.131 ± 0.004	1007.7 ± 0.4	1012	1037
125-150	130.39 / 31	389 ± 269	1.7 ± 0.3	0.101 ± 0.009	1010 ± 1	1015	1050
150-175	95.17 / 37	133 ± 61	1.7 ± 0.2	0.085 ± 0.004	1011 ± 1	1018	1059
175-200	115.17 / 52	46 ± 28	1.7 ± 0.2	0.070 ± 0.004	1012 ± 1	1021	1077
200-250	142.52 / 54	75 ± 60	1.4 ± 0.3	0.052 ± 0.005	1018 ± 2	1027	1085
250-300	297.75 / 111	9 ± 12	1.6 ± 0.4	0.038 ± 0.004	1015 ± 5	1029	1144
300-400	273.36 / 145	12 ± 20	1.1 ± 0.5	0.024 ± 0.004	1025 ± 10	1040	1189
>400	401.32 / 194	1 ± 2	1.2 ± 0.8	0.018 ± 0.005	1033 ± 16	1051	1211

Table D.5: Fit results of the Γ-function fit to the electron arrival time distributions. The errors are provided by the fit algorithm. The values $t_{\min}^{\text{fit}}$ and $t_{\max}^{\text{fit}}$ are the lower and upper limit of the fit range.

| distance [m]	χ^2/n.d.f.	a	b	c	θ [ns]	t_{min}^{fit}	t_{max}^{fit}
0-20	267.67 / 32	655 ± 222	1.4 ± 0.2	0.191 ± 0.007	995.8 ± 0.7	997	1029
20-40	673.94 / 43	2 ± 1	4.3 ± 0.3	0.235 ± 0.008	986.4 ± 0.6	997	1034
40-60	199.39 / 33	65 ± 30	2.7 ± 0.2	0.178 ± 0.006	992.8 ± 0.6	999	1036
60-80	118.31 / 27	117 ± 65	2.2 ± 0.2	0.149 ± 0.008	995.5 ± 0.8	1001	1032
80-100	150.02 / 25	284 ± 111	1.6 ± 0.2	0.122 ± 0.007	998.7 ± 0.7	1003	1032
100-125	78.94 / 24	132 ± 102	1.8 ± 0.3	0.12 ± 0.01	999 ± 1	1004	1032
125-150	106.21 / 36	72 ± 36	1.8 ± 0.2	0.106 ± 0.005	999.4 ± 0.9	1005	1045
150-175	76.67 / 39	26 ± 24	2.0 ± 0.4	0.100 ± 0.008	999 ± 2	1006	1049
175-200	64.08 / 35	52 ± 46	1.5 ± 0.4	0.08 ± 0.01	1003 ± 2	1009	1048
200-250	95.44 / 48	35 ± 24	1.6 ± 0.3	0.074 ± 0.005	1004 ± 2	1011	1063
250-300	68.39 / 58	20 ± 19	1.5 ± 0.3	0.060 ± 0.006	1006 ± 3	1014	1076
300-400	69.16 / 51	34 ± 29	1.0 ± 0.3	0.044 ± 0.007	1015 ± 3	1021	1076
>400	206.28 / 145	3 ± 2	1.0 ± 0.2	0.028 ± 0.003	1014 ± 3	1032	1116

Table D.6: Fit results of the Γ-function fit to the muon arrival time distributions. The errors are provided by the fit algorithm. The values t_{min}^{fit} and t_{max}^{fit} are the lower and upper limit of the fit range.

distance [m]	$\langle t \rangle_{e/\gamma}^{\Gamma}$ [ns]	$\sigma_{e/\gamma}^{\Gamma}$ [ns]	$\langle t \rangle_{\mu}^{\Gamma}$ [ns]	σ_{μ}^{Γ} [ns]	$t_{\mathrm{cut}}^{\Gamma}$ [ns]	μ-purity [%]
0-20	6.9 ± 0.8	6.7 ± 0.2	9 ± 1	8.2 ± 0.5	7.7 ± 0.8	35.9 ± 0.2
20-40	10.0 ± 0.9	7.4 ± 0.4	9 ± 2	9.8 ± 0.4	9.5 ± 0.9	14.15 ± 0.06
40-60	13.7 ± 0.7	7.9 ± 0.2	13 ± 1	10.7 ± 0.4	13.5 ± 0.8	8.02 ± 0.04
60-80	17.8 ± 0.7	8.9 ± 0.2	17 ± 2	11.9 ± 0.8	17 ± 1	8.16 ± 0.04
80-100	22.8 ± 0.8	10.6 ± 0.3	20 ± 2	13.1 ± 0.8	21 ± 1	9.96 ± 0.06
100-125	28 ± 1	12.5 ± 0.5	22 ± 4	14 ± 2	25 ± 2	12.60 ± 0.07
125-150	36 ± 4	16 ± 2	26 ± 3	16 ± 1	31 ± 2	16.2 ± 0.1
150-175	43 ± 3	19 ± 1	29 ± 5	17 ± 2	36 ± 3	20.1 ± 0.1
175-200	52 ± 4	24 ± 2	33 ± 6	19 ± 3	42 ± 4	23.5 ± 0.2
200-250	64 ± 7	30 ± 3	39 ± 5	22 ± 2	52 ± 4	27.6 ± 0.2
250-300	82 ± 14	42 ± 6	47 ± 8	26 ± 3	64 ± 8	33.3 ± 0.3
300-400	112 ± 26	60 ± 12	61 ± 10	32 ± 5	86 ± 14	35.8 ± 0.3
>400	154 ± 57	82 ± 27	87 ± 11	51 ± 6	121 ± 29	40.0 ± 0.7

Table D.7: Mean arrival times, separation cut values and muon purities calculated from results of the Γ-fits. The errors of the mean values $\langle t \rangle^{\Gamma}$ and the standard deviations σ^{Γ} are calculated via error propagation of the errors of the fit results. The errors of the muon purities correspond to the statistical errors.

D.4 Separation cut values determined with results from the Log-normal-fit

distance [m]	χ^2 / n.d.f	σ	θ	m	A	$t_{\mathrm{min}}^{\mathrm{fit}}$	$t_{\mathrm{max}}^{\mathrm{fit}}$
0-20	637.13 / 19	0.49 ± 0.01	992.3 ± 0.3	13.8 ± 0.3	55242 ± 285	979	1061
20-40	301.83 / 12	0.50 ± 0.01	994.2 ± 0.3	14.7 ± 0.2	445508 ± 2227	1000	1016
40-60	269.34 / 13	0.32 ± 0.01	989.4 ± 0.6	22.4 ± 0.5	794725 ± 2182	1003	1020
60-80	192.21 / 15	0.34 ± 0.01	992.2 ± 0.6	23.7 ± 0.6	664769 ± 2079	1006	1025
80-100	143.47 / 17	0.39 ± 0.01	995.8 ± 0.7	24.5 ± 0.6	461789 ± 2114	1009	1030
100-125	184.14 / 21	0.53 ± 0.01	1002.4 ± 0.5	23.9 ± 0.4	408117 ± 2560	1012	1037
125-150	83.73 / 27	0.47 ± 0.02	1000 ± 1	32.4 ± 0.8	257430 ± 1913	1015	1046
150-175	83.27 / 34	0.50 ± 0.01	1001.7 ± 0.7	38.0 ± 0.6	163540 ± 1091	1018	1056
175-200	101.41 / 47	0.43 ± 0.02	995 ± 2	51 ± 1	107452 ± 984	1017	1163
200-250	229.07 / 70	0.44 ± 0.01	994 ± 1	64 ± 1	125739 ± 765	1017	1092
250-300	252.23 / 104	0.46 ± 0.01	990 ± 2	83 ± 2	53868 ± 342	1023	1132
300-400	302.09 / 140	0.57 ± 0.02	998 ± 2	102 ± 2	34507 ± 345	1027	1172
>400	856.23 / 358	0.81 ± 0.02	1035.9 ± 0.9	108 ± 2	6220 ± 91	1037	1400

Table D.8: Fit results of the Log-normal-function fit to the electron distributions. The errors are provided by the fit algorithm. The values $t_{\mathrm{min}}^{\mathrm{fit}}$ and $t_{\mathrm{max}}^{\mathrm{fit}}$ are the lower and upper limit of the fit range.

distance [m]	χ^2 / n.d.f	σ	θ	m	A	$t_{\min}^{\text{fit}}$	$t_{\max}^{\text{fit}}$
0-20	167.29 / 24	0.109 ± 0.003	924 ± 2	80 ± 2	59205 ± 310	977	1053
20-40	159.93 / 16	0.31 ± 0.03	978 ± 3	30 ± 2	147891 ± 1210	997	1027
40-60	68.42 / 19	0.26 ± 0.01	974 ± 2	37 ± 2	139075 ± 746	999	1022
60-80	65.78 / 20	0.34 ± 0.03	982 ± 2	31 ± 2	110990 ± 936	1001	1025
80-100	107.36 / 20	0.46 ± 0.03	990 ± 2	26 ± 1	87720 ± 1131	1003	1027
100-125	73.18 / 24	0.50 ± 0.02	992.3 ± 0.7	27.7 ± 0.6	89973 ± 813	1004	1032
125-150	279.06 / 53	0.368 ± 0.006	980.4 ± 0.5	42.0 ± 0.5	68195 ± 298	997	1113
150-175	182.85 / 61	0.54 ± 0.01	992.1 ± 0.6	34.8 ± 0.5	51730 ± 282	1003	1149
175-200	303.06 / 79	0.56 ± 0.01	992.1 ± 0.5	39.5 ± 0.5	41967 ± 240	1001	1123
200-250	228.60 / 77	0.539 ± 0.009	992.6 ± 0.6	44.3 ± 0.5	56401 ± 294	1003	1085
250-300	147.66 / 85	0.67 ± 0.02	1000 ± 1	44.7 ± 0.8	30440 ± 248	1015	1110
300-400	144.52 / 104	0.81 ± 0.03	1010 ± 1	52.2 ± 0.8	22341 ± 279	984	1241
>400	327.92 / 260	0.96 ± 0.03	1016 ± 1	75 ± 2	5374 ± 90	1022	1287

Table D.9: Fit results of the Log-normal-function fit to the muon distributions. The errors are provided by the fit algorithm. The values $t_{\min}^{\text{fit}}$ and $t_{\max}^{\text{fit}}$ are the lower and upper limit of the fit range.

distance [m]	$\langle t\rangle^{\log}_{e/\gamma}$ [ns]	$\sigma^{\log}_{e/\gamma}$ [ns]	$\langle t\rangle^{\log}_{\mu}$ [ns]	$\sigma^{\log}_{\mu}$ [ns]	$t^{\log}_{\text{cut}}$ [ns]	μ-purity [%]
0-20	7.8 ± 0.2	8.0 ± 0.3	4.4 ± 0.2	8.8 ± 0.3	6.1 ± 0.1	36.8 ± 0.2
20-40	10.8 ± 0.2	8.9 ± 0.3	9 ± 1	10 ± 1	10.0 ± 0.5	14.15 ± 0.06
40-60	13.0 ± 0.2	7.7 ± 0.3	11.9 ± 0.5	10.0 ± 0.8	12.4 ± 0.3	8.25 ± 0.04
60-80	17.3 ± 0.3	8.9 ± 0.4	16 ± 1	12 ± 1	16.4 ± 0.5	8.40 ± 0.04
80-100	22.3 ± 0.4	10.8 ± 0.5	19 ± 1	14 ± 1	20.9 ± 0.6	10.28 ± 0.06
100-125	29.9 ± 0.5	15.6 ± 0.7	23.8 ± 0.5	17.0 ± 0.8	26.9 ± 0.4	12.28 ± 0.07
125-150	36.2 ± 0.8	18 ± 1	25.4 ± 0.2	17.1 ± 0.4	30.8 ± 0.4	16.2 ± 0.1
150-175	44.8 ± 0.5	23.1 ± 0.8	32.4 ± 0.4	23.7 ± 0.8	38.6 ± 0.3	18.7 ± 0.1
175-200	51 ± 1	25 ± 2	38.5 ± 0.4	28.3 ± 0.9	44.8 ± 0.6	22.5 ± 0.2
200-250	64 ± 1	33 ± 1	43.8 ± 0.4	29.8 ± 0.8	53.9 ± 0.5	26.7 ± 0.2
250-300	82 ± 1	45 ± 2	56 ± 1	42 ± 2	69.4 ± 0.8	31.6 ± 0.2
300-400	118 ± 2	74 ± 4	82 ± 2	70 ± 5	100 ± 1	32.8 ± 0.3
>400	187 ± 3	147 ± 9	134 ± 3	144 ± 12	161 ± 2	34.5 ± 0.6

Table D.10: Mean arrival times, separation cut values and muon purities calculated from results of the Log-normal-function fits. The errors of the mean values $\langle t\rangle^{\log}$ and the standard deviations $\sigma^{\log}$ are calculated via error propagation of the errors of the fit results. The errors of the muon purities correspond to the statistical errors.

D.5 Influence of the precision of the shower core position
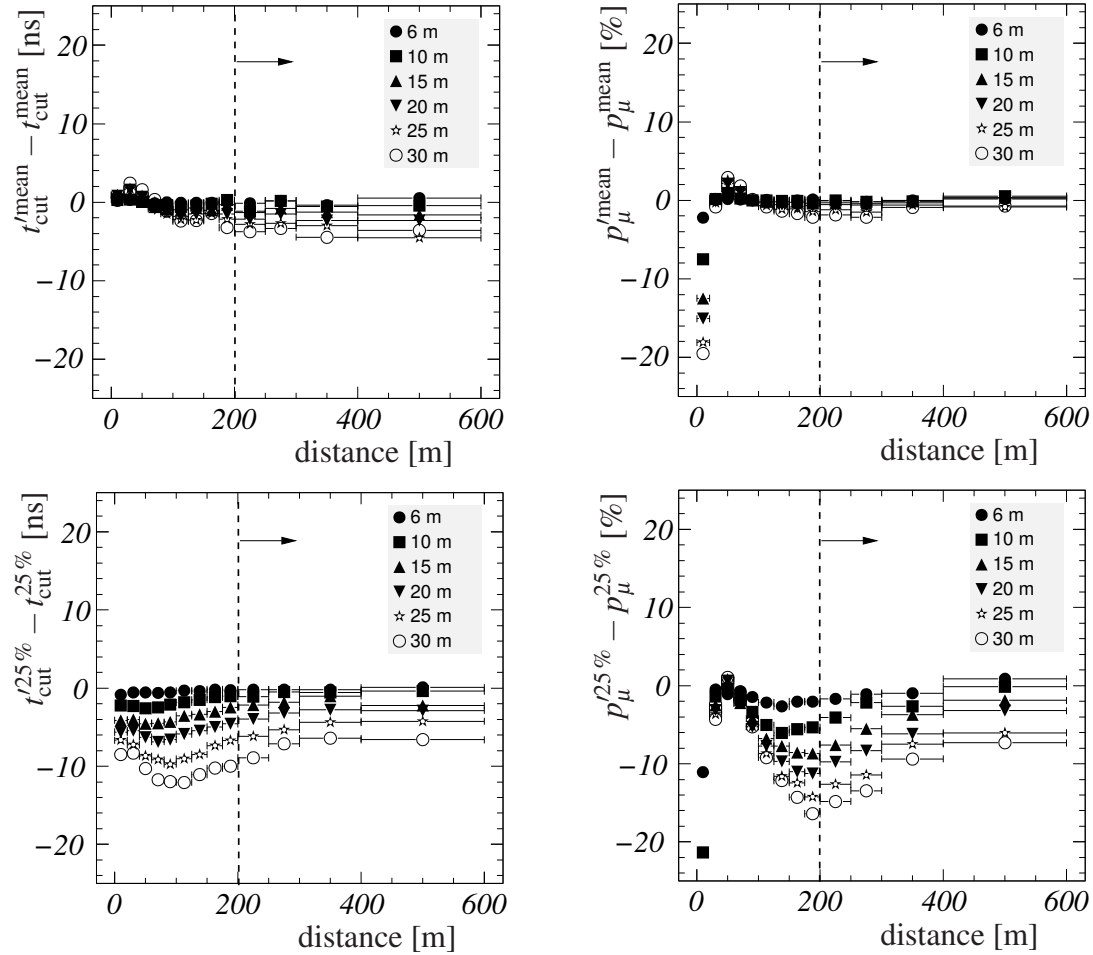
Figure D.1: Relative deviation of the separation cut values and the muon purities calculated from the mean value and the 25 %-quantile for various values of the core position smearing. The dashed lines represent the core distance above which a separation of electrons and muons according to their arrival times becomes feasible.
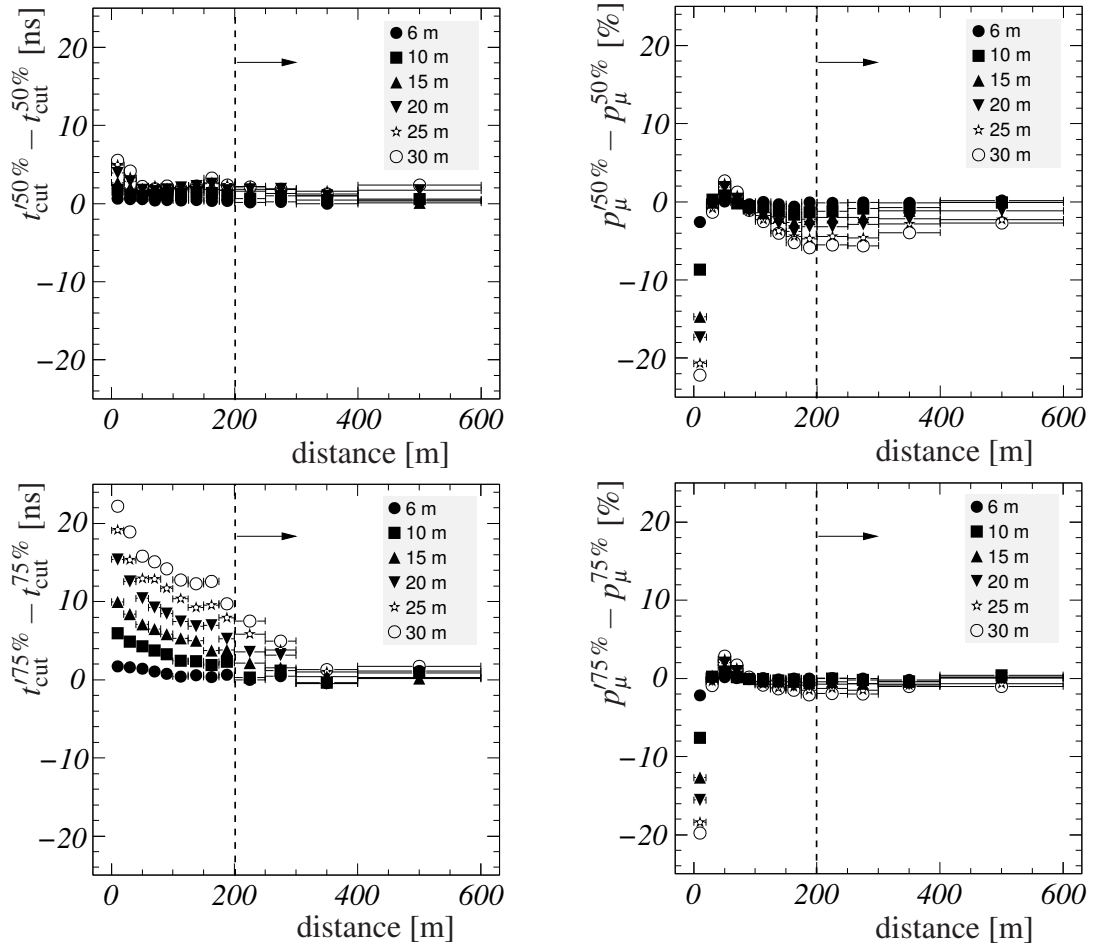
Figure D.2: Relative deviation of the separation cut values and the muon purities calculated from the 50 %-quantile and the 75 %-quantile for various values of the core position smearing. The dashed lines represent the core distance above which a separation of electrons and muons according to their arrival times becomes feasible.

D.6 Influence of the size of the average MIP detector response
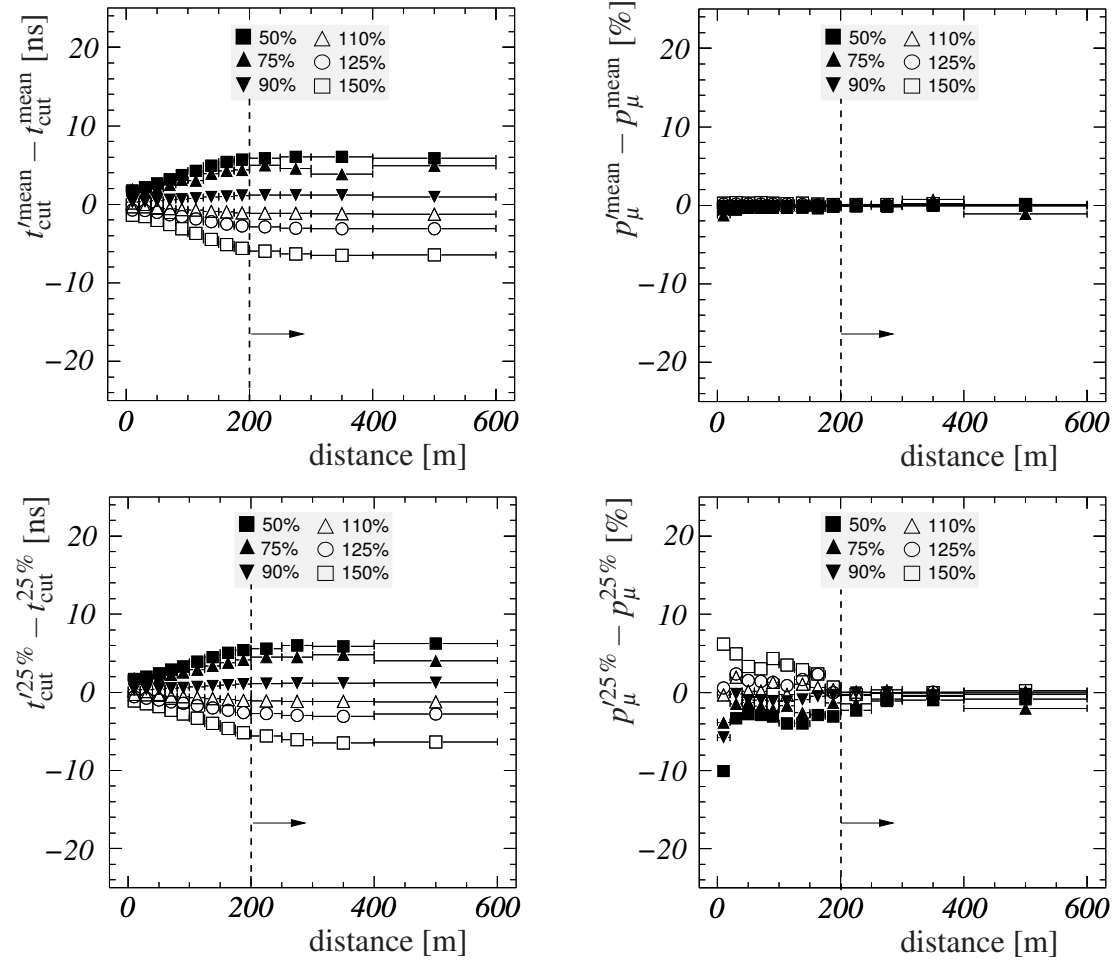
Figure D.3: Relative deviation of the separation cut values and the muon purities calculated from the mean value and the 25 %-quantile for various sizes of the average MIP detector response. The dashed lines represent the core distance above which a separation of electrons and muons according to their arrival times becomes feasible.
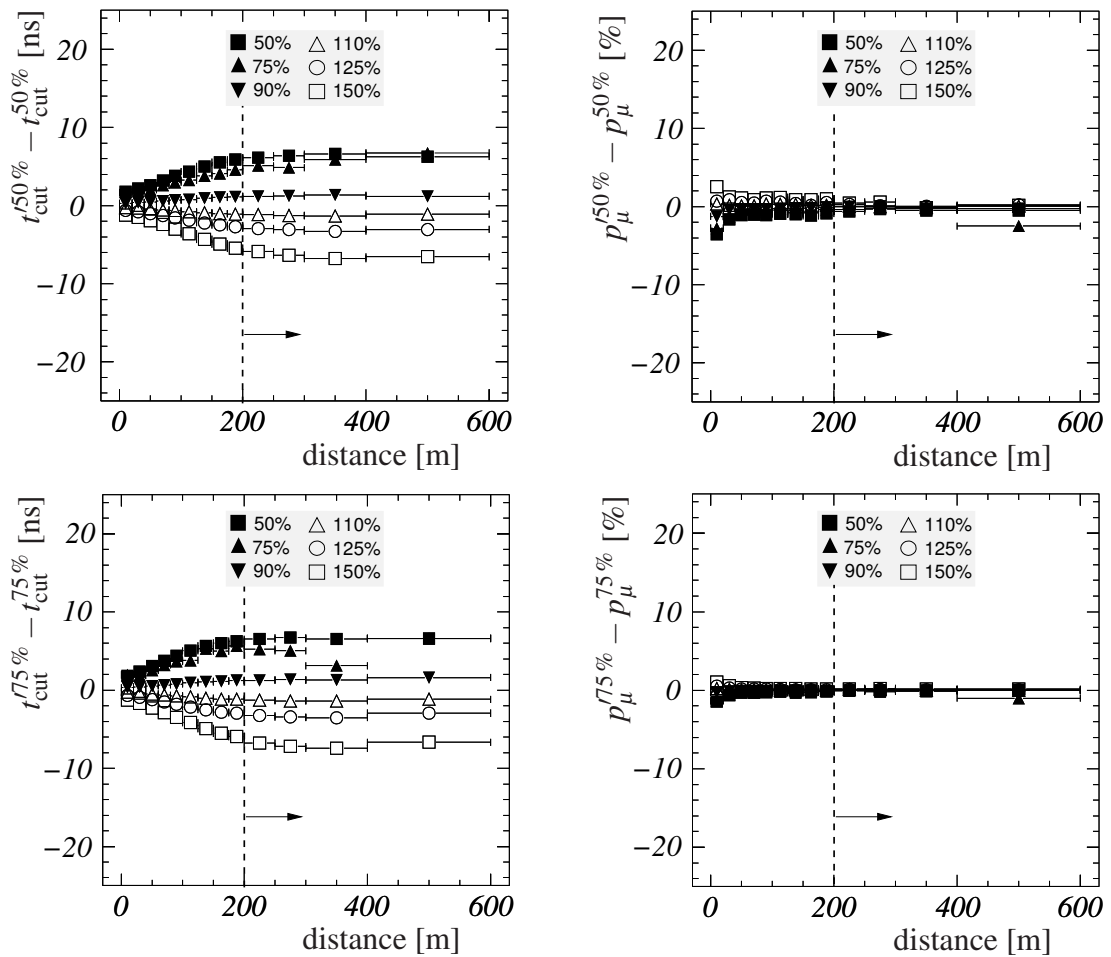
Figure D.4: Relative deviation of the separation cut values and the muon purities calculated from the 50 %-quantile and the 75 %-quantile for various sizes of the average MIP detector response. The dashed lines represent the core distance above which a separation of electrons and muons according to their arrival times becomes feasible.

D.7 Separation cut values and muon purities with systematics

distance [m]	$t_{\text{cut}}^{\text{mean}}$ [ns]	p_{μ}^{mean} [%]	$t_{\text{cut}}^{25\%}$ [ns]	$p_{\mu}^{25\%}$ [%]
0-20	$6.75 \pm 0.2 \pm 20.78$	$39.0 \pm 0.2 \pm 0.5$	$3.53 \pm 0.2 \pm 21.96$	$68.6 \pm 0.4 \pm 19.2$
20-40	$10.10 \pm 0.03 \pm 20.60$	$13.40 \pm 0.06 \pm 0.79$	$5.89 \pm 0.03 \pm 21.29$	$19.4 \pm 0.1 \pm 10.8$
40-60	$15.81 \pm 0.01 \pm 19.23$	$6.86 \pm 0.03 \pm 0.69$	$9.32 \pm 0.01 \pm 19.96$	$11.23 \pm 0.07 \pm 9.16$
60-80	$21.77 \pm 0.01 \pm 17.29$	$7.03 \pm 0.04 \pm 0.52$	$12.43 \pm 0.01 \pm 18.35$	$12.98 \pm 0.08 \pm 7.55$
80-100	$27.80 \pm 0.02 \pm 15.92$	$8.60 \pm 0.05 \pm 0.34$	$15.09 \pm 0.02 \pm 17.03$	$17.9 \pm 0.1 \pm 4.9$
100-125	$34.34 \pm 0.03 \pm 14.86$	$10.35 \pm 0.05 \pm 0.21$	$18.00 \pm 0.03 \pm 15.82$	$23.9 \pm 0.1 \pm 2.1$
125-150	$41.13 \pm 0.05 \pm 13.60$	$12.67 \pm 0.07 \pm 0.05$	$21.70 \pm 0.05 \pm 14.40$	$29.6 \pm 0.2 \pm 0.9$
150-175	$47.74 \pm 0.07 \pm 12.76$	$15.4 \pm 0.1 \pm 0.2$	$24.96 \pm 0.07 \pm 13.42$	$34.4 \pm 0.2 \pm 2.5$
175-200	$55.65 \pm 0.09 \pm 12.29$	$18.3 \pm 0.1 \pm 0.3$	$29.25 \pm 0.09 \pm 12.88$	$39.5 \pm 0.3 \pm 3.9$
200-250	$67.5 \pm 0.1 \pm 12.0$	$21.9 \pm 0.1 \pm 0.4$	$35.5 \pm 0.1 \pm 12.7$	$44.4 \pm 0.3 \pm 4.5$
250-300	$81.4 \pm 0.2 \pm 12.0$	$27.4 \pm 0.2 \pm 0.5$	$42.9 \pm 0.2 \pm 12.6$	$48.4 \pm 0.4 \pm 4.8$
300-400	$105.2 \pm 0.2 \pm 12.4$	$30.9 \pm 0.3 \pm 0.3$	$55.2 \pm 0.2 \pm 13.2$	$50.5 \pm 0.5 \pm 3.2$
> 400	$135.3 \pm 0.6 \pm 12.0$	$36.3 \pm 0.8 \pm 0.5$	$74.0 \pm 0.6 \pm 13.3$	$53 \pm 1 \pm 2$

Table D.11: Separation cut values and muon purities calculated from the mean value and the 25 %-quantile with statistical and systematic errors. The overall error is dominated by systematics.

distance [m]	$t_{\text{cut}}^{50\%}$ [ns]	$p_{\mu}^{50\%}$ [%]	$t_{\text{cut}}^{75\%}$ [ns]	$p_{\mu}^{75\%}$ [%]
0-20	$5.72 \pm 0.2 \pm 21.90$	$42.1 \pm 0.2 \pm 6.3$	$9.66 \pm 0.2 \pm 21.66$	$39.1 \pm 0.2 \pm 2.5$
20-40	$8.57 \pm 0.03 \pm 21.32$	$13.97 \pm 0.06 \pm 3.84$	$13.83 \pm 0.03 \pm 20.92$	$13.27 \pm 0.05 \pm 1.27$
40-60	$12.82 \pm 0.01 \pm 20.08$	$7.52 \pm 0.04 \pm 3.02$	$19.98 \pm 0.01 \pm 19.42$	$6.87 \pm 0.03 \pm 0.78$
60-80	$16.76 \pm 0.01 \pm 18.49$	$8.25 \pm 0.04 \pm 2.39$	$26.75 \pm 0.01 \pm 17.77$	$7.10 \pm 0.03 \pm 0.52$
80-100	$20.63 \pm 0.02 \pm 16.96$	$10.49 \pm 0.06 \pm 1.88$	$33.53 \pm 0.02 \pm 16.27$	$8.57 \pm 0.04 \pm 0.29$
100-125	$25.30 \pm 0.03 \pm 15.59$	$12.83 \pm 0.07 \pm 1.19$	$41.66 \pm 0.03 \pm 15.06$	$10.27 \pm 0.05 \pm 0.13$
125-150	$30.47 \pm 0.05 \pm 14.23$	$16.66 \pm 0.09 \pm 0.61$	$50.27 \pm 0.05 \pm 13.75$	$12.34 \pm 0.07 \pm 0.05$
150-175	$35.74 \pm 0.07 \pm 13.30$	$20.7 \pm 0.1 \pm 0.4$	$58.63 \pm 0.07 \pm 13.03$	$14.68 \pm 0.09 \pm 0.08$
175-200	$42.45 \pm 0.09 \pm 12.78$	$23.9 \pm 0.2 \pm 0.6$	$68.61 \pm 0.09 \pm 12.60$	$17.4 \pm 0.1 \pm 0.3$
200-250	$51.9 \pm 0.1 \pm 12.6$	$27.8 \pm 0.2 \pm 0.7$	$84.8 \pm 0.1 \pm 12.4$	$20.4 \pm 0.1 \pm 0.3$
250-300	$63.7 \pm 0.2 \pm 12.7$	$33.6 \pm 0.3 \pm 1.1$	$104.4 \pm 0.2 \pm 12.4$	$25.3 \pm 0.2 \pm 0.3$
300-400	$84.5 \pm 0.2 \pm 13.1$	$37.0 \pm 0.3 \pm 1.2$	$139.9 \pm 0.2 \pm 12.9$	$28.6 \pm 0.2 \pm 0.3$
> 400	$114.0 \pm 0.6 \pm 13.1$	$41.6 \pm 0.8 \pm 0.9$	$187.8 \pm 0.6 \pm 12.2$	$32.3 \pm 0.6 \pm 0.2$

Table D.12: Separation cut values and muon purity calculated from the the 50 %-quantile and the 75 %-quantile of the arrival time distributions with statistical and systematic errors. The overall error is dominated by systematics.

List of Figures

List of Tables

Bibliography

[Abb04]   R. U. Abbasi et al., *Measurement of the flux of ultrahigh energy cosmic rays from monocular observations by the High Resolution Fly's Eye experiment*, Phys. Rev. Lett. **92** (2004), 151101, astro-ph/0208243.

[Abr04]   J. Abraham et al., *Properties and performance of the prototype instrument for the Pierre Auger Observatory*, Nucl. Instrum. Meth. **A523** (2004), 50–95.

[Agl89]   M. Aglietta et al., *The EAS TOP array at $E(0) = 10^{14}$ eV - 10^{16} eV: Stability and resolutions*, Nucl. Instrum. Meth. **A277** (1989), 23–28.

[Agl93]   M. Aglietta et al., *UHE cosmic ray event reconstruction by the electromagnetic detector of EAS-TOP*, Nucl. Instrum. Meth. **A336** (1993), 310–321.

[Agn95]   G. Agnetta et al., *GREX/COVER_PLASTEX: An experiment to analyze the space-time structure of extensive air showers produced by primary cosmic rays of 10^{15} eV*, Nucl. Instrum. Meth. **A359** (1995), 596–602.

[Agn97]   G. Agnetta et al., *Time structure of the extensive air shower front*, Astroparticle Physics **6** (1997), 301–312.

[Aha04]   F. A. Aharonian et al., *High-energy particle acceleration in the shell of a supernova remnant*, Nature. **432** (2004), 75–77.

[Ant01]   T. Antoni et al., *Electron, muon, and hadron lateral distributions measured in air-showers by the KASCADE experiment*, Astropart. Phys. **14** (2001), 245–260, astro-ph/0004233.

[Ant03a] T. Antoni, *Nachweis hochenergetischer Myonen in ausgedehnten Luftschauern bei KASCADE*, Ph.D. thesis, Universität Heidelberg, Germany, 2003.

[Ant03b] T. Antoni et al., *The Cosmic-Ray Experiment KASCADE*, Nucl. Instrum. Meth. **A513** (2003), 429–675.

[Ant05]   T. Antoni et al., *KASCADE measurements of energy spectra for elemental groups of cosmic rays: Results and open problems*, Astropart. Phys. **24** (2005), 1–25, astro-ph/0505413.

[Ape06] W. D. Apel et al., *Comparison of measured and simulated lateral distributions for electrons and muons with KASCADE*, Astropart. Phys. **24** (2006), 467–483.

[Aug39] P. Auger, P. Ehrenfest, R. Maze, J. Daudin, and R. A. Fréon, *Extensive Cosmic-Ray Showers*, Rev. Mod. Phys. **11** (1939), 288–291.

[AZ01] T. Abu-Zayyad et al., *Measurement of the cosmic ray energy spectrum and composition from 10^{17} eV to $10^{18.3}$ eV using a hybrid fluorescence technique*, Astrophys. J. **557** (2001), 686–699, astro-ph/0010652.

[Bah03] J. N. Bahcall and E. Waxman, *Has the GZK cutoff been discovered?*, Phys. Lett. **B556** (2003), 1–6, hep-ph/0206217.

[Ber99] E. G. Berezhko and L. T. Ksenofontov, *Composition of cosmic rays accelerated in supernova remnants*, J. Exp. Theor. Phys. **89** (1999), 391–403.

[Bir94] D. J. Bird et al., *The cosmic-ray energy spectrum observed by the Fly's Eye*, Astrophys. J. **424** (1994), 491–502.

[Blo98] V. Blobel and E. Lohrmann, *Statistische und numerische Methoden der Datenanalyse*, B. G. Teubner Stuttgart, 1998.

[Boz01] H. Bozdog et al., *The detector system for measurement of multiple cosmic muons in the central detector of KASCADE*, Nucl. Instrum. Meth. **A465** (2001), 455–471.

[Bre98] M. Brendle and U. Raidt, *The triggering and timing electronics of the KASCADE central detector*, Nucl. Instrum. Meth. **A412** (1998), 420–424.

[Bur06] J. v. Buren, *Investigations of the muon component of extensive air showers measured by KASCADE-Grande*, Ph.D. thesis, Universität Karlsruhe, Germany, 2006.

[Can02] J. Candia, L. N. Epele, and E. Roulet, *Cosmic ray photodisintegration and the knee of the spectrum*, Astropart. Phys. **17** (2002), 23–33, astro-ph/0011010.

[Ces83] C. J. Cesarsky and T. Montmerle, *Gamma rays from active regions in the galaxy - The possible contribution of stellar winds*, Space Sci. Revs. **36** (1983), 173–193.

[Che86] K. S. Cheng, C. Ho, and M. A. Ruderman, *Energetic radiation from rapidly spinning pulsars. 1. Outer magnetosphere gaps. 2. Vela and crab*, Astrophys. J. **300** (1986), 500–539.

[Cow98] G. Cowan, *Statistical Data Analysis*, Oxford University Press, 1998.

[Dar06] A. Dar and A. De Rujula, *A theory of cosmic rays*, hep-ph/0606199.

[Dol02] P. Doll et al., *Muon tracking detector for the air shower experiment KASCADE*, Nucl. Instrum. Meth. **A488** (2002), 517–535.

[Dru83]   L. O. Drury, *An introduction to the theory of diffusive shock acceleration of energetic particles in tenuous plasma*, Rept. Prog. Phys. **46** (1983), 973–1027.

[Efi91]   N. N. Efimov et al., *The energy spectrum and anisotropy of primary cosmic rays at energy $E(0) > 10^{17}$ eV observed in Yakutsk*, Proc. ICCR Int. Symp. *Astrophysical Aspects of the Most Energetic Cosmic Rays* (1991), 20.

[Eng99]   J. Engler et al., *A warm-liquid calorimeter for cosmic-ray hadrons*, Nucl. Instrum. Meth. **A427** (1999), 528–542.

[Eno02]   R. Enomoto et al., *The acceleration of cosmic ray protons in the supernova remnant RX J1713.7-3946*, Nature **416** (2002), 823–826.

[Eva00]   M. Evans, N. Hastings, and B. Peacock, *Statistical Distributions*, New York: Wiley, 2000.

[Fas03]   A. Fasso et al., *The physics models of FLUKA: Status and recent development*, ECONF **C0303241** (2003), MOMT005, hep-ph/0306267.

[Fer49]   E. Fermi, *On the Origin of the Cosmic Radiation*, Phys. Rev. **75** (1949), 1169–1174.

[Fer05]   A. Ferrari, P. R. Sala, A. Fasso, and J. Ranft, *FLUKA: A multi-particle transport code (Program version 2005)*, Report **CERN-2005-010** (2005).

[Gla05a] R. Glasstetter, *private communication*, 2005.

[Gla05b] R. Glasstetter et al., *Shower size reconstruction at KASCADE-Grande*, Proc. 29th Int. Cosmic Ray Conf., Pune **00** (2005), 101–106.

[Gol64]   R. Gold, *An iterative unfolding method for response matrices*, Argonne National Laboratory Report ANL-6984 (1964), 2–37.

[Gre56]   K. Greisen, *The Extensive Air Showers*, Prog. Cosmic Ray Phys. **III** (1956), 1–141.

[Gre66]   K. Greisen, *End to Cosmic-Ray Spectrum?*, Phys. Rev. Lett. **16** (1966), S748–750.

[Hae96]   R. Haeusler, *Aufbau und erste Messungen des Top-Clusters von KASCADE*, Diploma thesis, Universität Karlsruhe, Germany, 1996.

[Har90]   A. K. Harding and T. K. Gaisser, *Acceleration by pulsar winds in binary systems*, Astrophys. J. **358** (1990), 561–574.

[Hau03]   A. Haungs et al., *The KASCADE-Grande Experiment*, Proc. 28th Int. Cosmic Ray Conf., Tsukuba **2** (2003), 985–988.

[Hay00]   N. Hayashida et al., *Updated AGASA event list above 4×10^{19} eV*, Astronomical Journal **120** (2000), 2190.

[Hec98]   D. Heck, G. Schatz, T. Thouw, J. Knapp, and J. N. Capdevielle, *CORSIKA: A Monte Carlo code to simulate extensive air showers*, Report **FZKA-6019** (1998).

[Hes12]   V. F. Hess, *Über Beobachtungen der durchdringenden Strahlung bei sieben Freiballonfahrten*, Phys. Zeitsch. **13** (1912), 1084–1091.

[Hil05]   A. M. Hillas, *Can diffusive shock acceleration in supernova remnants account for high-energy galactic cosmic rays?*, J. Phys. **G31** (2005), R95–R131.

[Hor01]   A. Horneffer, *Aufbau eines Flash-ADC Systems und Messung der Zeitstruktur ausgedehnter Luftschauer mit dem KASCADE-Experiment*, Diploma thesis, Universität Karlsruhe, Germany, 2001.

[Jok87]   J. R. Jokipii and G. Morfill, *Ultra-high-energy cosmic rays in a galactic wind and its termination shock*, Astrophys. J. **312** (1987), 170–177.

[Kal93]   N. N. Kalmykov and S. S. Ostapchenko, *The nucleus-nucleus interaction, nuclear fragmentation, and fluctuations of extensive air showers*, Phys. Atom. Nucl. **56** (1993), 346–353.

[Kam58]   K. Kamata and J. Nishimura, *The Lateral and the Angular Structure Functions of Electron Showers*, Suppl. Prog. Theo. Phys. **6** (1958), S93–155.

[Kaz01]   D. Kazanas and A. Nicolaidis, *Cosmic Ray "Knee": A Herald of New Physics?*, Proc. 27th Int. Cosmic Ray Conf., Hamburg (2001), 1760.

[Kaz03]   D. Kazanas and A. Nicolaidis, *Cosmic Rays and Large Extra Dimensions*, Gen. Rel. Grav. **35** (2003), 1117.

[Knu06]   S. P. Knurenko et al., *Characteristics of EAS and primary particle mass composition in the energy region of 10^{17} eV - 3×10^{19} eV by Yakutsk data*, Nucl. Phys. Proc. Suppl. **151** (2006), 92–95, astro-ph/0411483.

[Kob02]   K. Kobayakawa, Y. Sato, and T. Samura, *Acceleration of particles by oblique shocks and cosmic ray spectra around the knee region*, Phys. Rev. **D66** (2002), 083004, astro-ph/0008209.

[Kri92]   W. Kriegleder, *Ein Detektorsystem zum Nachweis von Myonen in ausgedehnten Luftschauern für das KASCADE-Projekt*, Ph.D. thesis, 1992, KfK 5023.

[Kul59]   G. L. Kulikov and G. B. Khristiansen, *On the size spectrum of extensive air showers*, Sov. Phys. JETP 35 **8** (1959), 441–444.

[Lag01]   A. A. Lagutin and R. I. Raikin, *Lateral distribution of electrons in EAS at superhigh energies: predictions and experimental data*, Nucl. Phys. Proc. Suppl. **97** (2001), 274–277.

[Lin85]   J. Linsley, *Standard value for the radiation length in air*, Proc. 19th Int. Cosmic Ray Conf., La Jolla **7** (1985), 163–166.

[Mai03]   G. Maier, *Suche nach Anisotropie in der kosmischen Strahlung mit dem KASCADE-Experiment*, Ph.D. thesis, Universität Karlsruhe, Germany, 2003.

[May90]   H. J. Mayer, *On the benefits of a thin lead shield for the performance of an extended air shower array*, Nucl. Instr. Meth. **A294** (1990), 651–662.

[Nel85]   W. R. Nelson, H. Hirayama, and D. W. O. Rogers, *The EGS4 Code System*, Report **SLAC-0265** (1985), Stanford Linear Accelerator Center.

[Ogi03]   S. Ogio and F. Kakimoto, *Advective diffusion propagation model for galactic cosmic rays above 10^{12} eV*, Proc. 28th Int. Cosmic Ray Conf., Tsukuba **1** (2003), 315–318.

[Ost06]   S. Ostaptchenko, *private communication*, 2006.

[Ove04]   S. Over, *Development and commissioning of data acquisition systems for the KASCADE-Grande experiment*, Diploma thesis, Universität Siegen, Germany, 2004.

[Ptu93]   V. S. Ptuskin et al., *Diffusion and drift of very high energy cosmic rays in galactic magnetic fields*, Astron. Astrophys. **268** (1993), 726–735.

[Rac93]   J. P. Rachen and P. L. Biermann, *Extragalactic ultrahigh-energy cosmic rays. 1. Contribution from hot spots in FR-II radio galaxies*, Astron. Astrophys. **272** (1993), 161–175, astro-ph/9301010.

[Ric03]   S. Richter, *Untersuchung der Feinstruktur des Kerns hochenergetischer Luftschauer*, Diploma thesis, Universität Karlsruhe, Germany, 2003.

[Ris00]   M. Risse, *Test und Analyse hadronischer Wechselwirkungsmodelle mit KASCADE-Ereignisraten*, Ph.D. thesis, Universität Karlsruhe, Germany, 2000.

[Rou04]   E. Roulet, *Astroparticle theory: Some new insights into high energy cosmic rays*, Int. J. Mod. Phys. **A19** (2004), 1133–1141, astro-ph/0310367.

[Sch96]   H. Schieler, *Konzeption, Entwicklung und Test des lokalen Datenerfassungssystems für das strukturierte Detektor-Array von KASCADE*, Ph.D. thesis, Universität Karlsruhe, Germany, 1996.

[Sch05]   H. Schieler, *private communication*, 2005.

[Sig03]   G. Sigl, *The enigma of the highest energy particles of nature*, Ann. Phys. **303** (2003), 117–141, astro-ph/0210049.

[Sim83]   J. A. Simpson, *Elemental and isotopic composition of the galactic cosmic rays*, Ann. Rev. Nucl. Part. Sci. **33** (1983), 323–382.

[Sta93]   T. Stanev, P. L. Biermann, and T. K. Gaisser, *Cosmic rays. IV. The spectrum and chemical composition above 10^4 GeV*, Astron. Astrophys. **274** (1993), 902, astro-ph/9303006.

[Ste99]   F. W. Stecker and M. H. Salamon, *Photodisintegration of ultrahigh energy cosmic rays: A new determination*, Astrophys. J. **512** (1999), 521–526, astro-ph/9808110.

[Tak98]   M. Takeda et al., *Extension of the Cosmic-Ray Energy Spectrum Beyond the Predicted Greisen-Zatsepin-Kuz'min Cutoff*, Physical Review Letters **81** (1998), 1163.

[Tka01]   W. Tkaczyk, *Is the "knee" and "ankle" in cosmic ray spectrum due to its propagation?*, Proc. 27th Int. Cosmic Ray Conf., Hamburg (2001), 1979–1982.

[Ulr04]   H. Ulrich, *Untersuchungen zum primären Energiespektrum der kosmischen Strahlung im PeV-Bereich mit dem KASCADE-Experiment*, Ph.D. thesis, Universität Karlsruhe, Germany, 2004.

[vC33]   P. van Cittert, *Zum Einfluss der Spaltbreite auf die Intensitätverteilung in Spektralinien II*, Z. Physik **69** (1933), 298–308.

[Völ92]   G. Völker, *Ein Detektorsystem zum Nachweis der e/γ-Komponente großer Luftschauer im UHE-Bereich*, Ph.D. thesis, Forschungszentrum Karlsruhe, Germany, 1992.

[Web99]   J. Weber, *Untersuchung der elektromagnetischen und myonischen Komponente ausgedehnter Luftschauer und Bestimmung der Elementzusammensetzung der kosmischen Strahlung*, Ph.D. thesis, Universität Karlsruhe, Germany, 1999.

[Wef91]   J. Wefel, *Cosmic rays, supernovae and the interstellar medium*, NATO ASIC Series 337 **337C** (1991), 29.

[Wet95]   Y. Wetzel, *Messung und Rekonstruktion der elektromagnetischen Komponente ausgedehnter Luftschauer*, Ph.D. thesis, Universität Karlsruhe, Germany, 1995.

[Wig00]   R. Wigmans, *On big bang relics, the neutrino mass and the spectrum of cosmic rays*, Nucl. Phys. Proc. Suppl. **85** (2000), 305–310, hep-ph/0107263.

[Woi75]   C. P. Woidneck and E. Bohm, *The longitudinal particle distribution in the extensive air shower disk*, J. Phys. **A8** (1975), 997–1004.

[Zat66]   G. T. Zatsepin and V. A. Kuzmin, *Upper limit of the spectrum of cosmic rays*, JETP Lett. **4** (1966), 78–80.

Danksagung

Ich möchte an erster Stelle meinem Doktorvater Prof. Dr. Peter Buchholz sehr herzlich für die lehrreiche Zeit danken, die ich in seiner Arbeitsgruppe verbringen durfte. Ich danke ihm dafür, dass er mir das eine oder andere mal seine Vorlesung anvertraut hat, und besonders dafür, dass er es mir ermöglicht hat, an internationalen Schulen und Konferenzen teilnehmen zu können.

Ich danke Prof. Dr. Claus Grupen sehr herzlich für seine Bereitschaft diese Arbeit als Zweitgutachter zu bewerten und für seine humorvollen Beiträge, die sehr zur angenehmen Atmosphäre in der Arbeitsgruppe beitragen.

Bei der gesamten Siegener Arbeitsgruppe bedanke ich mich für die gute Zusammenarbeit und das gemeinsame Schultern verschiedenster Aufgaben. Ich möchte meinen Kollegen Thomas Bäcker, Sven Over und Dirk Zimmermann für die gute Zeit in Siegen und Karlsruhe danken. Für die Einführung in die afrikanische Kultur und für die gemeinsamen Unternehmungen außerhalb der Physik danke ich Nadir Omar Hashim.

Ich danke den Mitgliedern der KASCADE-Grande-Kollaboration für die gute Zusammenarbeit und das Ermöglichen dieser Arbeit. Für die Hilfe in fachlichen Fragen möchte ich mich bei Ralph Glasstetter, Dr. Andreas Haungs und Dr. Harald Schieler bedanken. Für die ausgiebige Unterstützung im Umgang mit KRETA bedanke ich mich nochmals bei Ralph Glasstetter.

Den ehemaligen Kollegen Dr. Ulrich Husemann, Dr. Matthias Böcker, Dr. Markus Adams und Dr. Carsten Cruse danke ich dafür, dass sie mir den Einstieg in die Arbeitsgruppe so angenehm gemacht haben und bei Fragen immer hilfsbereit waren.

Ich danke den Kollegen Thomas Bäcker, Dirk Zimmermann und insbesondere Dr. Wolfgang Walkowiak dafür, dass sie freiwillig auf den einen oder anderen netten Abend verzichtet haben, um diese Arbeit Korrektur zu lesen.

Mein größter Dank gilt meiner gesamten Familie. Ich danke meiner Frau Sylvia, meinen Eltern, Geschwistern, Großeltern und meiner Schwiegermutter, die mir alle in den letzten Jahren unterstützend zur Seite standen.